Journal of INNOVATIVE SCIENCE and ENGINEERING

Volume 7
Issue 1
Year 2023

E-ISSN: 2602-4217

www.jise.btu.edu.tr

J Inno Sci Eng,2023, 7(1):1-12
https://doi.org/10.38088/jise.1118420

Research Article

Comparing Traffic Performances Between Signalized and Give-Way Roundabouts: A Case Study in Bursa

Alphan Kayacan [1], Bahadir Yilmaz [2*], Ahmet M. Ozdemir [2]

[1] *Dokuz Eylül University, Civil Engineering Department, 35160, İzmir, Turkiye*
[2*] *Bursa Technical University, Civil Engineering Department, 16310, Bursa, Turkiye*
+

Abstract

Globally developing economies and opportunities have caused an increase in the density of people in city centers in recent years; thus, an exponential increase has been experienced in the number of motor vehicles, which complicates the creation of a sustainable traffic network. Waiting times and the number of stops cause psychological, physical, and environmental problems. The efficiency of intersections is vital to ensure sustainable transportation. Modern roundabouts outperform signalized roundabouts, and their popularity has been increasing in recent years. However, the geometric features of intersections should be suitable for the location and traffic composition. In this study, the Durmazlar roundabout, which is currently a signalized roundabout in Bursa, has been transformed into a modern roundabout and redesigned. One of the aims of the study is to make minimal changes in the geometry of the roundabout. One-way road applications have been made to regulate entrances and exits on problematic roads. Modeling of the roundabout and collecting data was performed through the PTV Vissim software. Queue length, travel time, and speed parameters of the data obtained regarding the new scenario and the current situation were compared.

Keywords: Modern roundabout, PTV vissim, Signalized roundabout, Traffic simulation.

Cite this paper as:
Kayacan A., Yilmaz, B. and Ozdemir, A. M. (2023). *Comparing traffic performances between signalized and give-way roundabouts: A case study in Bursa*, 7(1):1-12.

*Corresponding author: Bahadir Yilmaz

E-mail: bahadir.yilmaz@btu.edu.tr

Received Date: 18/05/2022
Accepted Date: 08/10/2022

1. Introduction

The constant growth of the world's population, as well as the number of motor vehicles providing transportation around the globe, creates several issues such as traffic accidents, congestion, emission, and noise pollution [1–4]. Due to the global Covid-19 pandemic, people's desire to provide more isolated transportation has caused travel modes to shift from public transportation to private motor vehicles. As a result of this situation, the number of motor vehicles has increased faster than expected, which emphasized the importance of traffic network enhancements [5–7].

The increased number of motor vehicles on urban roads has significantly increased traffic congestion [8–11]. As a result, waiting time in traffic, amount of fuel spent, and amount of emissions have increased. Also, the study showed that intersections account for 47 percent of death or injury incidents in urban areas [1]. To minimize these disadvantages, it is essential that intersections, which are the most important connectors of urban road networks, operate as efficiently as possible. Different types of intersection applications and different traffic control methods can be preferred to reduce traffic congestion [12]. Signalized roundabouts are one of the intersection types that has become less popular around the world in recent years. In addition, signalized roundabouts are one of the most vital elements of traffic conflicts in different modes of transport and in any transport network [3, 13–15]. Stoppages at traffic lights cause the majority of road delays. The number of traffic lights per kilometer, rather than the volume of traffic per lane or the volume-to-capacity ratio, is thought to have a greater impact on travel speeds [16]. This situation forces us to look for an at-grade intersection that can operate more efficiently than signalized roundabouts. In the light of the study, the use of modern roundabouts has increased in recent years despite the lack of definite criteria for the design and implementation of modern roundabouts which are seen to be more efficient than signalized roundabouts in many performance criteria.

In recent years, the microsimulation modeling method has been very popular in the transportation discipline. While a wide variety of simulation softwares and methods are available, PTV's Verkehr In Städten SIMulationsmodell (VISSIM) is widely preferred for its ease of use, speed of resolution, flexibility to create complex problems, and flexibility in simulating jurisdiction-specific networks [17–19].

In this study, the Durmazlar signalized roundabout (located in Bursa, Turkey) has been transformed into a modern roundabout, and all conditions have been investigated by redesigning it. The PTV Vissim software was used in the modeling of the roundabout. Afterwards, evaluations were made between the new scenario and the current situation.

2. Material – Method

The problematic intersections with high traffic density in Bursa province were investigated within the scope of the study. Bursa Metropolitan Municipality Transportation Coordination Branch Office was contacted and information was obtained related to the determined intersections in terms of traffic, accident, plan, expropriation, and the Durmazlar Roundabout that is located on the Boulevard Ata at Nilufer district was chosen for investigation. The features of the Durmazlar Roundabout, such as its being on the main artery, connecting the industrial zone of the province with the residential areas, having one entrance and one exit with non-ideal geometry, and being suitable for geometry changes in expropriation, have influenced the state of its being selected for the study. In Figure 1, the roads connected to the intersection are shown and numbered.

Figure 1. Roads connected to the Durmazlar Roundabout.

The road connected to the roundabout from the northeast direction is connected to the Sanayi Street that is the continuation of the Boulevard Mudanya and is numbered “1”. The road connected from the south is connected to the İzmir Street, which combines the roads in the directios to İzmir, Çalı, and Bursa, and is numbered “2”. The road connected from the northwest direction is connected to Bursa Organized Industrial Zone and Nilufer Organized Industrial Zone and is numbered “3”. The side road connecting the roads 2 and 3 is shown with the number “5”. The last road connected to the roundabout from the east is connected to the Ata Street and is numbered “4”. The PTV Vissim software was used to model the current geometric condition and to reflect criteria such as driver behaviors, traffic characteristics, vehicle tracking models, and signaling systems in the most effective way. The Vissim is a discrete-time micro-scale traffic simulation software that simulates and evaluates all road users in various situations, including intersection designs, urban road traffic, traffic lights, public transport systems, pedestrian movements, and their interactions.

2.1. Modeling of the Current Situation

The drawn model of the intersection area is given in Figure 2. Roads 1, 2, and 3 have been drawn as three lanes for departure and arrival, with a horizontal curve radius equal to the current situation on the satellite image. Lane widths are set at 3.5 meters, except where otherwise noted.

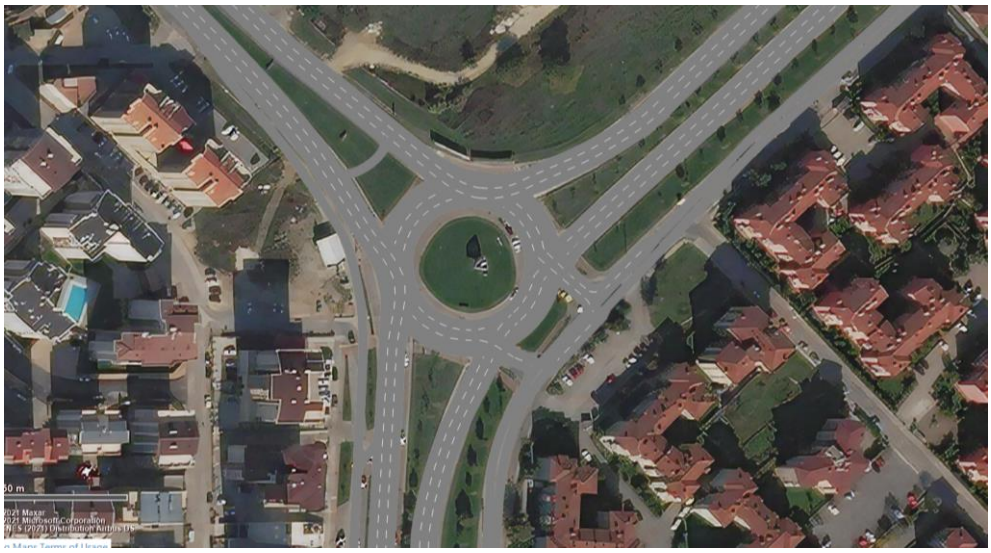

Figure 2. Model of the intersection area drawn in Vissim

In Figure 3, the irregularity is observed in the current state of the road 4. The road numbered 4 is modeled as two lanes, excluding the intersection entrance area. The simulation reflects the current confusion by setting the number of lanes as two arrivals and two departures at the intersection entrances and giving the intersection 3 lanes.

Figure 3. Irregularity on the road 4 in the current situation

Traffic data and signal times of the Durmazlar Roundabout were obtained through Bursa Metropolitan Municipality. Vehicle counts were performed in May 2018 and include peak values for the morning, noon, and evening hours. Vehicles arriving at and exiting the roundabout from all roads and routes are included in the data. The morning count with the highest number of vehicles was used in the simulation. In Table 1, the vehicle count data of the intersection are given.

Table 1: Morning peak hour of motor vehicle counts

	1	2	3	4	5	Total
Morning	1804	2929	1558	733	458	**7482**
1	11	1868	130	71	0	**2080**
2	1243	175	940	64	0	**2422**
3	550	204	0	598	458	**1810**
4	0	682	488	0	0	**1170**
5	0	0	0	0	0	**0**

The Durmazlar Roundabout signaling cycle time is 74 seconds. The signaling cycle diagram prepared in the Vissim is given in Figure 4.

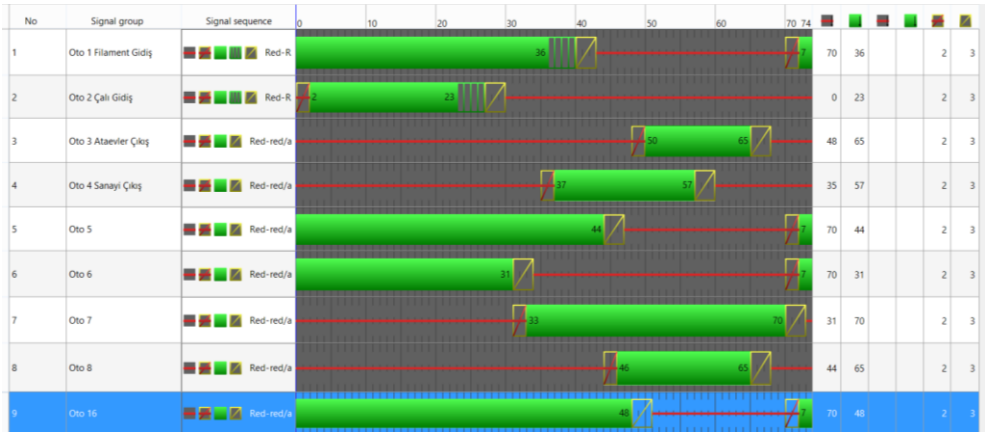

Figure 4. Current situation signaling cycle diagram

2.2. Modeling of the 4-Way Modern Roundabout

In this scenario, the Durmazlar Roundabout was designed as a modern roundabout by increasing the entrance slopes to the crossroads on each route and imposing speed limits at the intersection entrances. As for the information received from the municipality, a side road has been opened within the expropriation limit for the turns from the road numbered1 to road numbered 3. In addition, a U-turn road was built before the intersection for vehicles that come from the road numbered 1 and turn along the intersection and make a U-turn. Due to the geometrical aspects of the road 4, channeling for right turns from the road 2 to the road 4 was not possible. The road was built in order to make a U-turn before the intersection for vehicles that come from the road 2 and turn along the intersection and make a U-turn. For the turns from the road 3 to the road 1, no separate channeling was established and the existing side road 5 was used. A one-way application was made, with the entrances to the intersection from the road 4, which does not conform to the geometrically modern roundabout standards. A separator island was used to avoid confusion at the roundabout entrances and exits on the road 4. Reduced speed areas have been created by placing speed warning signs at the entrances to the intersection area. As a result of the arrangements made, the view of the intersection area is given in Figure 5.

Figure 5. 4-way modern roundabout modeling

Vehicles connected to the roundabout from the southern route of the road 4 were diverted to the road 2 before the intersection area with the existing crossing. Since the signaling system at the roundabout has been removed, the priority rule of the vehicle moving in the roundabout has been defined.

3. Results

This title refers to the result reached as a result of the modeling. The created scenario was compared with the current situation.

3.1. Current Situation

As in the on-site observations, a blockage occurred on the road 4 in the simulation as well. Although the roads 1, 2, and 3 were evacuated during the green light periods, they were subject to serious delays due to the congestion in the signaling located in the roundabout. Figure 6 shows the traffic congestions that occurred in the simulation.

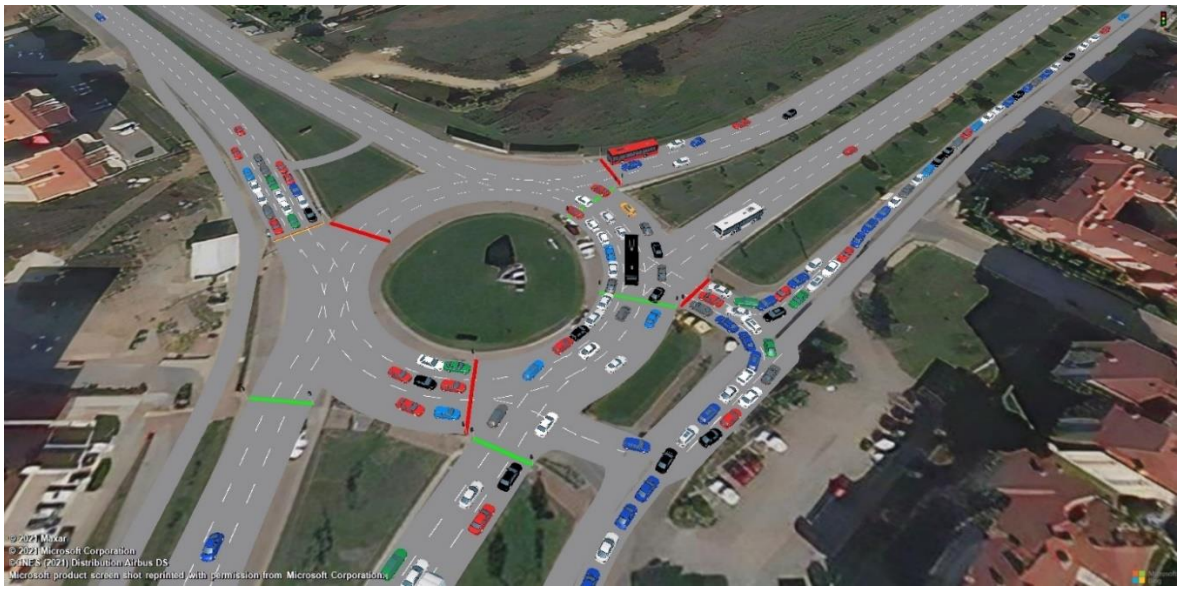

Figure 6. Congestion occurring in the current situation simulation

The average queue length, number of vehicles, and average speed data obtained for the current situation as a result of the simulations are given in Table 2.

Table 2. Current situation simulation "Queue Counter" and "Data Collection Point" data

Road	Avg. Queue Length (m)	Number of Vehicle	Avg. Speed (km/h)
1	23,97	2035	39,84
2	19,43	2419	26,05
3	22,55	1347	24,32
4	80,98	1166	20,9
5	0	441	50,14

The route and travel time of each vehicle entering the intersection are given in Table 3. Each routes travel time was measured from 50 meters before entering the intersection to 50 meters after departing the intersection. In addition to the number of vehicles and travel times, the total number of vehicles and average travel time for each road are given.

Table 3. Current situation simulation "Vehicle Travel Time" data

Route	Number of Vehicle	Travel Time (sec)	Number of Vehicle	Avg. Travel Time (sec)
1→1	10	81,99		
1→2	1830	30,15		
1→3	116	29,47	2033	56,71
1→4 down	35	65,27		
1→4 up	42	76,65		
2→1	1259	30,01		
2→2	166	85,72		
2→3	914	50,09	2404	47,29
2→4 down	29	21,15		
2→4 up	36	49,46		
3→1	565	72,63		
3→2	198	45,83	1331	57,07
3→4 down	266	47,15		
3→4 up	302	62,67		
4 down→3	268	56,58		
4 down→2	344	76,28	1166	74,93
4 up→3	240	75,44		
4 up→2	314	91,43		

The congestion in the road 4 that is shown by the simulation was supported by the values in the obtained data. As seen in the tables, the road 4 is the road with the highest average queue length and average travel time and the

lowest average speed.

3.2. Modern Roundabout

Although traffic performances increased on the roads 2, 3, and 4 in the simulations, much more congestion occurred on the road 1 and long queues were formed. Average queue length, number of vehicles and average speed data of the four-way modern roundabout simulation are given in Table 4.

Table 4. Four-way modern roundabout simulation "Queue Counter" and "Data Collection Point" data

Road	Avg. Queue Length (m)	Number of Vehicle	Avg. Speed (km/h)
1	258,35	1829	13,57
2	65,58	2342	17,47
3	39,54	1334	12,62
4	11,11	693	10,71
5	0	442	60,42
1→3	0	115	61,28
1U	0	9	32,83
2U	0,87	528	31,43

For the four-way modern roundabout, the route and travel time of each vehicle entering the intersection are given in Table 5. Travel time of each route was measured from 50 meters before entering the intersection to 50 meters after departing the intersection. In addition to the number of vehicles and travel times, the total number of vehicles and average travel time for each road are given.

Table 5. Four-way modern roundabout simulation "Vehicle Travel Time" data

Route	Number of Vehicle	Travel Time (sec)	Number of Vehicle	Avg. Travel Time (sec)
1→1	8	13,68		
1→2	1572	60,98		
1→3	104	8,53	1752	37,61
1→4 down	30	43,79		
1→4 up	38	61,08		
2→1	1258	27,12		
2→2	533	11,82		
2→3	1045	30,01	2901	23,16
2→4 down	29	19,04		
2→4 up	36	27,83		
3→1	570	34,52	1340	32,99
3→2	199	31,7		

3→4 down	268	26,24		
3→4 up	303	39,48		
4 up→3	363	30,5	688	31,65
4 up→2	325	32,79		

Among the examined routes, only the travel time of the route from the road 1 to the road 2 increased, while the remaining fifteen travel times decreased. The travel times comparisons of the current situation and four-way modern roundabout simulations are given in Figure 7.

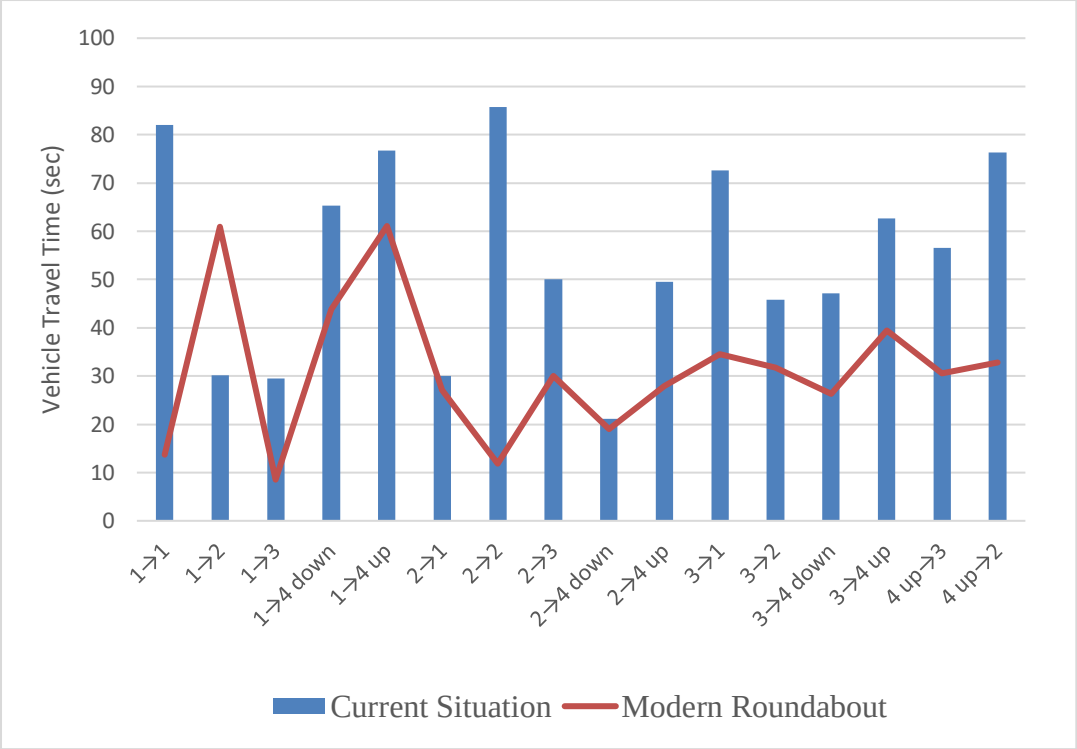

Figure 7. Comparison of the current situation and modern roundabout vehicle travel times

The comparison of the four-way modern roundabout simulation data with the current state data is given in Table 6.

Table 6. Comparison of the current situation and modern roundabout simulation results

	Avg. Queue Length (m)	Number of Vehicle	Avg. Speed (km/h)	Avg. Vehicle Travel Time (sec)
Current Situation	29,39	7408	32,25	58,22
Modern Roundabout	74,92	7292	30,04	31,19
Change (%)	154,94	-1,57	-6,85	-46,42

As can be seen in Table 6, although the performance of the road 4 improved as a result of the changes made, the average queue length, which is one of the performance parameters, increased at a high rate of 154,94% in total.

However, the average vehicle travel time has decreased by 46,42%. Since the amount of vehicles given to the system is the same, it is not expected to change much in the number of vehicles. Thus, the number of vehicles using the intersection area showed a decrease of as low as 1,57%. The average speed of the system also decreased by 6,85%.

3.3. Statistical Analysis

In order to examine the comparability of the mean values of the obtained data, the data were analyzed with the t-test method. Queue length and speed parameters were interpreted by comparing their mean values and variances since they did not have enough data to perform the t-test. For the vehicle travel time parameter, the t-test was applied assuming that the data were normally distributed. Hypotheses are established for the t-test:

H0= Means are equal

Ha= Means are not equal

Data analyzes made in R studio program are given in Figure 8.

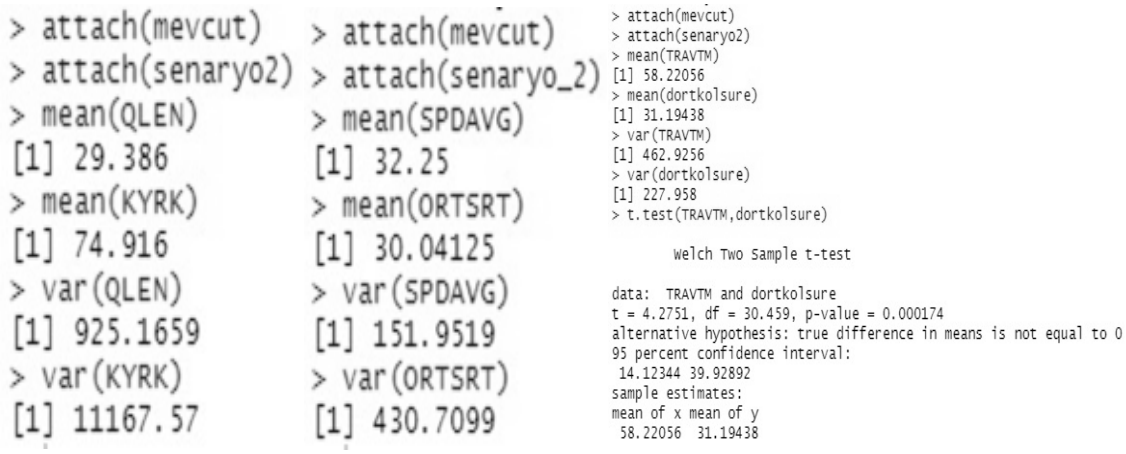

Figure 8. Statistical data analysis steps

As a result of the t-test, the p-value was found to be 0,000174. Since the p-value obtained was less than the minimum value of 0,05, H_0 among the hypotheses established at the beginning of the test was rejected and H_a was accepted. Thus, it has been determined that there is a statistically significant difference between the averages of the travel time data groups of the current situation and modern roundabout scenarios. In the queue length and speed data, which do not have enough data to apply the t-test, the increases or decreases in the averages were supported by the variance values.

4. Conclusion

In the modeling, the signaling systems at the existing roundabout were removed. Arrangements were made in the roundabout area according to the modern roundabout design standards. It has been redesigned by making one-way application on the road 4, which does not comply with geometric standards. With the arrangements made, it was desired to investigate how a modern roundabout, which does not have ideal design features, will perform. As a result of the simulations, the excessive congestion that occurred on road 4 in the current situation was eliminated,

but this time excessive congestion occurred on the road 1. The average queue length across the roundabout increased from 29,39 meters to 74,92 meters. While the variance was 925,17 in the current situation, as a result of changing the roundabout type, it increased approximately 12 times and became 11167,57. These values showed that the average queue length data were measured at extreme values, while excessive congestion occurred on the road 1 in the simulation while supporting the operation of the other roads without congestion. Average speed decreased from 32,25 km/h to 30,04 km/h. While the variance of the speed parameter was 151.95 in the current situation, it was calculated as 430,71 as a result of the modification. In the current situation, the density of vehicles accumulating around the rotating island has shifted to the entrance area of the roundabout after the arrangements made. Although there was an improvement on the problematic road numbered 4, this improvement negatively affected the road numbered 1. Despite all the negativities, thanks to the removal of the signaling in the roundabout, the average travel time of vehicles has decreased from 58,22 seconds to 31,19 seconds since they entered the roundabout area. The decrease in the variance from 462,93 to 227,96 supported the improvement in the travel time parameter. As a result of the t-test applied, the p-value was 0,000174. Thus, the null hypothesis was rejected and it was determined that the change was significant. The roundabout type change had a negative effect on the queue length and speed data, but it was reflected positively on the travel time parameter. The results showed that the transformation of the selected roundabout into a modern roundabout with non-ideal geometrical conditions will not yield positive results in the current traffic conditions and geometric conditions.

As seen in the simulations, the fact that even one road does not comply with the design standards in the modern four-way roundabout model has seriously affected the performance of other roads and reduced the performance of the intersection. This has demonstrated the importance of design standards in modern roundabouts.

References

[1] Coelho, M. C., Farias, T. L., and Rouphail, N. M. (2006). Effect of roundabout operations on pollutant emissions. Transportation Research Part D: Transport and Environment, 11(5), 333–343.

[2] Mandavilli, S., Rys, M. J., and Russell, E. R. (2008). Environmental impact of modern roundabouts. International Journal of Industrial Ergonomics, 38(2), 135–142.

[3] Gross, F., Lyon, C., Persaud, B., and Srinivasan, R. (2013). Safety effectiveness of converting signalized intersections to roundabouts. Accident Analysis & Prevention, 50, 234–241.

[4] Mistry, J., Chaudhari, P., Arkatkar, S., and Antoniou, C. (2022). Examining Traffic Operations at Multi-Legged Intersection Operating under Heterogeneous Traffic: A Case Study in India. Transportation Research Procedia, 62, 83–90.

[5] Dias, C., Abd Rahman, N., Abdullah, M., and Sukor, N. S. A. (2021). Influence of COVID-19 Mobility-Restricting Policies on Individual Travel Behavior in Malaysia. Sustainability, 13(24), 13960.

[6] Basu, R., and Ferreira, J. (2021). Sustainable mobility in auto-dominated Metro Boston: Challenges and opportunities post-COVID-19. Transport Policy, 103, 197–210.

[7] Abdullah, M., Dias, C., Muley, D., and Shahin, M. (2020). Exploring the impacts of COVID-19 on travel behavior and mode preferences. Transportation Research Interdisciplinary Perspectives, 8, 100255.

[8] Dui, H., Chen, S., Zhou, Y., and Wu, S. (2022). Maintenance analysis of transportation networks by the traffic

transfer principle considering node idle capacity. Reliability Engineering & System Safety, 221, 108386.

[9] Olayode, I. O., Tartibu, L. K., and Okwu, M. O. (2021). Prediction and modeling of traffic flow of human-driven vehicles at a signalized road intersection using artificial neural network model: A South African road transportation system scenario. Transportation Engineering, 6, 100095.

[10] Olayode, I. O., Tartibu, L. K., Okwu, M. O., and Ukaegbu, U. F. (2021). Development of a Hybrid Artificial Neural Network-Particle Swarm Optimization Model for the Modelling of Traffic Flow of Vehicles at Signalized Road Intersections. Applied Sciences, 11(18), 8387.

[11] Cakici, Z., & Murat, Y. S. (2019). A Differential Evolution Algorithm-Based Traffic Control Model for Signalized Intersections. Advances in Civil Engineering, 1–16.

[12] Yang, G., Warchol, S., Cunningham, C. M., and Hummer, J. (2022). The potential of signalized offset T-intersections to accommodate new developments. International Journal of Transportation Science and Technology.

[13] Kitali, A. E., and Sando, P. E. T. (2017). A full Bayesian approach to appraise the safety effects of pedestrian countdown signals to drivers. Accident Analysis & Prevention, 106, 327–335.

[14] Mokhtarimousavi, S., Anderson, J. C., Azizinamini, A., and Hadi, M. (2020). Factors affecting injury severity in vehicle-pedestrian crashes: A day-of-week analysis using random parameter ordered response models and Artificial Neural Networks. International Journal of Transportation Science and Technology, 9(2), 100–115.

[15] Murat, Y. S., and Guo, R. (2021). Signalized Roundabouts. In International Encyclopedia of Transportation (pp. 227–237). Elsevier.

[16] Bai, Y., Chen, W., and Xue, K. (2010). Association of Signal-Controlled Method at Roundabout and Delay. In 2010 International Conference on Intelligent Computation Technology and Automation (pp. 816–820). IEEE.

[17] Arafat, M., Nafis, S. R., Sadeghvaziri, E., and Tousif, F. (2020). A data-driven approach to calibrate microsimulation models based on the degree of saturation at signalized intersections. Transportation Research Interdisciplinary Perspectives, 8, 100231.

[18] Bandi, M. M., and George, V. (2020). Microsimulation Modelling in VISSIM on Short-term and Long-term Improvements for Mangalore City Road Network. Transportation Research Procedia, 48, 2725–2743.

[19] Chauhan, B. P., Joshi, G. J., and Parida, P. (2019). Car following model for urban signalised intersection to estimate speed based vehicle exhaust emissions. Urban Climate, 29, 100480.

J Inno Sci Eng,2023, 7(1):13-28
https://doi.org/10.38088/jise.1120186

Research Article

A New Method for Verification and Evaluation of PLC Software

Muhammed A. Öz[1*], Özgür T. Kaymakci [2]

[1] *Yıldız Technical University, Department of Control and Automation Engineering, İstanbul, Turkey*
[2] *Canakkale Onsekiz Mart University, Department of Electrics and Electronics Engineering, İstanbul, Turkey*

Cite this paper as: Muhammed A. Oz and Ozgur T. K. (2023). A New method for verification and evaluation of PLC software. 7(1): 13-28.

*Corresponding author: Ozgur T. Kaykamci

E-mail: okaymakci@comu.edu.tr

Received Date:24/05/2022
Accepted Date:09/09/2022

Availableonline at
http://jise.btu.edu.tr/

Abstract

Varying market demands and changes in production standards require production systems to be effortlessly modifiable and quickly operational. On the other hand, designing, developing, and testing the control system of a new production system prove costly and time-consuming. Therefore, most engineers write code intuitively and apply basic and insufficient tests. Moreover, most of the code developed for industrial control systems is still written manually using the ladder programming language. At the same time, almost all code development platforms support users with only manual test interfaces. This causes the testing process to be very long and laborious. In addition, not all possible input and output combinations of the code can be tested most of the time. This is a serious handicap, especially for safety-related systems. This study aims to develop a reusable and quickly implementable method that will accurately translate RTC program and the behavior of RTC in a modular Petri net model. Through this translated model, the system and safety requirements written in the Computation Tree Logic can be verified. An advantage of this method is that it does not require a plant model which makes it reusable for new plants and provides a quick verification method for code written intuitively. A case study is given to demonstrate the correctness of our method.

Keywords: Industrial automation, Programmable logic controller (PLC), Code verification, Safety.

1. Introduction

Automation systems are an indispensable part of the industry because of their plentiful benefits. Even though these systems save labor, energy, and materials improve quality and accuracy, they have a big disadvantage related to their high initial costs. It takes a fairly long amount of time and resources to design and develop a new automation system. Designing an automation system can be divided into two main tasks. The first task is to choose and assemble the right components for the system. This task is relatively simple when compared with the second task which is to develop a control algorithm and realize it on a real-time controller.

Most developers in the industry follow the V-model when a real-time control system is to be developed [1]. The model includes the steps to take in the process of development, which are requirements, analysis, implementation, testing, verification, and validation. To apply this V-model, the system must be modeled as a discrete event system, after the requirements of the system are collected. A control strategy must be chosen and its result must be converted into real time controller code. Ljungkrantz et al. proposed a method to develop specifications for safety components in PLC programs. [2]. Viera et al. used automata theory to model flexible manufacturing systems consisting of several subsystems and presented a method that allows designers to systematically convert supervisory control theory results into a programmable logic controller code [3]. Hu et al. modeled and analyzed automatic manufacturing systems with synchronous operations using petri nets [4]. Different modeling needs result in a variety of modeling techniques, for scholastic systems a modified petri net called colored stochastic petri nets [5], and for time-critical systems called timed arc Petri nets [6] can be used.

Röshe et al. and Ovatman et al. presented review papers on model based testing approaches [7, 8]. Methods on verification of RTC programs can be classified into two general categories. One of the categories would include the methods where the model to be verified is a combination of the plant model and the model of the RTC program. Bauer et al. presented a method to convert timed sequential functional charts to discrete event timed automata. They also analyzed the converted model UPPAAL [9]. Mertke and Frey worked on Signal Interpreted Petri Nets and presented a new graphical design approach. They implemented the results on a benchmark problem. [10]. Alenlejung et al. introduced the discrete event modeling language Sensor Graphs, which is intended for modeling physical systems from the perspective of a PLC programmer and for usage within formal verification, process observation, and fault detection [11]. Nellen et al. presented two CEGAR-based methodologies for the reachability analysis of SFC-controlled chemical plants [12].

A different approach of including system model is through using simulations. Carlsson et al. used OPC interface in order to connect PLC and a simulation tool. They defined four major problems related to OPC and introduced two possible solutions [13]. Rankin and Jiang developed a platform that provides a flexible simulated testing environment which enables synchronized coupling between the real and simulated world [14]. Park et. al. introduced a visual verification platform based on discrete event systems specifications approach. Here the models can be in a hierarchical, modular manner [15]. Patil et al. presented how integrated circuit (IC) verification method can be used effectively for assuring functional correctness and response time analysis of PLC program [16]. Koo et al. presented a framework of virtual plant models for the verification of PLC logic through modeling and simulation [17]. Although including system model in the verification process increases correctness, it also increases costs and start up time. Besides, this method requires a specialist to model the system and methods are not reusable.

Another way to verify a RTC program is without using a plant model. Wang et al. has proposed a systemic method for

the construction of verification model. PLC system architecture and PLC features has been modeled as components and connectors [18]. Zhang et. al. has proposed a method that generates timed event sequences and implemented this strategy into a program named VETPLC [19]. Adiego et al. propose a general methodology to perform automated model checking of complex properties expressed in temporal logics on PLC programs and is based on an intermediate model [20]. Xiao et al. introduces the compositional verification framework for PLC programs [21]. Ulewicz et al. proposed a novel method for regression verification of PLC code, which allows one to prove that two variants of a plant's software behave identically in specified situations, despite being implemented differently [22]. He et al. proposed a model-based verification of PLC programs using Simulink design [23]. Adiego et al. used PLCverif that was produced by CERN. Here they tried to reveal the bugs in the PLC program that was generated from a functional safety perspective [24]. While the methods above eliminate the need for a system model, they lack the critical components of verification such as readability, modularity and reusability. In addition, the use of intermediate models are also problematic as they require translating the system a few times and decrease the accuracy of the model.

Varying market demands and changes in the production standards require production systems to be effortlessly modifiable and quickly operational. While physical parts of the production system can be built efficiently, designing, developing and testing the control system prove costly and time consuming. Therefore, most engineers write a code out of intuition and apply basic and insufficient tests. The aim of this study is to develop a reusable and quickly implementable method to verify the safety and performance requirements of the respective system. This method will improve modification and development times, financial costs and safety.

Main contribution of this study is to provide a method which accurately translates RTC program and the behavior of RTC in a modular Petri net model. Through this translated model, the system and safety requirements can be verified. An advantage of this method is that it does not require a plant model which makes it reusable for new plants as long as requirements are updated. Petri net models are verified and viewed through TAPAAL, which is a tool for editing, simulating, analyzing and verifying TAPN. The verification process is done on the basis of certain safety requirements, which are written in Computation Tree Logic (CTL), which models time as a tree-like structure, formulation [25], [26]. A general schematic of the proposed method is given in Figure 1.

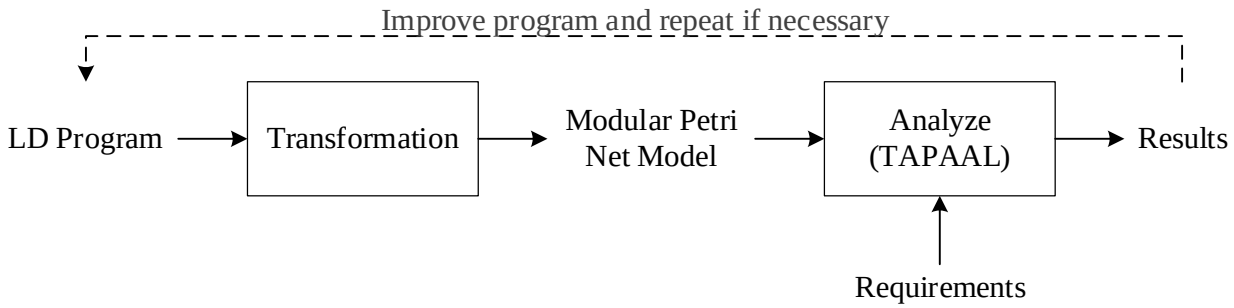

Figure 1. General schematic of the proposed method.

2. Modeling Real Time Controllers

Programmable logic controllers (PLCs) are among the most used RTCs in the industry. PLCs can be defined as cyclic data processors meaning they repeat a predetermined control algorithm indefinitely. The algorithm that is executed cyclically is called the program. To unify the syntax and semantics of programming languages for PLCs, the International Electrotechnical Committee (IEC) published IEC 61131-3. One of the two graphical languages recommended by this standard, the ladder diagram (LD) will be covered in this paper.

2.1. LD program

LD is a programming language that is represented by a graphical diagram based on the circuit diagrams of relay logic hardware. It consists of a main program body and subprograms which perform a specific task and can be called from the main program body. Consider an LD program P having m rungs and n subprograms $P_1, \dots, P_n$ each having m_i, $i = 1, \dots, n$ rungs.

$$P = \{(j, diagram_j) | j = 1, \dots, m\} \cup \bigcup_{i \leq n} P_i$$

Program P can be defined as given in equation where

$$P_i = \left\{ \left(j_i, diagram_{j_i}\right) \middle| j_i = 1, \dots, m_i \right\}, for\ all\ i = 1, \dots, n$$

Where $diagram_j(diagram_{j_i})$ designates the diagram at rung $j(j_i)$ of $P(P_i)$.

2.2. Model of an LD Program

To describe the potential behavior of the program a Petri Net can be used. Let $PN = (\mathrm{P}, \mathrm{T}, \mathrm{F}, \mathrm{W}, M_0)$ be a 5-tuple where, P is a finite set of places, T is a finite set of transitions, the places P and transitions T are disjoint $(P \cap T = \emptyset)$, $F \subseteq (P \times T) \cup (T \times P)$ is the flow relation, $W : F \rightarrow (\mathbb{N} \setminus \{0\})$ is the arc weight mapping, and $M0 : P \rightarrow \mathbb{N}$ is the initial marking representing the initial distribution of tokens. PN model of an LD program can be constructed as follows: Set of places P. $P = P_p + P_b + P_c$

P_p is a set of places expressing the variables of the program defined by the programmer. Although LD supports many data types in this paper only Booleans are discussed as they are most commonly used in the industry. Assuming the main program P_r contains n_{pr} variables and each subprogram P_{ri} contains n_{pri} variables, then $P_p = P_{pr} x P_{pr_2} x \dots x P_{pr_n}$ where $P_{pr} = Pr_{var_1} x Pr_{var_2} x \dots x Pr_{var_{n_{pr}}}$ and $Pr_{var_j} = \{\text{true}, \text{false}\}$ for $j = 1, \dots, n_{pr}$.

P_b is a set of states expressing the behavior of the plc. In this approach, variables that are not defined in the program by the user but are still needed to express some functions such as rising edge trigger. This function requires the previous value of the variable. Thus, a place must be created to store value of the variable. Assuming the main program P_b contains n_b functions as describes above and each subprogram P_{b_i} contains n_{b_i} functions, then $P_b = P_b x P_{b_1} x \dots x P_{b_{n_i}}$ where $P_b = Pb_{var_1} x Pb_{var_2} x \dots x Pb_{var_j}$ and P_b defines the variables needed for expressing all functions in the appropriate subprogram and Pb_{var_j} defines the variables needed for the respective function in that subprogram.

P_c is a set of places defining program counters. The program counter of each of the program modules together to form the set SPC. Thus, $SPC = \{1, \dots, maxpc\} \times \{1, \dots, maxpc1\} \times \dots \times \{1, \dots, maxpcn\}$. Adding the $P_{c_{Reading}}$ a place to define the reading cycle of PLC and $P_{c_{Writing}}$ a place to define the writing cycle of PLC to this set, a PLC behavior can

be accurately modeled.

Flow relation, $F \subseteq (P \times T) \cup (T \times P)$ describes how the tokens of the places change after the firing of each transition. The condition described by the LD diagram is modeled using the firing rule of the transitions and the actual firing of the transition models the action taken as a result of the respective conditional statement. Since this study only deals with logical values of the software, places in the PN model can only have two values, as a result the upper limit of tokens for our Petri net places is one. Here zero tokens express the value false whereas one token expresses the value true. Furthermore, the weights of the arcs must always be set to one considering that places can only contain one token. The Petri net will be self-looping because the input places lose their tokens when transition fires and their tokens must be returned. A Petri net under these terms is called an ordinary, finite-capacity net with strict firing rule.

This study proposes modeling the RTC and its ladder program in three steps. First, rungs of the LD program are modeled one by one as independent model components. Next, a behavioral model of the RTC is generated considering the requirements of the LD program. Finally, model components of LD program and the behavioral model are assembled.

2.3. Model of an LD Program

The logic in a ladder diagram typically flows from left to right. The diagram which resembles a ladder can be divided into sections called rungs. RTC executes these rungs one by one from top to bottom. Each rung typically consists of a combination of input instructions and these instructions lead to a single output instruction. However, rungs may also contain function block instructions. A rung can be tough as a condition and an action taken depending on the condition.

In this example a single rung of a LD program is given in figure A and its corresponding PN model is given Figure 1. The condition on this rung is that P_0 must be true and P_1 must be false. The action taken depending on this condition is setting the output variable P_2 to true. In the case of P_2 being true, meaning it already has a token, after the firing of transitions its token will increase to more than one and this is not acceptable. Therefore, two transitions are needed to take the respective action when the condition is satisfied. Transition T_3 is fired when the previous value of P_2 is false and transition T_2 is fired when previous value of P_2 is true. Notice that in order to complete the execution in the PN model the token of $rung_n$ must be transferred to the place $rung_{n+1}$. Consequently, transitions T_0 and T_1 are used to transfer the token from $rung_n$ to $rung_{n+1}$ when the condition is not satisfied. The components with the dotted line are not necessary to model the code but to model the behavior of the RTC. The places $rung_n$ and $rung_{n+1}$ are members of the program counter set. The place $rung_n$ is used to simulate the RTCs behavior of running the code line by line with order. After $rung_n$ loses its token $rung_{n+1}$ recieves it and executes the PN model of the next rung.

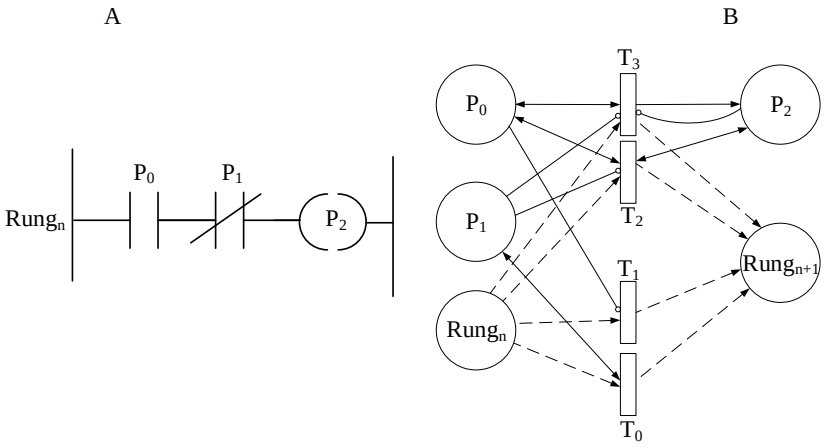

Figure 2. An example of a RTC instruction and its Petri net model correspondence.

An example of a RTC instruction and its corresponding Petri net model is given in Figure 2-A and Figure 2-B. The instruction calculates the conjunction of variable P0 and the complement of variable P1, and writes the result on the output variable P2. In the Petri net correspondence, in addition to the instruction rung indicators are used to run Petri net model components in order just as a RTC. Furthermore, the component must complete the instruction operation in one transition. At the end of the operation next rung indicator must get a token and the input variables must keep their initial values. Petri net correspondences of commonly used instructions are given in the Appendix.

2.4. Model of PLC Scan Cycle

When the scan cycle starts, PLC checks each input card to determine its logical state and saves this information in a data table to be used in the next cycle step. This speeds up the process while avoiding cases where an input changes from the start to the end of the program. The PLC executes programs one instruction at a time using only the memory copy of the inputs. When all instructions are completed, the outputs are updated using the temporary values in memory. The PLC updates the status of the outputs based on which inputs were on during the first step and the results of executing a program during the second step. The PLC now restarts the process by scanning inputs.

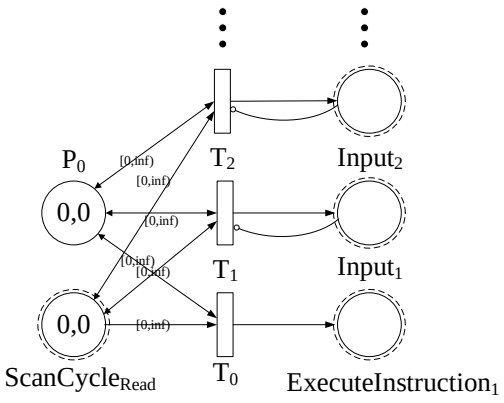

Figure 3. Petri net model of RTC's reading cycle.

Proposed method simulates the same behavior. Each scan cycle stage is indicated by a place and by connecting these places to respective transitions, PLC scan cycle stages and one by one execution of the program instructions can be achieved in the model. Similar to the PLC, the model first determines the logical states of the input places. Software that is being tested should function safely under all conditions. Therefore, the model should allow all input combinations even when they are not possible in the physical system. This is achieved using the PN model component given in Figure 3. This component takes advantage of the firing rules of PNs by enabling many transitions until T_0 transition is fired and all input combinations are possible. The place $ScanCycle_{Read}$ indicates the scan cycle step: read input values. When $ScanCycle_{Read}$ loses its token, the input combination is decided and will stay same until the next cycle. After this cycle stage $ExecuteInstruction_1$, which indicates that first instruction should be executed, receives a token and instructions are executed in order. Each scan cycle step and each instruction is a component of the Petri network and interactions are provided through shared places, and these shared places are shown with two circles where the outer one is dotted. This improves readability, reduces design complexity of the network and pave the way to automatic modeling.

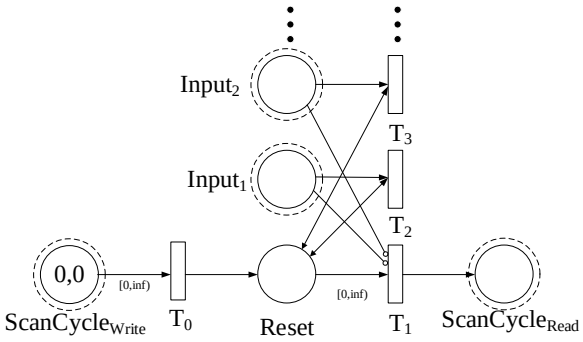

Figure 4. Petri net model of RTC's output cycle.

Last scan cycle is the output cycle and its representation is given in Figure 4. $ScanCycle_{Write}$ is the indicator of this cycle. This model component has two main tasks; the first task is to store the previous input logic states especially for PLC instruction such as rising and falling edge trigger, and the second task is to clear all inputs before going into the reading cycle step using sink transitions, transitions without any output place. This component is also important because it represents when outputs are updated therefore must be kept in mind in the verification process. The values of outputs should only be checked in the output cycle. Model representations of all scan cycle steps are shown in the Figure 5.

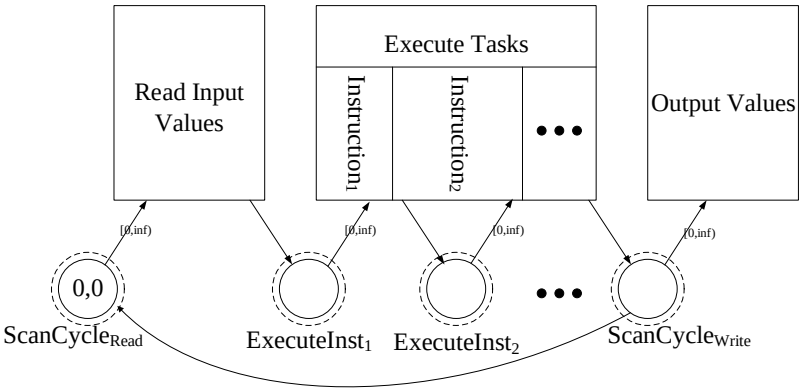

Figure 5. Model representations of all scan cycle steps.

3. Case Study

A program that controls two robot arms which are a sub-system of a production line is used for the case study. A representation of the system is given in Figure 6. There are two conveyors that carry materials inside the subsystem and only one conveyor moves materials out of the system with the guidance of presence sensors. These conveyors are controlled by a different higher level program of the production system. The control program is written for two robot arms which pick up materials when ready from the assigned conveyor and places them on conveyor 3.

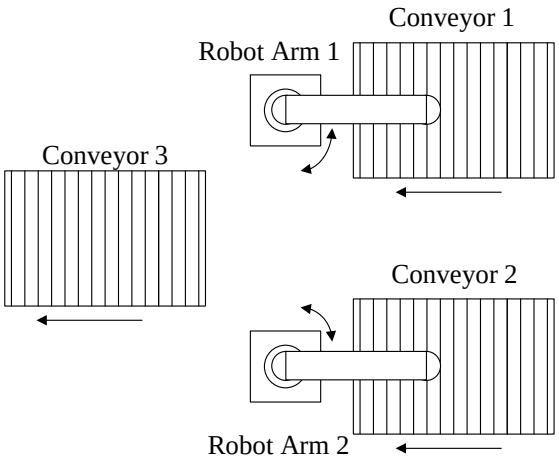

Figure 6. Schematics of the production system.

While the system is idle, which means it is waiting for a detection of a material on either conveyor, the robot arms are in a position above their assigned conveyors with the robot's gripper being at a certain height. When a material is detected on either conveyor, the assigned robot arm lowers itself in order to pick the material with its gripper then goes back to the original height and starts moving in circular motion towards conveyor 3. Once the robot arm lowers its gripper again until it can place the material safely on conveyor 3 and moves back to its original height, it moves towards its assigned conveyor. The process of moving a material is finished once it is in a position above its assigned conveyor.

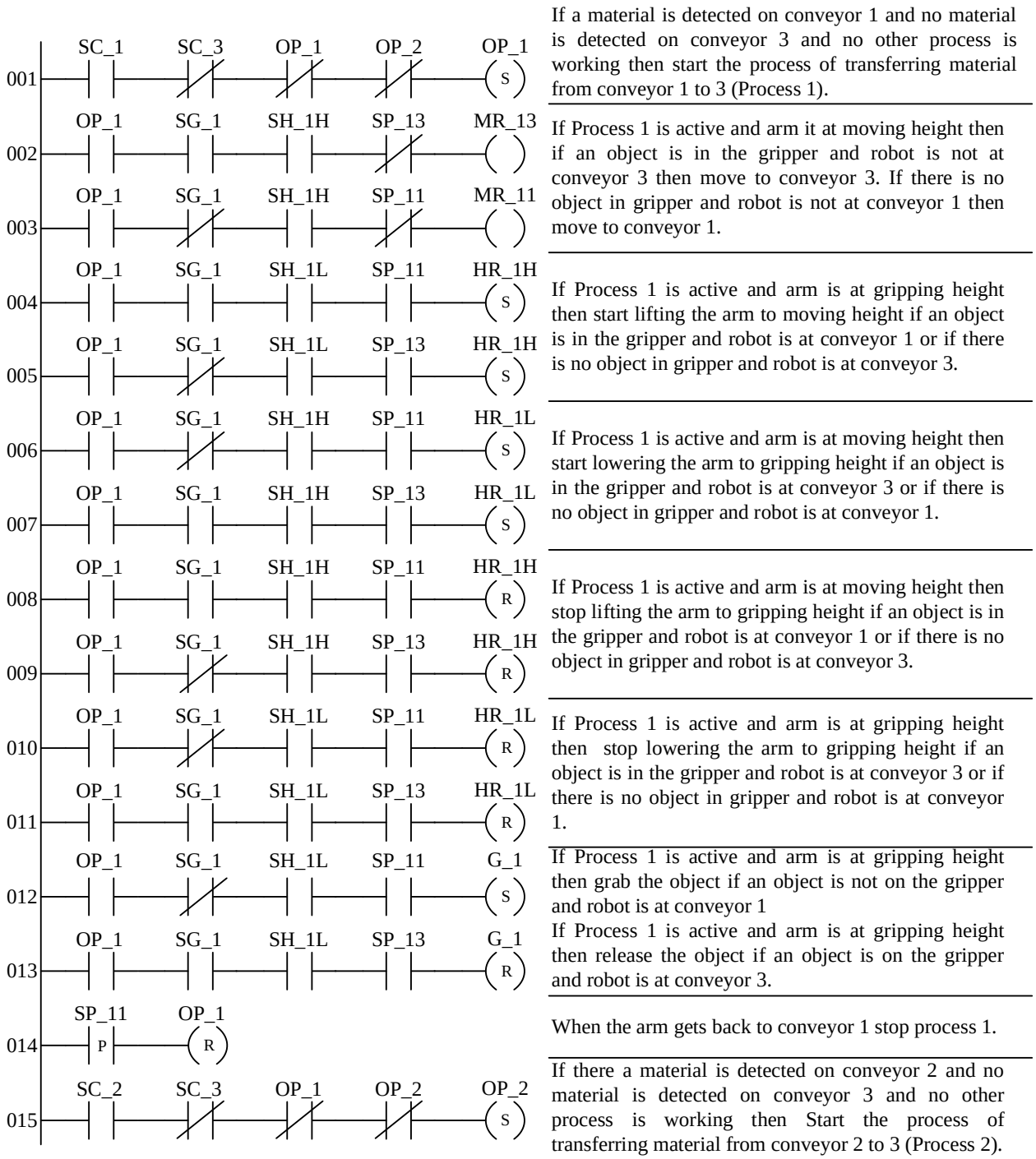

Figure 7. Program for the production system and comments.

PLC code segment that is given in Figure 7 is an intuitively written program for the production line mentioned above. This code segment except the last rung runs one of the robot arms. Rest of the program is just a copy of this segment where the names of the inputs and outputs are changed accordingly to work with the other robot arm hence, space is preserved, and readability is improved for the rest of the program which is not included. The process does not allow two robots operate at the same time. Thus, just adding the last rung is enough to verify that under no circumstance robots work simultaneously. All in all, the whole program can be verified by just verifying the program segment since the robots operate the same. This program was tested on a simulative environment and no mistake or unwanted scenarios were detected. Table 1 presents the lists of the inputs and the outputs used in the PLC code that will be verified using the proposed method in this paper.

Table 1. Verification result before and after correction.

Sensor Inputs	
SC_x	Material presence detection on conveyor x *(x={1,2,3})*
SP_x1	Robot arm *x* is in position to pick materials from conveyor *x (x={1,2})*
SP_x3	Robot arm *x* is in position to place materials on conveyor 3 *(x={1,2})*
SH_xL	Robot arm *x* is at the appropriate height to pick and place materials *(x={1,2})*
SH_xH	Robot arm *x* is at the appropriate height to move materials *(x={1,2})*
SG_x	Robot arm *x* is holding a material *(x={1,2})*
Control Outputs	
MR_x1	Move the robot arm x towards the assigned conveyor *x (x={1,2})*
MR_x3	Move the robot arm x towards conveyor *3 (x={1,2})*
G_x	Controls the pick and place process of robot arm *x (x={1,2})*
MH_xL	Decreases the height of the robot x gripper *(x={1,2})*
MH_xH	Decreases the height of the robot x gripper *(x={1,2})*
Intermediate Variables	
OP_x	Starts the process of transferring material from conveyor *x* to conveyor 3 *(x={1,2})*

3.1. Transformation

Using the proposed approach, this program is transformed into a modular TAPN model so that each rung of the code is a counterpart to a component of the model. This property simplifies modeling and increases the readability of the model which is useful when searching for errors in the code. TAPAAL, a software tool for modeling and verifying TAPN models, is used in this case study.

All transformation steps are standardized and ordered, which make automating the transformation process possible. First, reading and writing cycles of the RTC are modeled using the variables of the program. Next, rungs of the program are transformed beginning with the places associated with the controller's operation cycle, such as program counter, being implemented into the model component. Variables used in the rung are added as places into the model and with the help of a transition the update of the output is simulated. Even though a transition is enough for this process other combinations are implemented to ensure that the token is transferred between program counter places. Only a few components of the resulting model is given here to preserve space. Transformed TAPN model component of rung 6 is given in Figure 8 part A and transformed TAPN model component of rung 14 combined is given in Figure 8 part B.

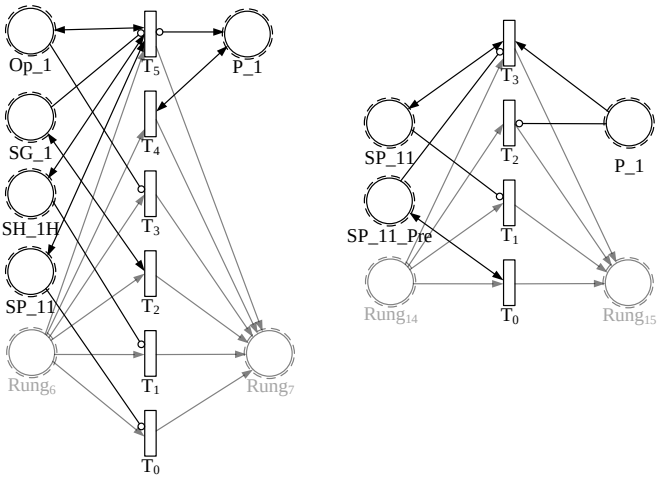

Figure 8. The TAPN model of some rungs.

In the component TAPN model of rung 6, transition named T_5 fires when the right combination of input values that set P_1 variable are present. T_4 transition is there to keep P_1 place from receiving more than one token, which is an unwanted situation. Any other combination of input values will fire one of the other transitions to transfer the token to the next program rung. TAPN Model component of the Rung 14 is very similar.

3.2. Verification and Correction

To ensure the reliable operation of this system, some safety features must be maintained. These safety requirements are added to the model with the help of Tapaal editor using Computer Tree Logic (CTL) formulation. CTL logic is a branching-time logic. CTL logic formulas are evaluated over all possible paths of a Kripke structure. To verify the formulized requirements Tapaal translates the TAPN model into Network of Timed Automata (NTA) and use Uppaal verification on the produced NTA. All queries are checked via Tapaal Discrete Verification method based on the Breadth First search order in state space. As the coverability tree is too large, it is not given in the study. Since the model simulates a PLCs working behavior, outputs are formulized with scan cycle write place added. Safety requirements of the system are given below with the corrections if the requirement is not satisfied.

SR1: The two robot arms must not operate concurrently. Since robots have overlapping operation routes, to avoid a possible and highly likely to occur collision, concurrent working must not be allowed.

$$AG\neg(ScanCycle_{write} \geq 1 \wedge OP\_1 \geq 1 \wedge OP\_2 \geq 1)$$

SR2: The robot arms cannot move horizontally while moving up. Difference between the heights of the conveyors can cause robot extremities to collide with the conveyor.

$$AG\neg(ScanCycle_{write} \geq 1 \wedge MH\_1L \geq 1 \wedge (MP\_10 \geq 1 \vee MP\_11 \geq 1))$$

SR3: The robot arms cannot move horizontally while moving down. Just like safety requirement 2, difference between the heights of the conveyors can cause robot extremities to collide with the conveyor.

$$AG\neg(ScanCycle_{write} \geq 1 \wedge MH\_1H \geq 1 \wedge (MP\_10 \geq 1 \vee MP\_11 \geq 1))$$

SR4: The robot gripper must not try to place its load while moving to conveyor 3. This can cause defective products, which means high cost depending on the value of the material being carried.

$$AG\neg(ScanCycle_{write} \geq 1 \wedge MP_{13} \geq 1 \wedge SG\_1 = 0)$$

SR5: The robot gripper must not try to place its load while moving to conveyor 3. This can cause defective products,

which means high cost depending on the value of the material being carried.

$$AG\neg(ScanCycle_{write} \geq 1 \wedge MP_{13} \geq 1 \wedge SG\_1 = 0)$$

SR6: Robot must not move down to place its load when a product is present on conveyor 3. Same as safety requirement 4, this event can cause defective products, even worst it can cause damage to robots or the conveyor.

$$AG\neg(ScanCycle_{write} \geq 1 \wedge MH\_1L \geq 1 \wedge SP\_11 \geq 1 \vee SC\_3 \geq 1)$$

SR7: The robot should not carry a load while all conveyors are occupied. This event is referred to as a deadlock in the system where all allowed actions are blocked.

$$AG\neg(ScanCycle_{write} \geq 1 \wedge SC\_3 \geq 1 \wedge SC\_1 \geq 1 \wedge OP\_1 \geq 1)$$

Table 2. Verification Result Before and After Correction.

S. R. No	*Name of Safety Requirement*	*Verification Before Correction*			*Verification After Correction*		
		Mb	*Second(s)*	*Result*	*Mb*	*Second(s)*	*Result*
1	*Concurrent Working*	*43*	*0.021*	✓	*25*	*0.53*	✓
2	*Unauthorized Movement Up*	*43*	*0.085*	✗	*24*	*0.534*	✓
3	*Unauthorized Movement Down*	*23*	*0.223*	✗	*25*	*0.535*	✓
4	*Misplace*	*43*	*0.813*	✓	*24*	*0.53*	✓
5	*Lock*	*0*	*0.114*	✗	*26*	*0.517*	✓
6	*Collision*	*0*	*0.049*	✗	*0*	*0.546*	✓
7	*Deadlock*	*0*	*0.054*	✗	*0*	*0.051*	✗
System Info	*Intel Core I7-2630QM Cpu @2,00 Ghz x64* *6 Gb Ram* *Windows 10 64-Bit*						
Verification tool	*TAPAAL 3.9.1*						

The power of this method comes from its straightforward application and ability to find errors that can be very rare or even caused by faulty sensors. Within the case study, intuitively written program, which was tested before with no errors, failed to satisfy almost all requirements except safety requirement 1 and 4. After verification, the results can be used to correct the program. Failure to satisfy requirement 2 and 3 means that unnecessary variables are used in rung 8 through 11, which can prevent robot from stopping under rare circumstances. Requirement 5 indicates that rung 8 through 11 and 13 fails at resetting when OP_1 is false due to the fact that before operation resets anyone of the set functions can be activated with no way to reset. Requirement 6 points out an obvious error where rungs, which run, place operation does not include information from the sensor of conveyor 3. Corrected versions of these rungs are given in Figure 9.

Since conveyors are under control of another control system, the possibility of a deadlock cannot be evaded by changing the program at hand. But since conveyors only carry materials in one direction the deadlock will not be permanent.

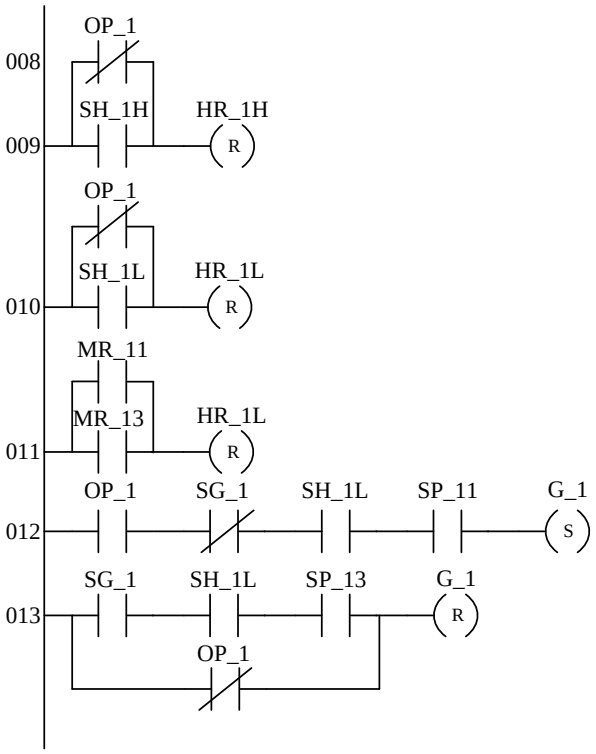

Figure 9. Corrected versions of faulty rungs.

4. Conclusion

Today, most of the code still developed for industrial control systems is written manually, usually using the ladder programming language. Although most of the code developed for industrial automation systems is based on basic logic relations, when the number of inputs and outputs and their possible combinations are considered, the entire code cannot be tested. Generally, the process is progressed with test scenarios based on white box testing and black box testing strategies. For this reason, code development platforms are content with developing interfaces where relevant test scenarios can be run according to these strategies. On the other hand, showing that the safety-related code meets the relevant safety conditions and proving that these conditions are met in all possible combinations will be a very valuable output for the safety of the process.orship) are not allowed. After receipt of the corrected proofs, the article in PDF format will be published online.

References

[1] Zhou, M.; Wan, H.; Wang, R.; Song, X.; Su, C.; Gu, M.; Sun, J. (2013). Formal component-based modeling and synthesis for PLC systems, *Computers in Industry*, Vol. 64, No. 8, 1022–1034. doi:10.1016/j.compind.2013.07.003

[2] Ljungkrantz, O.; Akesson, K.; Yuan, C.; Fabian, M. (2012). Towards Industrial Formal Specification of Programmable Safety Systems, *IEEE Transactions on Control Systems Technology*, Vol. 20, No. 6, 1567–1574Presented at the IEEE Transactions on Control Systems Technology. doi:10.1109/TCST.2011.2169262

[3] Vieira, A. D.; Santos, E. A. P.; de Queiroz, M. H.; Leal, A. B.; de Paula Neto, A. D.; Cury, J. E. R. (2017). A Method for PLC Implementation of Supervisory Control of Discrete Event Systems, *IEEE Transactions on Control Systems Technology*, Vol. 25, No. 1, 175–191Presented at the IEEE Transactions on Control Systems Technology.

doi:10.1109/TCST.2016.2544702

[4] Chen, C.; Hu, H. (2015). Maximally permissive distributed control of automated manufacturing systems with assembly operations using Petri nets, *2015 IEEE International Conference on Automation Science and Engineering (CASE)*Presented at the 2015 IEEE International Conference on Automation Science and Engineering (CASE), , 532–538. doi:10.1109/CoASE.2015.7294134

[5] List, G. F.; Mashayekhi, M. (2016). A Modular Colored Stochastic Petri Net for Modeling and Analysis of Signalized Intersections, *IEEE Transactions on Intelligent Transportation Systems*, Vol. 17, No. 3, 701–713Presented at the IEEE Transactions on Intelligent Transportation Systems. doi:10.1109/TITS.2015.2483324

[6] Wang, X.; Mahulea, C.; Silva, M. (2013). Fault Diagnosis Graph of time Petri nets, *2013 European Control Conference (ECC)*Presented at the 2013 European Control Conference (ECC), , 2459–2464. doi:10.23919/ECC.2013.6669417

[7] Rösch, S.; Ulewicz, S.; Provost, J.; Vogel-Heuser, B. (2015). Review of Model-Based Testing Approaches in Production Automation and Adjacent Domains—Current Challenges and Research Gaps, *Journal of Software Engineering and Applications*, Vol. 08, No. 09, 499–519. doi:10.4236/jsea.2015.89048

[8] Ovatman, T.; Aral, A.; Polat, D.; Ünver, A. O. (2016). An overview of model checking practices on verification of PLC software, *Software & Systems Modeling*, Vol. 15, No. 4, 937–960. doi:10.1007/s10270-014-0448-7

[9] Bauer, N.; Engell, S.; Huuck, R.; Lohmann, S.; Lukoschus, B.; Remelhe, M.; Stursberg, O. (2004). Verification of PLC Programs Given as Sequential Function Charts, H. Ehrig; W. Damm; J. Desel; M. Große-Rhode; W. Reif; E. Schnieder; E. Westkämper (Eds.), *Integration of Software Specification Techniques for Applications in Engineering: Priority Program SoftSpez of the German Research Foundation (DFG), Final Report*, Springer, Berlin, Heidelberg, 517–540. doi:10.1007/978-3-540-27863-4_28

[10] Mertke, T.; Frey, G. (2001). Formal verification of PLC programs generated from signal interpreted Petri nets, *2001 IEEE International Conference on Systems, Man and Cybernetics. e-Systems and e-Man for Cybernetics in Cyberspace (Cat.No.01CH37236)* (Vol. 4)Presented at the 2001 IEEE International Conference on Systems, Man and Cybernetics. e-Systems and e-Man for Cybernetics in Cyberspace (Cat.No.01CH37236), , 2700–2705 vol.4. doi:10.1109/ICSMC.2001.972974

[11] Alenljung, T.; Lennartson, B.; Hosseini, M. N. (2012). Sensor Graphs for Discrete Event Modeling Applied to Formal Verification of PLCs, *IEEE Transactions on Control Systems Technology*, Vol. 20, No. 6, 1506–1521Presented at the IEEE Transactions on Control Systems Technology. doi:10.1109/TCST.2011.2168607

[12] Nellen, J.; Driessen, K.; Neuhäußer, M.; Ábrahám, E.; Wolters, B. (2016). Two CEGAR-based approaches for the safety verification of PLC-controlled plants, *Information Systems Frontiers*, Vol. 18, No. 5, 927–952. doi:10.1007/s10796-016-9671-9

[13] Carlsson, H.; Svensson, B.; Danielsson, F.; Lennartson, B. (2012). Methods for Reliable Simulation-Based PLC Code Verification, *IEEE Transactions on Industrial Informatics*, Vol. 8, No. 2, 267–278Presented at the IEEE Transactions on Industrial Informatics. doi:10.1109/TII.2011.2182653

[14] Rankin, D. J.; Jiang, J. (2011). A Hardware-in-the-Loop Simulation Platform for the Verification and Validation of Safety Control Systems, *IEEE Transactions on Nuclear Science*, Vol. 58, No. 2, 468–478Presented at the IEEE Transactions on Nuclear Science. doi:10.1109/TNS.2010.2103325

[15] Park, S. C.; Park, C. M.; Wang, G.-N.; Kwak, J.; Yeo, S. (2008). PLCStudio: Simulation based PLC code

verification, *2008 Winter Simulation Conference*Presented at the 2008 Winter Simulation Conference, , 222–228. doi:10.1109/WSC.2008.4736071

[16] Patil, M. M.; Subbaraman, S.; Joshi, S. (2011). Exploring Integrated Circuit Verification Methodology for Verification and Validation of PLC Systems, *2011 International Symposium on Electronic System Design*Presented at the 2011 International Symposium on Electronic System Design, , 88–93. doi:10.1109/ISED.2011.47

[17] Koo, L.-J.; Park, C. M.; Lee, C. H.; Park, S.; Wang, G.-N. (2011). Simulation framework for the verification of PLC programs in automobile industries, *International Journal of Production Research*, Vol. 49, No. 16, 4925–4943. doi:10.1080/00207543.2010.492404

[18] Wang, R.; Guan, Y.; Luo, L.; Song, X.; Zhang, J. (2013). Formal Modelling of PLC Systems by BIP Components, *2013 IEEE 37th Annual Computer Software and Applications Conference*Presented at the 2013 IEEE 37th Annual Computer Software and Applications Conference, , 512–518. doi:10.1109/COMPSAC.2013.85

[19] Zhang, M.; Chen, C.-Y.; Kao, B.-C.; Qamsane, Y.; Shao, Y.; Lin, Y.; Shi, E.; Mohan, S.; Barton, K.; Moyne, J.; Mao, Z. M. (2019). Towards Automated Safety Vetting of PLC Code in Real-World Plants, *2019 IEEE Symposium on Security and Privacy (SP)*Presented at the 2019 IEEE Symposium on Security and Privacy (SP), , 522–538. doi:10.1109/SP.2019.00034

[20] Fernández Adiego, B.; Darvas, D.; Viñuela, E. B.; Tournier, J.-C.; Bliudze, S.; Blech, J. O.; González Suárez, V. M. (2015). Applying Model Checking to Industrial-Sized PLC Programs, *IEEE Transactions on Industrial Informatics*, Vol. 11, No. 6, 1400–1410Presented at the IEEE Transactions on Industrial Informatics. doi:10.1109/TII.2015.2489184

[21] Xiao, L.; Li, M.; Gu, M.; Sun, J. (2014). A hierarchy framework on compositional verification for PLC software, *2014 IEEE 5th International Conference on Software Engineering and Service Science*Presented at the 2014 IEEE 5th International Conference on Software Engineering and Service Science, , 204–207. doi:10.1109/ICSESS.2014.6933545

[22] Ulewicz, S.; Vogel-Heuser, B.; Ulbrich, M.; Weigl, A.; Beckert, B. (2015). Proving equivalence between control software variants for Programmable Logic Controllers, *2015 IEEE 20th Conference on Emerging Technologies Factory Automation (ETFA)*Presented at the 2015 IEEE 20th Conference on Emerging Technologies Factory Automation (ETFA), , 1–5. doi:10.1109/ETFA.2015.7301603

[23] He, N.; Oke, V.; Allen, G. (2016). Model-based verification of PLC programs using Simulink design, *2016 IEEE International Conference on Electro Information Technology (EIT)*Presented at the 2016 IEEE International Conference on Electro Information Technology (EIT), , 0211–0216. doi:10.1109/EIT.2016.7535242

[24] Adiego, B. F.; Lopez-Miguel, I. D.; Tournier, J.-C.; Blanco, E.; Ladzinski, T.; Havart, F. (2022). Applying Model Checking to Highly-Configurable Safety Critical Software: The SPS-PPS PLC Program, *Proceedings of the 18th International Conference on Accelerator and Large Experimental Physics Control Systems*, Vol. ICALEPCS2021, 5 pages, 0.178 MB. doi:10.18429/JACoW-ICALEPCS2021-WEPV042

[25] Ljungkrantz, O.; Akesson, K.; Fabian, M.; Yuan, C. (2010). Formal Specification and Verification of Industrial Control Logic Components, *IEEE Transactions on Automation Science and Engineering*, Vol. 7, No. 3, 538–548Presented at the IEEE Transactions on Automation Science and Engineering. doi:10.1109/TASE.2009.2031095

[26] Bel Mokadem, H.; Bérard, B.; Gourcuff, V.; De Smet, O.; Roussel, J.-M. (2010). Verification of a Timed Multitask System With Uppaal, *IEEE Transactions on Automation Science and Engineering*, Vol. 7, No. 4, 921–932Presented at the IEEE Transactions on Automation Science and Engineering. doi:10.1109/TASE.2010.2050199

J Inno Sci Eng,2023, 7(1):29-39
https://doi.org/10.38088/jise.1142634

Research Article

A Contactless Palmprint Imaging System Design Using MediaPipe Hands

Mustafa Kocakulak[1*], Nurettin Acir[2]

[1*] *Department of Mechatronics Engineering, Bursa Technical University, 16310 Bursa, Turkey*
[2] *Department of Electronic Engineering, National Defence University, 34334 İstanbul, Turkey*

Cite this paper as:
Kocakulak, M. and Acır, N. (2023). *A Contactless Palmprint Imaging System Design Using MediaPipe Hands*. Journal of Innovative Science and Engineering.7(1):29-39

*Corresponding author: Mustafa Kocakulak
E-mail: mustafa.kocakulak@btu.edu.tr

Received Date:08/07/2022
Accepted Date:18/10/2022

Abstract

Palmprint has been widely used in biometric systems because of its durability and reliability. To avoid recognition performance degradation, dynamic region of interest extraction is a critical step for these systems. In this study, a low-cost contactless palmprint imaging system has been designed and a dynamic region of interest extraction method has been applied to palmprints using the MediaPipe Hands framework. Since the need for hygienic touchless systems has been realized in the post-COVID-19 pandemic world, a low-cost imaging system has been proposed to capture the user's hand at a distance without touching any platform. The region of interest of the user's palmprints in a real-time video stream has been extracted dynamically. This study creates a paradigm for future studies on palmprint imaging. With conducted experiments, the potential of MediaPipe Hands in terms of speed and accuracy on mobile palmprint imaging applications has been realized on Raspberry Pi 4. This work demonstrates that the employed hardware and proposed hand-tracking algorithm are suitable for designing low-cost contactless palmprint imaging systems in non-controlled ambient light conditions. For recognition purposes, a database will be released soon.

Keywords: Contactless biometrics, Imaging system, MediaPipe Hands, Palmprint, Region of interest.

1. Introduction

Hand-based biometric traits such as fingerprint, finger vein, palm vein, and palmprint have received much attention in recent years. Owing to the low-cost and user-friendly structure of image-capturing platforms, these biometric features have been deemed promising and popular [1]. Among these traits, palmprint provides extra advantages. Palmprint requires neither high-resolution images nor complex imaging platform designs. Palmprint patterns can be observed despite the low-image resolution [2]. For real-time mobile applications, low palmprint image resolution provides a small storage need and short computation time [3]. Moreover, a palmprint is robust against spoofing attacks since a user can hardly ever leaves palmprint information unintentionally on touched platforms compared to a fingerprint [4]. With extracted palmprint information by a determined area of palm as a region of interest (ROI) for feature extraction, biometric systems ensure minimum biometric information loss and maximum recognition accuracy at the same time. However, it is not easy to extract palmprint ROI dynamically due to the varying orientation of the hand on the imaging platform and variations in the user's hand size [3].

Dynamic extraction of the region that contains biometric information accurately is a key preprocessing step to increase recognition performance [5]. Evaluation of the extracted ROI rather than the whole acquired image provides shorter processing time and lower memory usage. Researchers have proposed various solutions for ROI localization in the literature. As the main steps of ROI localization, hand boundary detection, and palm region extraction on the detected hand can be listed [5]. There are roughly 3 hand boundary detection methods used for palmprint images: predefined window-based methods, mask-based methods, and threshold-based methods. These methods achieve considerable performance despite possessing some drawbacks. Predefined window-based methods do not possess an adaptive structure not to be affected by changes in the user's hand size and variations in hand orientation [6]. Mask-based methods are vulnerable to background noise while detecting hand boundaries [6]. Lastly, threshold-based methods are severely affected by unevenly distributed illumination of the imaging environment [7]. All these methods are commonly in use for the extraction of ROI of existing publicly available palmprint datasets. However, none of these methods can detect the hand boundary perfectly. To overcome these drawbacks and provide adaptive solutions to ROI extraction, some ROI extraction methods have been proposed in the literature.

Li et al. [8] utilized a maximum inscribed circle. Rather than a rectangle-based positioning, they used a circle-based segmentation approach. They maximized the extracted ROI by increasing the radius of the extracted region from the center of the palm to the contour of the palm. Poon et al. [9] used the finger web between the index finger and middle finger and the finger web between the middle finger and ring finger to extract ROI dynamically. They utilized one of these 2 webs as an axis on which the maximum square region is centered. They proposed using elliptical half-rings to avoid rotational errors on extracted ROI images. Wang et al. [10] extracted the contour of the hand with a Sobel filter. They calculated the distance between the midpoint of the wrist and each point of the contour to find corresponding valleys in the distance profile while extracting ROI. Thus, they tried to ensure a hand-size invariant solution for a robust ROI extraction. Lin et al. [11] showed the effectiveness and usability of ROI extraction methods on palmprint and palm vein images. By utilizing preprocessing operations before extracting ROI with maximum inscribed circle and centroid methods, they presented a robust extraction for palm vein and palmprint. Jaswal et al. [12] proposed a novel ROI extraction method using Bresenham's line algorithm. They extracted ROI by drawing a square with the longest possible side using the base points at the finger bottoms. They evaluated the performance of the proposed method on 3 different

databases. Yan et al. [13] presented a robust solution for palm ROI extraction using a video stream. The imaging system located the position of the palm using a different color space in grabbed video frames dynamically. Kocakulak and Acır [14] proposed using Google's MediaPipe Hands framework for finding reference points on images of the IIT Delhi Touchless Palmprint Database. They used MediaPipe Hands for dynamic ROI extraction and avoided the cumbersome structure of conventional hand boundary detection methods. They reduced the required time for ROI extraction on this dataset considerably with the help of the lightweight structure of MediaPipe Hands while having accurate and adaptive results.

Based on the review of existing ROI extraction methods, MediaPipe Hands, which is a machine learning-based hand tracking framework and is commonly used for gesture recognition and hand-based augmented reality applications, has been utilized to extract ROI dynamically. Since quicker and more hygienic solutions are expected from touchless systems with more degrees of freedom for the placement of the hand, the proposed imaging system on Raspberry Pi with a web camera has been utilized in this framework. Despite varying illumination and hand rotation on the imaging platform, MediaPipe localizes the hand and finds the reference points on the user's hand for dynamic ROI extraction consistently owing to being well-trained with annotated images [15]. This framework provides a novel solution that has 2 hidden models working together. The first model detects the palm side on a full-hand image, and the second model finds the coordinates of 21 reference points on the detected palm.

The rest of this paper is organized as follows: Section 2 presents existing palmprint datasets and contactless palmprint acquisition devices in the literature. Section 3 introduces the proposed contactless palmprint acquisition system and describes the utilized ROI extraction method in detail. Section 4 presents the conducted experiments for this extraction method on the designed device. Lastly, Section 5 concludes this paper with an outlook on future works.

2. Related Works

2.1. Databases

With the recent studies on palmprint imaging technology, the number of publicly available datasets has increased. In Table 1, some publicly available palmprint databases are listed. In near future, a publicly available palmprint database will be released using the proposed design in this study. The number of subjects and samples will be sufficient compared to the listed datasets to meet the needs of deep learning-based applications.

Table 1. Public Palmprint Databases.

Datasets	Number of Subjects	Number of Images	Image Format
CASIA Palmprint Image Database [16]	312	5502	JPEG
CASIA Multispectral Palmprint Database [17]	100	7200	JPEG
PolyU-IITD Contactless Palmprint Database [18]	600	12000	BMP
IIT Delhi Touchless Palmprint Database [19]	230	2601	BMP
Tsinghua Palmprint Database [20]	80	1280	JPEG

2.2. Contactless Acquisition Device Designs

In this section, some of the contactless palmprint imaging devices are listed. Chen et al. [21] designed a system to illuminate palmprints with a digital camera and 23-watt lights which are positioned appropriately. They proposed a low-cost and touchless acquisition mechanism to capture palmprint and hand shape simultaneously. Hao et al. [17] built a multispectral imaging system. They used a group of LEDs and switched them sequentially to collect data under different lighting conditions. Using multispectral imaging techniques on a contactless imaging platform via a dedicated device, they evaluated the effect of multispectral imaging on the obtained verification performance. Kumar [19] utilized fluorescent light to illuminate palmprints in a semi-closed box. Using a pegless design, the palmprint images were captured despite not being user-friendly and narrow box design. Poinsot et al. [22] used a web camera and they captured palmprint images under natural light without any lighting equipment. In a controlled environment using green background, they located the user's hand and extracted palmprint images. Michael et al. [23] built a palmprint imaging system with a low-cost web camera and a 9-watt light bulb inside a semi-closed box. Without any markers and gloves, ROI images of palmprint and knuckle print were captured. Using a black box as an enclosure, they tried to avoid the negative effect of background light reflection. Ferrer et al. [24] designed a biometric system that works fine under visible light and infrared light owing to its bi-spectral structure. They used 2 low-cost web cameras to capture hand geometry and palmprint at the same time. Morales et al. [25] designed a multisampling image acquisition device that captures images of a hand with vertical movement between two plates. With its contactless structure, the proposed design could capture hand shape and palmprint images to increase the obtained performance using multimodality. Aykut and Ekinci [26] developed a system using a low-cost CCD camera with an iris lens. With the proposed design by fixing the distance between the camera and the user's hand, they resolved the problem of the varying distance between the user's hand and the camera. Xiao et al. [27] designed a low-cost palmprint acquisition device under natural light using a semi-closed box structure. This device captures the whole hand-based acquisition rather than part hand-based acquisition. Liang et al. [28] built an acquisition device to take high-quality palmprint images. Using a binocular CMOS camera, the imaging system captured the user's palm vein and palmprint simultaneously. They used a height reference to make volunteer subjects place their hand. We have designed a system by considering the main advantages and disadvantages of these listed imaging devices. In this study, the distance between the user's hand and the camera has been calculated and fixed with the help of the image projected on the tablet screen with a software solution. This provides a user-friendly structure while guiding users on the imaging platform. Without using any closed or semi-closed box, palmprint images have been captured using a low-cost camera which enables a low-cost system design. With a low-cost camera and MediaPipe Hands framework, palmprint image samples have been collected in real-time under natural light. Thus, the design system has worked accurately without using any lighting equipment. The details of the proposed palmprint acquisition device are given in the next section.

3. Results and Discussion Design and Implementation of Acquisition Device

3.1. Experimental Setup

The experimental setup is shown in Figure 1. The image acquisition hardware consists of a processing unit, camera, and tablet screen. We have used Raspberry Pi 4 Model B and Raspberry Pi Camera V2.1 since they have a low-cost and

compact design. The camera has been mounted on a tripod to capture the hands. The camera and the user's hand have been placed both on top of a table to capture effective images. First, images are captured with the camera. Then the user's hand distance to the camera is calculated and the hand image is processed with the help of the MediaPipe Hands framework on Raspberry Pi. Lastly, extracted images are monitored on the tablet screen.

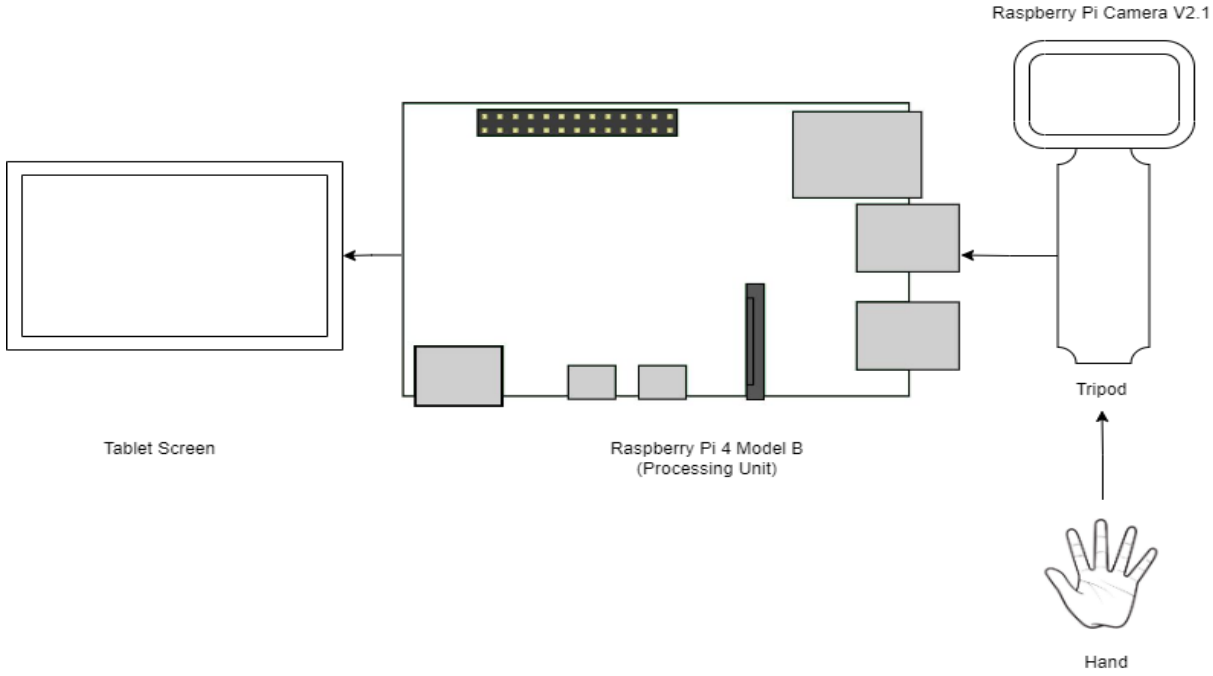

Figure 1. The experimental setup

3.2. Proposed ROI Extraction Method

The proposed dynamic ROI extraction method has 5 major steps. These steps are shown in the block diagram in Figure 2.

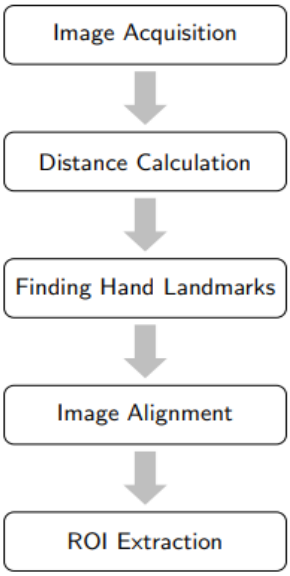

Figure 2. Primary steps in the proposed method

3.2.1. Image Acquisition

The webcam captures palmprint images in a continuous video stream. The user can freely place his hand across the camera and he can move his hand during the acquisition.

3.2.2. Distance Calculation

A Python-based software solution has been used to give feedback to the users about the positioning of the hand. Using the hand landmarks provided by the MediaPipe Hands framework, the position of the index finger, middle finger, and ring finger is fixed. The positions of the knuckles of these fingers are tracked. After getting positional approval from these 3 fingers with color indicators on the screen, the ROI extraction process for palmprint continues with distance calculation. To find the distance between the hand and the camera, firstly the hand is detected by the MediaPipe Hands. If the hand is present on the platform, landmark 5 and landmark 17 are used to calculate the actual distance in centimeters. Based on the distance between the x and y pixel coordinate values of these 2 landmarks, the Euclidean distance is calculated so as not to deal with rotation problems while finding the actual distance accurately. By defining a quadratic function to find the relation between the Euclidean distance of landmarks and their corresponding actual camera distance, the actual distance is estimated roughly with the help of curve fitting. The tablet screen is used to display the real-time video stream of the capture. Thus, the distance between the user's hand and the camera is fixed without using any physical distance sensor.

3.2.3. Finding Hand Landmarks

MediaPipe Hands is an open-source framework developed by Google to estimate the coordinates of 21 hand landmarks from a web camera [15]. These landmarks are enumerated as shown in Figure 3.

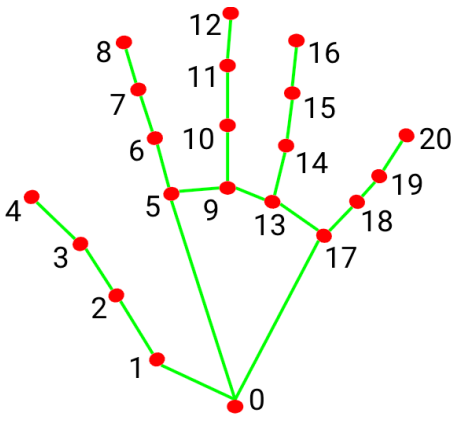

Figure 3. Hand landmarks of MediaPipe Hands [29]

MediaPipe Hands is mainly used for hand-tracking purposes on video data by estimating the pixel coordinates of these landmarks from 2D images. Roughly, MediaPipe Hands consists of 2 machine-learning pipelines. These are the palm detection model and hand landmarking model [29]. However, MediaPipe Hands hides the complexity of these 2 models and provides a lightweight solution. With its well-trained and considerably robust model in hand detection, it can catch hand landmarks even in extreme cases. Since it has a quick response time, it has been used to get the coordinates of each

landmark while extracting dynamic ROI from the acquired video stream as shown in Figure 4. Without any parameter adjustment, the vanilla version of this framework has been applied to the real-time video stream.

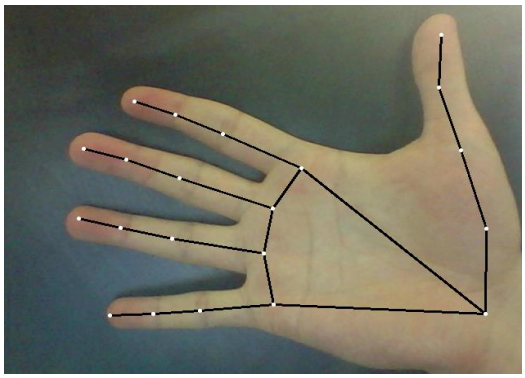

Figure 4. Detected hand landmarks on video data

3.2.4. Image Alignment

In the real-time video stream, hand displacement exists due to touchless and unguided imaging system preference. Hand displacement can be clarified as a case where the middle finger does not parallel the y-axis. For these images, hand displacement adjustment is conducted according to the extracted landmark of the middle finger to avoid the loss of a portion of the palm area in the ROI extraction. By using the angle between landmark 5 and landmark 9, or the angle between landmark 17 and landmark 9, the candidate rotation angles are computed. The greater of 2 angles to estimate the alignment angle is preferred. So the rotation angle θ can be computed as in Equation 1 [30]. In this equation, x_1, y_1 are the coordinates of landmark 9 and x_2, y_2 are the coordinates of landmark 5 or landmark 17.

$$\theta = \left(\frac{y_2 - y_1}{x_2 - x_1}\right)\left(\frac{180}{\pi}\right) \quad (1)$$

3.2.5. ROI Extraction

The detected hand landmarks of MediaPipe Hands have been used to find the borders of the palmprint. On the aligned image with detected landmarks, the boundaries of the extracted ROI have been determined by using the x and y pixel coordinates of landmarks 0, 5, and 17. While extracting the ROI, the farthest points, that provide an ROI of palmprint without any background, have been chosen horizontally and vertically. y coordinate of landmark 0 has been used as a lower limit on the y-axis, and the maximum of the y coordinate of landmarks 5 and 17 has been used as the upper limit on the y-axis. As a lower limit on the x-axis, the x coordinate of landmark 0 has been used, and lastly, as an upper limit on the x-axis, the x coordinate of landmark 17 has been used.

MediaPipe Hands framework tracks and detects the ROI automatically when a hand object is detected in the video stream at a certain distance from the camera. Despite varying illumination, the utilized hand-tracking framework enables the system to find key points to align hand images. Thus, the proposed system locates and extracts the ROI efficiently as shown in Figure 5.

Figure 5. A sample ROI image

4. Results and Discussion

All experiments have been carried out on Raspberry Pi 4 Model B with 4GB RAM and 64-bit quad-core processor. The proposed ROI extraction method has been implemented in Python 3.7 using Visual Studio Code IDE. The Python script has been used to build the system and MediaPipe Hands has been imported using OpenCV.

The performance of the proposed imaging system has been evaluated qualitatively rather than quantitatively. By using a dedicated thread, which is separate from the main thread, the frames have been read from the Raspberry Pi Camera. The frame-per-second (fps) rate of the camera sensor has been increased gradually. Thus, the most recent frame, which is read by the camera, has been grabbed at any moment in time. The performance of the proposed system has been evaluated on these grabbed images. Despite varying fps rates, MediaPipe Hands locates the palm and detects the reference points efficiently for each frame. As depicted in Figure 5 with a sample ROI image and in Figure 6 with detected reference points for flat and stretched hand positions under varying illumination, the proposed system can extract the palmprint ROI accurately. As a metric, the accuracy can be defined as the ratio between the number of perfectly extracted ROI and the total number of samples in the database. Correctly extracted ROI is an image that does not contain any background and only contains the palmprint. In these experiments, various scenarios have been used to test the efficiency of the proposed method such as hands with different poses and hands with accessories such as rings, hand tattoos, etc. Some of the sample images of these scenarios are given in Figure 6. However, the proposed method extracts ROIs dynamically even in these extreme cases. The delay interval between capturing sequential palmprint images is about 3 seconds. Since hand boundary detection or border tracing algorithms are not robust enough to ensure the stability of the proposed method due to complicated background noise, none of these algorithms have been used. The ROI segmentation accuracy could have been increased with additional preprocessing operations before the application of MediaPipe Hands or it could have been maximized with more proper parameter selection during the application of conventional methods. However, the main goal of this study is to show how well the MediaPipe Hands framework worked in detecting palmprint boundaries and extracting ROI from acquired videos. Our motivation is to develop a device without any physical sensor or guidance which restricts the user. The proposed ROI extraction method can be also used for palm vein and hand geometry biometrics since these biometric traits also focus on the same region that provides biometric features on the hand images.

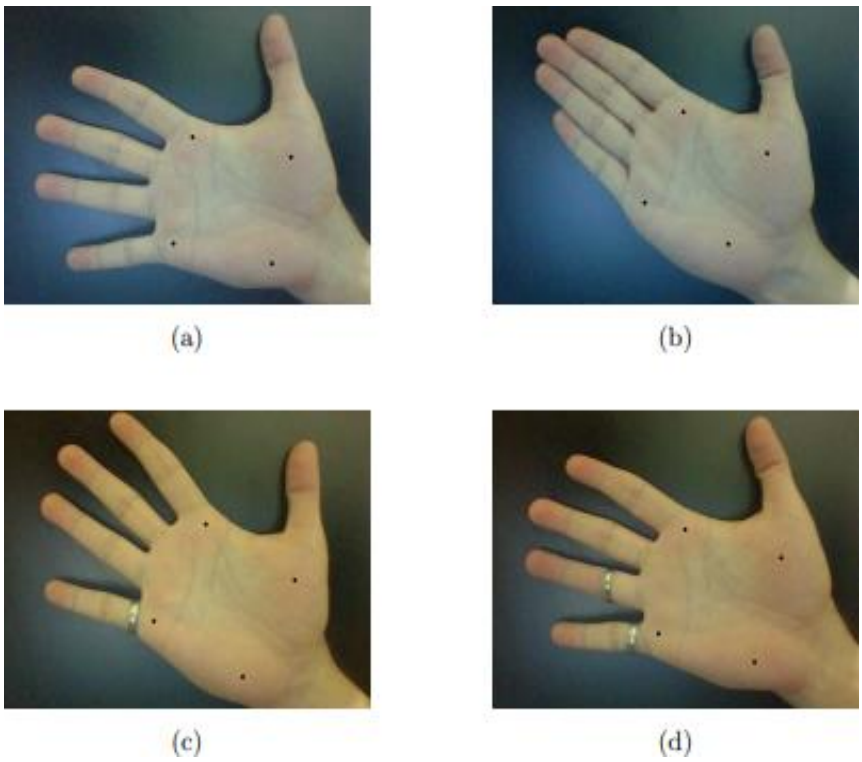

Figure 6. Image samples with detected hand landmarks (a) Stretched hand, (b) Flat hand, (c) Stretched hand with a ring, (d) Stretched hand with 2 rings

To increase the user's comfort, a contactless method has been proposed for image acquisition since the current trend in device design is towards an out-of-box structure. Although the contactless method causes translation and rotation problems, MediaPipe Hands and the proposed software resolve these problems efficiently. Thus, there will be no physical contact between the device surface and the user's hand during the image acquisition in the post-COVID-19 pandemic world. Moreover, the usage of MediaPipe Hands provides information about the hand on the platform. Whether the acquired image contains a right hand or a left hand, this information can be extracted with the help of this framework.

5. Conclusion

By their nature, recognition systems offer quick solutions, and they are used for security and privacy purposes in daily life. In this study, we have proposed to use MediaPipe Hands, which is a machine learning-based hand-tracking framework, to track hands on the imaging platform. Rather than analyzing the spatial domain and frequency domain, this study uses hand landmarks provided by this framework for ROI extraction. Since recognition performance does not solely depend on ROI localization but also on other factors such as applied feature extraction methods and used parameters, it has been only aimed to design an imaging system and extract ROIs of captured palmprint images. The developed imaging platform is effective, contactless, and hygienic. Its ROI extraction method is superior to conventional methods while finding palmprints in terms of time parameters. In future work, a large-scale palmprint database will be released with a sufficient number of users, samples, and sessions.

References

[1] Zhang, L., Li, L., Yang, A., Shen, Y., Yang, M. (2017). Towards contactless palmprint recognition: A novel device, a new benchmark, and a collaborative representation based identification approach. Pattern Recognition, 69, 199–212.

[2] Ong Michael, G. K., Connie, T., Jin Teoh, A. B. (2008). Touch-less palm print biometrics: Novel design and implementation. Image and Vision Computing, 26(12), 1551–1560.

[3] Zhang, D., Kong, W. K., You, J., Wong, M. (2003). Online palmprint identification. IEEE Transactions on Pattern Analysis and Machine Intelligence, 25(9), 1041–1050.

[4] Kekre, H. B., Sarode, T., Vig, R. (2012). An effectual method for extraction of ROI of palmprints. Proceedings - 2012 International Conference on Communication, Information and Computing Technology, ICCICT 2012, 12–16.

[5] Damak, W., Trabelsi, R. B., Damak, M. A., Sellami, D. (2018). Dynamic ROI extraction method for hand vein images. IET Computer Vision, 12(5), 586–595.

[6] Lu, H., Wang, Y., Gao, R., Zhao, C., Li, Y. (2021). A novel roi extraction method based on the characteristics of the original finger vein image. Sensors, 21(13).

[7] Yang, L., Yang, G., Zhou, L., Yin, Y. (2015). Superpixel based finger vein ROI extraction with sensor interoperability. Proceedings of 2015 International Conference on Biometrics, ICB 2015, 444–451.

[8] Li, W. X., Xia, S. X., Zhang, D. P., & Zhuo-Qun, X. U. (2004). A new palmprint identification method using bi-directional matching based on major line features. Journal of computer research and development, 41(6), 996-1002.

[9] Poon, C., Wong, D. C. M., Shen, H. C. (2004). A new method in locating and segmenting palmprint into region-of-interest. Proceedings - International Conference on Pattern Recognition, 4, 533–536.

[10] Wang, L., Leedham, G., Siu-Yeung Cho, D. (2008). Minutiae feature analysis for infrared hand vein pattern biometrics. Pattern Recognition, 41(3), 920–929.

[11] Lin, S., Xu, T., Yin, X. (2017). Region of interest extraction for palmprint and palm vein recognition. Proceedings - 2016 9th International Congress on Image and Signal Processing, BioMedical Engineering and Informatics, CISP-BMEI 2016, (4), 538–542.

[12] Jaswal, G., Kaul, A., Nath, R. (2017). Palm print ROI extraction using Bresenham line algorithm. 4th IEEE International Conference on Signal Processing, Computing and Control, ISPCC 2017, 2017-Janua, 547–552.

[13] Yan, M., Sun, D., Zhao, S., & Zhou, J. (2013, November). A robust approach for palm ROI extraction based on real-time region learning. In Chinese Conference on Biometric Recognition (pp. 241-248). Springer, Cham.

[14] Kocakulak, M., & Acir, N. (2022, May). Dynamic ROI Extraction for Palmprints using MediaPipe Hands. In 2022 30th Signal Processing and Communications Applications Conference (SIU) (pp. 1-4). IEEE.

[15] Zhang, F., Bazarevsky, V., Vakunov, A., Tkachenka, A., Sung, G., Chang, C.-L., & Grundmann, M. (2020). MediaPipe Hands: On-device Real-time Hand Tracking. http://arxiv.org/abs/2006.10214

[16] Sun, Z., Tan, T., Wang, Y., Li, S. Z. (2005). Ordinal palmprint represention for personal identification. Proceedings - 2005 IEEE Computer Society Conference on Computer Vision and Pattern Recognition, CVPR 2005, I, 279–284.

[17] Hao, Y., Sun, Z., Tan, T., & Ren, C. (2008, October). Multispectral palm image fusion for accurate contact-free palmprint recognition. In 2008 15th IEEE International Conference on Image Processing (pp. 281-284). IEEE.

[18] Kumar, A. (2019). Toward More Accurate Matching of Contactless Palmprint Images under Less Constrained Environments. IEEE Transactions on Information Forensics and Security, 14(1), 34–47.

[19] Kumar, A. (2008). Incorporating cohort information for reliable palmprint authentication. Proceedings - 6th Indian Conference on Computer Vision, Graphics and Image Processing, ICVGIP 2008, 583–590.

[20] Dai, J., Feng, J., Zhou, J. (2012). Robust and efficient ridge-based palmprint matching. IEEE Transactions on Pattern Analysis and Machine Intelligence, 34(8), 1618–1632.

[21] Chen, W. S., Chiang, Y. S., Chiu, Y. H. (2007). Biometric verification by fusing hand geometry and palmprint. Proceedings - 3rd International Conference on Intelligent Information Hiding and Multimedia Signal Processing, IIHMSP 2007., 2, 403–406.

[22] Poinsot, A., Yang, F., Paindavoine, M. (2009). Small sample biometric recognition based on palmprint and face fusion. 4th International Multi-Conference on Computing in the Global Information Technology, ICCGI 2009, 118–122.

[23] Michael, G. K. O., Connie, T., Teoh Beng Jin, A. (2010). An innovative contactless palm print and knuckle print recognition system. Pattern Recognition Letters, 31(12), 1708–1719.

[24] Ferrer, M. A., Vargas, F., Morales, A. (2011). BiSpectral contactless hand based biometric system. 2011 2nd National Conference on Telecommunications, CONATEL 2011 - Proceedings.

[25] Morales, A., Ferrer, M. A., Travieso, C. M., Alonso, J. B. (2012). Multisampling approach applied to contactless hand biometrics. Proceedings - International Carnahan Conference on Security Technology, 224–229.

[26] Aykut, M., Ekinci, M. 2015. Developing a contactless palmprint authentication system by introducing a novel ROI extraction method. Image and Vision Computing, 40, 65–74.

[27] Xiao, Q., Lu, J., Jia, W., & Liu, X. (2019). Extracting palmprint ROI from whole hand image using straight line clusters. IEEE Access, 7, 74327-74339.

[28] Liang, X., Li, Z., Fan, D., Li, J., Jia, W., & Zhang, D. (2022). Touchless palmprint recognition based on 3D Gabor template and block feature refinement. Knowledge-Based Systems, 249, 108855.

[29] Lugaresi, C., Tang, J., Nash, H., McClanahan, C., Uboweja, E., Hays, M., Zhang, F., Chang, C.-L., Yong, M. G., Lee, J., Chang, W.-T., Hua, W., Georg, M., & Grundmann, M. (2019). MediaPipe: A Framework for Building Perception Pipelines. http://arxiv.org/abs/1906.08172

[30] Yakno, M., Mohamad-Saleh, J., and Rosdi, B. A. (2015, May). New technique for larger ROI extraction of hand vein images. In 2015 International Conference on BioSignal Analysis, Processing and Systems (ICBAPS) (pp. 82-87). IEEE.

J Inno Sci Eng,2023, 7(1):40-47
https://doi.org/10.38088/jise.1134816

Research Article

Prediction of Cancer in DNA Sequences Using Unsupervised Learning Methods

Seyma Dogru [1*], Volkan Altuntas[2]

[1*,2] *Department of Computer Engineering, Bursa Technical University, 16310 Bursa, Turkey*

Abstract

Today, with the development of technology, the decision-making capabilities of machines have also increased. With their high analytical skills, computers can easily catch points and relationships that may escape the human eye.

Thanks to these capabilities, machines are also widely used in the field of health. For example, many machine-learning techniques developed on cancer prediction have been successfully applied. Early detection of cancer is crucial to survival. In the early diagnosis of cancer, the rates of drug treatment, chemotherapy, or radiotherapy that the person will be exposed to are significantly reduced and the patient gets through this process with the least amount of wear and tear. Gene Expression Cancer RNA-Seq Dataset was used in this study. This data set includes gene expression values of 5 cancer types (BRCA, KIRC, LUAD, LUSC, UCEC). DNA sequences in the dataset were analyzed using k-means and hierarchical clustering algorithms, which are unsupervised machine learning methods. The aim of the study is to develop a usable machine-learning model for the early detection of cancer at the gene level. Adjusted Rand Index (ARI), Silhouette Score, and Accuracy Metrics were used to evaluate the analysis results. The rand index calculates the similarity between clusters by counting the binaries assigned to clusters. The adjusted Rand Index is a randomly adjusted version of the Rand Index. The silhouette score indicates how well a data point fits within its own set among separated datasets. The accuracy metric is obtained as a percentage of correctly clustered data points divided by all predictions. Different connection methods are used in the hierarchical clustering algorithm. These are 'complete', 'ward', 'average', and 'single'. As a result of the study, the accuracy in the k-means algorithm was 0.990, the Adjusted Rand Index was 0.79, and the Silhouette Score was 0.14. Looking at the hierarchical clustering, ward performed the best of the four linkage methods, with an ARI score of 0.76 and a silhouette score of 0.13. As a result of the study, the accuracy of the hierarchical clustering algorithm was 0.999.

Keywords: k-Means, Machine Learning, Unsupervised Learning, Cancer, DNA, Hierarchical Clustering.

Cite this paper as:
Dogru, S. and Altuntas, V. (2023). *Prediction of Cancer in DNA Sequences Using Unsupervised Learning Methods*. Journal of Innovative Science and Engineering.7(1):40-47

*Corresponding author: Seyma Dogru
E-mail: seymadogru37@gmail.com

Received Date:05/07/2022
Accepted Date:17/10/2022

1. Introduction

Cancer is a disease in which certain cells in the body grow uncontrollably and spread to other parts of the body. Cancer can start almost anywhere in the human body, which is made up of trillions of cells. In a healthy human body, cells grow and then multiply to form new cells. They also die when they take damage or get old. Instead, the body produces new cells. In some bodies, this order can be disrupted, and damaged cells grow and multiply abnormally when they shouldn't. As a result, this disease, which we call cancer, occurs. As in all diseases, early diagnosis of cancer is very important to save the life of the patient. Many studies have been conducted over the years to facilitate diagnosis. Cancer can be diagnosed at the gene level and with imaging techniques. Cancers are heterogeneous due to their habitat. Subtypes of cancer types can also be found. For example, there are 5 subtypes of cancer for breast cancer. It has been named Luminal A, Luminal B, HER2 overexpressed, Basal-like, and Claudin-low [1]. In this study, the diagnosis of cancer subtypes by DNA sequencing was investigated. Each subtype has a unique treatment plan, and in this respect, a successful diagnosis of the subtype is important for the patient to receive the right treatment. In previous studies, supervised learning algorithms of machine learning method (Naive Bayes, Decision Tree, Random Forest, Support Decision Machine, K Nearest Neighbor) were used. There are also studies using the Hierarchical Clustering Algorithm [2, 3]. The hierarchical clustering algorithm was chosen by the researchers because of the inherent complexity of most other algorithms and the difficulty of determining the parameters that need to be determined when applying. In this study, k-Means and Hierarchical Clustering algorithms, which are unsupervised machine learning algorithms, were successfully applied and it was observed how they performed on unlabeled data. In the k-Means algorithm, the regions where the data points are concentrated are taken as the center. Data points around these centers are included in the clusters using the Euclidean distance. On the other hand, hierarchical clustering was made, and clustering was done with four linking methods. Single, ward, complete and average were used, and their results were compared. It has been shown that both algorithms give successful results in cancer detection at the gene level. 99.0% accuracy in the k-Means algorithm and 99.9% accuracy in the hierarchical clustering algorithm was obtained.

2. Literature Review

In the study conducted by Fahad Hussain and his colleagues in 2019, cancer prediction was made on the “Gene expression cancer RNA-Seq Data Set” dataset using Naive Bayes, Decision Tree, Random Forest, Support Decision Machine, K Nearest Neighbour algorithms [4]. Elaheh Moradi and colleagues conducted a study titled "Machine learning framework for early MRI-based Alzheimer's transformation prediction in MCI subjects." They used MRI images to identify Alzheimer's disease 1-3 years before clinical diagnosis. For this purpose, semi-supervised and supervised machine learning algorithms were used. [5]. In the study of Konstantina Kourou and her colleagues in 2015, various machine learning and data mining methods were applied to solve the diagnosis problem of cancer patients. The authors conducted a qualitative survey of research articles over the past five years and identified several studies such as cancer susceptibility, cancer recurrence, and cancer survival [6]. In the study conducted by Gunasekaran Manogaran and his colleagues in 2018, Bayes Markov Model and Gaussian Clustering were used to model DNA copy number variation across the genome and identification of cancer [7]. In the study conducted by Zeid Khitan and his colleagues in 2017, algorithms such as SVM, Decision Tree, Neural Network, Random Forest, Linear Model were used to predict the outcome of dialysis, death, or creatinine elevation in kidney patients due to diet [8]. In the study conducted by Manish

Motwani and his colleagues in 2017, they used machine learning algorithms to analyze the mortality within 5 years in patients who underwent angiography [9]. A lung cancer prediction model was developed by Timor Kadir and Fergus Gleeson in 2018 using machine learning and imaging techniques [10]. In 2020, Milon Islam and his colleagues created a prediction model on breast cancer using machine learning techniques. They achieved an accuracy of over 98% in ANN, while they achieved an accuracy of 97.14% in SVM [11]. In the study by Yixuan Li and Zixuan Chen in 2018, different machine learning methods on breast cancer (Decision Tree (DT), Random Forest (RF), Support Vector Machine (SVM), Neural Network (NN), and Logistic Regression (LR)) have been tested and their performances compared. Accuracy was 0.961, 0.951, 0.961, 0.937, and 0.956 for DT, SVM, RF, RF, LR, and NN, respectively [12]. In the study "Using machine learning to predict ovarian cancer" by Mingyang Lu et al., ovarian cancer prediction was made using algorithms such as Decision tree and Logistic regression [13].

3. Method

In this article, the k-Means algorithm, a machine learning algorithm, and a hierarchical clustering algorithm were used to analyze the DNA sequences of cancer patients. The K-Means algorithm is one of the most popular unsupervised machine learning algorithms. Unsupervised machine learning algorithms work based on clustering.

3.1. Data Set

DNA data of cancer patients were obtained through the data set named “Gene expression cancer RNA-Seq Data Set” [14]. This data set contains 20531 features and 801 rows of data. These classes represent the gene sequence for patients with five types of tumors. Dataset was used in this study. This data set includes gene expression values of 5 cancer types (BRCA, KIRC, LUAD, LUSC, UCEC). Cancer, designated BRCA, is the most aggressive type of breast cancer seen in women. KIRC is a type of kidney cancer known for its high mortality rate worldwide. An average of 75 percent of kidney cancers are diagnosed with this type of cancer. LUAD cancer, which accounts for 40 percent of lung cancer diagnoses, is known to spread more slowly than other types of lung cancer. It is also seen in non-smokers. LUSC, the second most common form of lung cancer, is the most common type of cancer among smokers. Their location is usually in the middle of the lung. UCEC is a type of cancer encountered before birth.
The mortality rate is very high due to the difficulty of early diagnosis. It is known as the most common cancer in women [15].

3.2. K-Means

The clustering technique is only one of the most preferred data analysis methods to obtain information about the classes of data. It can be defined as the task of identifying subgroups so that the data in the same cluster are very similar, while the data in different clusters are very different. Based on a similarity measure, such as Euclidean distance or correlation-based distance, an attempt is made to find homogeneous subgroups within the data so that the data points in each cluster are as similar as possible. The decision of which similarity measurement method to use is application specific [16]. Typically, unsupervised algorithms arrive at a conclusion from datasets using only input vectors, without reference to known or labeled results [17]. It aims to put data showing similar characteristics in the same cluster. There is no clustered data. Data that does not belong to any cluster is included in the Outlier cluster.

K-means, a clustering algorithm, determines subsets of unlabeled data points. The k parameter requested from the user specifies how many subsets it should be divided into. The algorithm decides which dataset will be in which cluster, taking into account the similarity of the data points, without the need for prior training. When the algorithm starts working, it assigns centroids as many as the number of clusters we have determined, so it works on a centroid basis.
The algorithm in question tries to minimize the sum of the differences between the data and the clusters in which they are located. It takes unlabeled points as input data and splits them into k clusters. Iterations continue until the best separation is found.

There are some metrics to measure the success of the study. These are adjusted rand score (ARI), silhouette score, and accuracy. In the ARI score, "0" indicates random labeling, and "1" indicates a perfect replica of the truth. If the silhouette is in the score value, the values are interpreted as -1 for very bad clusters and +1 for very dense clusters.
The Accuracy formula for k-Means is calculated using true positive (TP), true negative (TN), false positive (FP), and false negative (FN) metrics as follows.

$$\text{Accuracy} = (TP + TN) / (TP + TN + FP + FN) \quad (1)$$

3.3. Hierarchical Clustering

The hierarchical clustering method was also used in the study. Hierarchical Clustering was developed to eliminate a disadvantage in the k-Means algorithm. In the k-Means algorithm, the number of clusters must be specified beforehand. For this reason, hierarchical clustering has emerged. The basic logic of the hierarchical clustering algorithm is based on the combination of similar features or vice versa. There are two basic approach logics; agglomerative and divisive. In Agglomerative logic, first of all, all data is separate from each other, so all data is considered as a set on its own. Then, by looking at the characteristics of each, data with similar attributes are started to be thrown into the same cluster. In the Divisive method, the opposite of this process is performed. First of all, all the data is looked at as if it were a cluster and it is started to be divided into subsets according to their distance or similarity. As a result of this process, each data becomes a cluster on its own.
Different linkage methods are used while performing these operations. Linkage methods are Single Linkage, Complete Linkage, Average Linkage, Ward's Linkage, Median Linkage, and Centroid Linkage. Among these, Single Linkage, Complete Linkage, and Average Linkage methods are link-based techniques. Ward's Linkage method is variance based. Median Linkage and Centroid Linkage are based on centralization. Single Linkage proceeds by merging the two closest clusters using the distance matrix. However, this method takes some time. In the Complete Linkage method, the merge process is performed by considering the largest distance between the data. The downside is that this method is sensitive to endpoints. The basic logic in the Average Linkage method is the process of applying merging by averaging the distances between the data. This method is more preferred. Ward's Linkage method aimed to minimize information loss. Information loss is the sum of the squares of the errors. This method does not combine groups with the smallest distance but does combine structures with the minimum value of variance. The Centroid Linkage method performs a grouping based on Euclidean distance. It is sufficient that the center points of the converging clusters are at a minimum distance from each other while performing the operation. In the Median Linkage method, the center of gravity of the larger data set is taken as the basis when merging the clusters, and the new center is closer to this center of gravity [18]. In the

hierarchical clustering method, we can visualize with a dendrogram. A dendrogram is a tree-like structure describing the relationship between all data points in the system [19].

3.4. Model Building and Accuracy Measurement

While measuring the accuracy of the model, TP, FP, TN, and FN values were used. TP is the positive data, and the model says positive; FP is the negative data, but the model calls it positive; TN is the negative data, and the model calls it negative; FN represents data that is positive but predicted negatively by the model. These values were reached by comparing the outputs predicted by the model with the actual labels.

4. Results and Discussion

After the cleaning and editing studies on the data set, k-Means and Hierarchical clustering algorithms were applied. The test size was determined at a rate of 0.5 to be the same in the algorithms. Since there are 5 cancer types, the number of clusters was chosen as 5. After the necessary coding was done, the ARI score was 0.79 and the silhouette score was 0.135 in the k-Means algorithm (Table 1). The ARI score appears to be closer to the case of perfect duplication of values. Looking at the silhouette score, it is seen that the value is close to the average. Four linkage methods (full, ward, average, single) were tried in the hierarchical clustering algorithm and the best results were obtained in ward with ARI score and silhouette score of 0.775 and 0.13, respectively (Table 2). The reason why the silhouette score is low is that the ward method differentiates the classes from each other well. Looking at the Accuracy value, it was seen that accuracy was 0.990 for k-Means and 0.999 for Hierarchical clustering, slightly better accuracy than the k-Means algorithm (Table 3).

Table 1. ARI and Silhouette Score Results for k-Means

Adjusted Rand Score	0.7940732386133297
Silhouette Score	0.13507290311138614

Table 2. ARI and Silhouette Score Results for Hierarchical Clustering

	ARI	Silhoutte Score
complete	-0.030075	0.091312
ward	0.775358	0.133002
average	0.00041	0.254240
single	0.00041	0.201673

Table 3. Accuracy for k-Means and Hierarchical Clustering

	Accuracy
k-Means	0.9909194430904822
Hierarchical Clustering	0.9997240156180038

Then the dendrogram was drawn. The dendrogram obtained is as in Figure 1.

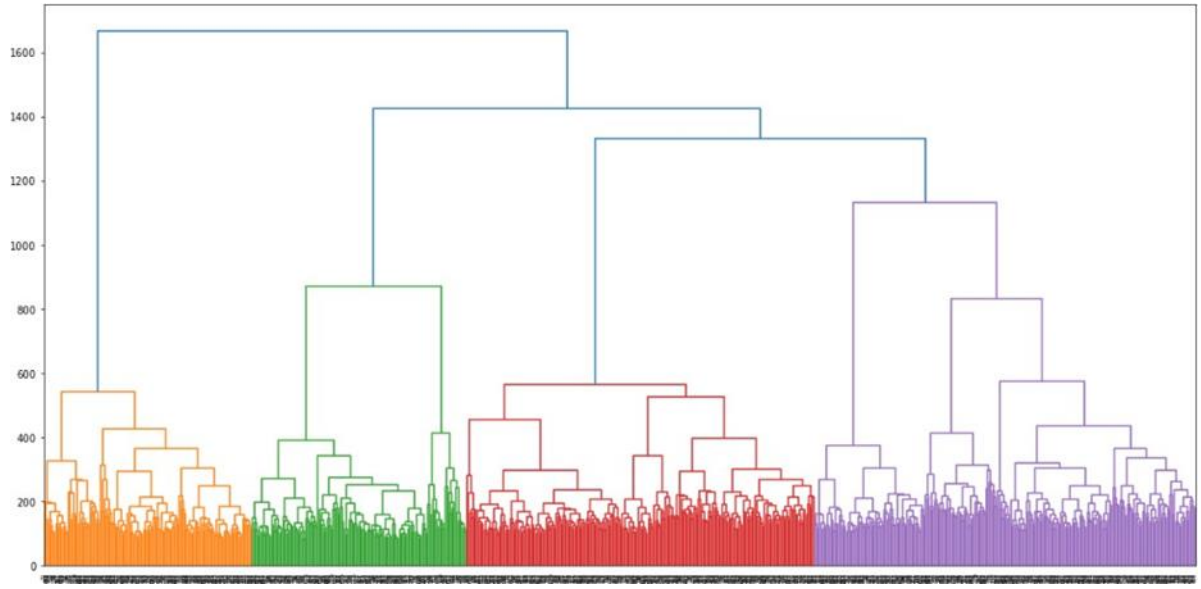

Figure 1. Dendrogram

In this study, two successful models with 99.0% and 99.9% accuracy values for cancer subtype prediction are presented. Since the algorithms are not deterministic algorithms, results can be obtained at once without the need to run the algorithm repeatedly. Considering the results, it is seen that this study is a reliable study that can be used for cancer prediction. Thanks to this study, it will be possible to determine whether a person has cancer yet at the gene level and to be diagnosed early. The patient will be able to get through this period with minimal wear, without the need for more drugs, chemotherapy, or radiotherapy. Thus, psychological, economic, and physical damage will be minimized. This study can be an informative resource for software that will be developed in the medical field and include data mining algorithms, and with this study, the contribution of clustering algorithms to the evaluation and analysis of various medical data can be observed. Compared with previous studies [20], this study showed a higher accuracy rate. It is seen that none of the algorithms used here reach 99% accuracy. The source codes of the study can be found at [21].

5. Conclusion

In this study, the performance of two different unsupervised machine learning methods was investigated on the data set containing the gene expression values of 5 cancer types (BRCA, KIRC, LUAD, LUSC, UCEC). K-Means and Hierarchical Clustering algorithms were used as clustering algorithms. The study was carried out on the Jupyter Notebook platform. Accuracy, adjusted rand score (ARI) and silhouette score metrics were used to measure the performance of the algorithms used. Values close to 1 for the ARI score indicate good clustering. Silhouette score values are -1 for very weak clusters, 1 for very dense clusters, and 0 for results where the clusters are well separated from each other. The study was visualized by drawing a dendrogram (Figure 1). K-Means and Hierarchical Clustering algorithms showed similar clustering performance. While the K-Means algorithm has an accuracy value of 99.09%, the Hierarchical Clustering algorithm has an accuracy value of 99.9%. Although both methods are successful, the Hierarchical Clustering algorithm has slightly higher accuracy. 4 different connection methods are used in the Hierarchical Clustering algorithm. These connection methods are complete, ward, average, and single. When the results were compared as in Table 2, it was seen that the "ward" method showed the best performance. The ARI score is 0.775 and the Silhouette score is 0.13. When these results are interpreted, the ARI score is close to 1. This result indicates a good clustering. Looking at the

silhouette score, it is close to 0. This result shows that the clusters are well separated from each other. When the results of the K-Means algorithm are examined, it is seen that the ARI score is 0.79 and the silhouette score is 0.135. It also states that the k-Means algorithm creates successful clusters as in hierarchical clustering. Both clustering techniques used in this study showed successful results. Two models have been obtained that can be used for the early detection of cancer at the gene level. This study will shed light on future studies on the subject.

6. Acknowledgments

The authors are grateful to TUBITAK ULAKBIM High Performance and Grid Computing Center (TRUBA), Bursa Technical University High-Performance Computing Laboratory.

References

[1] Prat A, Pineda E,Adamo B, Galván P, Fernández A, Gaba L, et al. Clinical implications of the intrinsic molecular subtypes of breast cancer. Breast, 2015

[2] M.C. de Souto, I.G. Costa, D.S. de Araujo, T.B. Ludermir, A. Schliep, Clustering cancer gene expression data: a comparative study, BMC Bioinforma. 9 (1) (2008) 497, https://doi.org/10.1186/1471-2105-9-497

[3] S. Saha, A. Ekbal, K. Gupta, S. Bandyopadhyay, Gene expression data clustering using a multiobjective symmetry based clustering technique, Comput. Biol. Med. 43 (11) (2013) 1965–1977, https://doi.org/10.1016/j.compbiomed.2013.07.021

[4] Fahad Hussain, Umair Saeed, Ghulam Muhammad, Noman Islam and Ghazala Shafi Sheikh, "Classifying cancer patients based on DNA sequences using machine learning", 2019

[5] Elaheh Moradi, Antonietta Pepe, Christian Gaser, Heikki Huttunen, Jussi Tohka, "Machine learning framework for early MRI-based Alzheimer's conversion prediction in MCI subjects", 2014

[6] KonstantinaKourou, Themis P.Exarchos, Konstantinos P. Exarchos, Michalis V. Karamouzis, Dimitrios I. Fotiadisa, "Machine learning applications in cancer prognosis and prediction", Computational and Structural Biotechnology Journal, 2015

[7] Gunasekaran Manogaran, V. Vijayakumar R. Varatharajan, Priyan Malarvizhi Kumar, Revathi Sundarasekar, Ching-Hsien Hsu, "Machine Learning Based Big Data Processing Framework for Cancer Diagnosis Using Hidden Markov Model and GM Clustering", Wireless Personal Communications, 2018

[8] Zeid Khitan, Anna P. Shapiro, Preeya T. Shah, Juan R. Sanabria, Prasanna Santhanam, Komal Sodhi, Nader G. Abraham, and Joseph I. Shapiro, "Predicting Adverse Outcomes in Chronic Kidney Disease Using Machine Learning Methods: Data from the Modification of Diet in Renal Disease", Marshall Journal of Medicine, 2017

[9] Manish Motwani, Damini Dey, Daniel S. Berman, Guido Germano, Stephan Achenbach et al., "Machine learning for prediction of all-cause mortality in patients with suspected coronary artery disease: a 5- year multicentre prospective registry analysis", European Heart Journal, 2017

[10] Timor Kadir, Fergus Gleeson, "Lung cancer prediction using machine learning and advanced imaging Techniques", 2018

[11] Md. Milon Islam, Md. Rezwanul Haque, Hasib Iqbal, Md. Munirul Hasan, Mahmudul Hasan, Muhammad Nomani Kabir, “Breast Cancer Prediction: A Comparative Study Using Machine Learning Techniques”, 2020

[12] Yixuan Li, Zixuan Chen, “Performance Evaluation of Machine Learning Methods for Breast Cancer Prediction”, 2018

[13] Mingyang Lu, Zhenjiang Fand, Bin Xu, Lujun Chen, Xiao Zheng, Jundong Li, Taieb Znati, Qi Mi, Jingting Jiang, “Using machine learning to predict ovarian cancer”, 2020

[14] UCI Machine Learning Repository, “Gene Expression Cancer RNA-Seq Data Set”, 2016, <https://archive.ics.uci.edu/ml/datasets/gene+expression+cancer+RNA-Seq>, (24 May 2022)

[15] Laiqa Rukhsar , Waqas Haider Bangyal , Muhammad Sadiq Ali Khan , Ag Asri Ag Ibrahim, Kashif Nisar and Danda B. Rawat, “Analyzing RNA-Seq Gene Expression Data Using Deep Learning Approaches for Cancer Classification”, 2021

[16] Imad Dabbura, "K-Means Clustering: Algorithm, Applications, Evaluation Methods, and Drawbacks" 2018, <https://towardsdatascience.com/k-means-clustering-algorithm-applications-evaluation-methods-and-drawbacks- aa03e644b48a>, (01 June 2022)

[17] Dr. Michael J. Garbade, "Understanding K-Means Clustering in Machine Learning" 2018, <https://towardsdatascience.com/understanding-k-means-clustering-in-machine-learning-6a6e67336aa1>, (01 June 2022)

[18] Eyup Kaan Ulgen, “Hierarchical Clustering”, 2021, <https://www.veribilimiokulu.com/hiyerarsik-kumeleme/>, (15 June 2022)

[19] Prasad Pai, Hierarchical Clustering Explained, 2021, <https://towardsdatascience.com/hierarchical-clustering-explained-e59b13846da8>, (10 June 2022)

[20] Fahad Hussain, Umair Saeed, Ghulam Muhammad, Noman Islam and Ghazala Shafi Sheikh, “Classifying cancer patients based on DNA sequences using machine learning”, 2019

[21] Seyma Dogru, “Predicting Cancer Using Machine Learning on DNA Sequences”, 2022, <https://github.com/seymadogru/Prediction-of-Cancer-in-DNA-Sequences-Using-Unsupervised-Learning-Methods-.git >, (03 September 2022)

J Inno Sci Eng,2022, 7(1):48-59
http://doi.org/10.38088/jise.1174927

Research Article

Effect of Permeability-Reducing Admixtures on Concrete Properties at Different Cement Dosages

Musa Yildirim [1*], Hacer Bilir Ozhan[2]

[1*,2] *Department of Civil Engineering, Bursa Technical University, 16320, Bursa, Turkey*

Abstract

Concrete is the most common building material used worldwide. Significantly high strength values have been achieved owing to developing material technology. Besides compressive strength, durability properties should also be taken into consideration since concrete is exposed to several external effects throughout its service life. Durability properties are mainly associated with the voids in the internal structure and surface of the concrete. Even if not exposed to any external effects, concrete contains several pores and micro-cracks. These pores and cracks enlarge with the influence of external effects, and new cracks are developed. Therefore, various methods are used to prevent the permeability of harmful liquids and gases into concrete structures. This study used permeability-reducing admixtures (PRAs) and polycarboxylate-based superplasticizers of various cement dosages to produce concrete mixtures. The main purpose is to examine the interaction of these admixtures with the cement dosage. Workability, compressive strength, and depth of water penetration under pressure tests were conducted to observe the effect of PRA on these parameters. The admixture crystallized in the internal structure of the concrete and created a fuller volume. While the compressive strength increased as a result of the crystallized product, the depth of water penetration decreased. Slump tests revealed that the admixture was compatible with all cement dosages, and it did not significantly affect the workability properties of the concrete. Expectedly, the compressive strength increased as the cement dosage increased, while the positive effect of the PRA gradually decreased. The PRA admixture also contributed to the decrease in the depth of water penetration, but its impact decreased as the cement dosage increased. It was concluded based on present findings that the PRA admixture, which is the most effective at the lowest cement dosage, increased the compressive strength values by 9.44% at this dosage and decreased the depth of water penetration under pressure by 26.09%.

Keywords: Permeability-reducing admixture, Cement dosage, Depth of water penetration, PRA.

Cite this paper as:
Yildirim, M. and Bilir Ozhan, H. (2023). *Effect of Permeability-Reducing Admixtures on Concrete Properties at Different Cement Dosages*. Journal of Innovative Science and Engineering.7(1):48-59

*Corresponding author: Musa Yildirim
E-mail: yildirim280@gmail.com

Received Date:14/09/2022
Accepted Date:27/10/2022

1. Introduction

Concrete has high compressive strength and mechanical properties owing to developing material technology and new construction methods. However, preserving such properties is a highly complex process since concrete is exposed to several external effects throughout its service life. Concrete is a semi-brittle material that includes many gaps and cracks in its microstructure, especially between the cement matrix and aggregates, even if there is no external effect [1]. Gases, liquids, and ions leak into the concrete structure from existing cracks and voids, and they negatively affect the durability of concrete. Although the compressive strength and durability properties of concrete are generally positively correlated with each other, the durability properties should also be improved since the material is constantly exposed to external influences [2,3]. Permeability properties are of great importance for concrete to be resistant to external influences. Harmful chemicals pass through the cracks and gaps in the structure of concrete and cause various physical and chemical reactions, thereby disrupting the structure of concrete. These deteriorations directly affect the durability properties of concrete [4]. Fluid can enter concrete cavities in three different ways: permeability caused by hydrostatic difference; capillary conduction caused by water surface tension; and diffusion caused by the vapor pressure difference of liquid vapors [5]. The major factor that causes these three different transmissibility is the gaps and micro-cracks in the concrete structure.

Although permeability is associated with a low void ratio, various parameters, such as material ratios, curing conditions, etc., affect the durability and permeability properties of the materials [6,7]. Different methods and materials are used to reduce permeability. Mineral admixtures are commonly used in concrete mixtures to improve durability properties as well as strength properties. In concrete, admixtures bind Ca $(OH)_2$, which is easily soluble in water, and convert it into C-S-H gel. In this way, they block the gaps that the lime will cause by dissolving. In addition, most of the mineral additives create a fuller concrete volume by filling the voids in the interfacial transition zones (ITZ) between aggregates and cement paste, especially since the silica fume is a hundred times smaller than the average diameter of the cement. Thus, a more impermeable concrete design is possible with mineral additives [8,9]. It was observed that blast furnace slag reduced permeability-related properties such as chloride-ion permeability, diffusion coefficients, and corrosion [10]. Higher and more advanced structures are being built with developing construction technologies to meet the dwelling needs of increasing populations. Concrete strength classes have also increased, and difficult-to-pour concrete recipes have been created. With the development of plasticizer chemical admixtures, workability problems have been largely solved today. Permeability-reducing admixtures (PRAs) have been developed for construction that has to be built even in unfavorable conditions. The American Concrete Institute classifies PRAs into 5 different categories [11]. These are hydrophobic water repellents, polymer products, finely divided solids, hydrophobic pore blockers, and crystalline products. However, methods such as the closure of gaps with bacteria and the use of polymers in capsules, which have become more common after the publication of this report, are available even though they are not included in the classification. By closing the gaps inside and on the surface of the concrete, these methods produce more impermeable and highly durable concrete [12-14]. The admixture to be used under hydrostatic conditions for the samples to be tested for depth of penetration of water under pressure is mentioned as crystalline hydrophilic polymers (latex, water-soluble or liquid polymer). Admixtures with hydrophobic pore blockers push liquids into the concrete, allowing for less liquid to be found. However, they cannot block the liquid under any hydrostatic pressure and thus lose their working mechanism. However, the crystallized permeability-reducing admixture used in this study does not lose its mechanism

of action under hydrostatic pressure. These admixtures, which are resistant to hydrostatic pressure, form crystallized structures with the ingress of water into the concrete, creating a more repellent structure [13]. The reaction of cement with calcium silicate and crystallized promoter is given in Eq 1. This reaction produces a modified calcium silicate hydrate and a pore-blocking precipitate. Furthermore, as illustrated in Figure 2, a product of cement hydration can react with Ca(OH)2 to form a C-S-H gel [15].

$$3CaO\text{-}SiO_2 + M_xR_x + H_2O \rightarrow Ca_xSi_xO_xR\text{-}(H_2O)_x + M_xCaR_x\text{-}(H_2O)_x \quad (1)$$

$$Ca(OH)_2 + \text{Silicate} \rightarrow \text{C-S-H} \quad (2)$$

PRAs reduce permeability through the closing of the gaps with resultant products. However, the formation of extra C-S-H gel seen in the reactions does not always mean that the compressive strengths will also increase. When using this type of permeability-reducing admixtıre, the chemical admixture quantity should be so selected as to reduce the effects on compressive strength. In some cases, additives may cause a loss of strength [16].

In previous studies, the use of such crystallized admixtures has been shown to improve various concrete properties. It has increased the compressive strength, water absorption, permeability, flexure strength, and durability properties by filling the voids in the concrete structure with crystallized formations [17–20]. However, the effect of PRA also depends on various variables, such as water/cement ratio and cement type [21]. Hassani et al. [19] concluded that the effectiveness of the admixture depended on binder type and that reported changing effectiveness values with increasing water/cement ratios. It was also observed that blast furnace slag had a positive effect on permeability properties. Khatib et al. [22] reported that metakaolin significantly reduced concrete permeability. There are studies also on the ratio of the admixture to be used [23].

The compatibility of the admixtures with different materials and different water/cement ratios was investigated under different conditions in previous studies. However, it has not been investigated how it will affect concrete mixtures containing cement at different dosages when there is a constant mineral admixture and water/cement ratio. Therefore, concrete mixtures containing blast furnace slag, which is a commonly used mineral additive, and cement in 3 different dosages were produced in this study. While the constant water/cement ratio and mineral additive dosage were used in the mixtures, only the cement dosage was changed. By adding permeability-reducing admixture (PRA) to each of these mixtures, a total of 6 types of concrete, with and without admixtures, were produced. Slump values, 7 and 28-day compressive strengths, and water penetration depth under pressure of the produced concrete were determined. Thus, the cement dosage-dependent effects of admixtures on workability, strength, and durability properties were investigated.

2. Materials and Methods

2.1. Materials

2.1.1. Binding materials

In this study, CEMI 42.5R type Portland cement was used in accordance with TS EN 197-1 standard [24]. All mixtures contained the same amount of blast furnace slag (BFS). Table 1 presents the chemical components of BFS and cement. The specific gravities of cement and BFS are 3.10 and 2.86, respectively.

Table 1. The chemical composition of cement and BFS (%, by weight).

Chemical compound	SiO_2	CaO	Al_2O_3	MgO	Fe_2O_3	K_2O	Na_2O	SO_3	Loss on ignition
Cement	20.12	62.38	5.88	1.87	2.40	0.93	0.38	3.28	1.82
BFS	40.20	35.90	11.66	5.88	1.68	1.47	0.30	0.90	0.88

The appearance of BFS and cement, the binding materials used in this study, is represented in Figure 1.

Figure 1. The appearance of BFS (left) and cement (right).

2.1.2. Aggregate

Three types of aggregates, 0–5 mm, 5–15 mm, and 15–22 mm crushed stone aggregates, were used in this study. The specific gravity values of these aggregates are 2.67, 2.70, and 2.71, respectively.

2.1.3. Water

Drinkable tap water was used as mixing water.

2.1.4. Chemical admixtures

In this study, a polycarboxylate-based superplasticizer and a permeability-reducing admixture were used. The properties of the plasticizer admixture and PRA based on manufacturer company analysis are given in Table 2.

Table 2. Properties of polycarboxylate-based superplasticizer and PRA.

Product	Appearance	Density (gr/cm^3)	pH	Chloride content (%)	Alkali Content (%)
Super Plasticizer	Brown-liquid	1.097	3.80	<0.1	<10
PRA	Yellow-liquid	1.13±0.02	9.80	<0.1	<0.4

2.2. Methods

2.2.1. Production of concrete mixtures

Concrete samples were produced with the use of three different cement dosages. In addition, two different types were produced from each sample type, with and without permeability-reducing admixtures, and a total of six different concrete mixes were produced. Concrete mix proportions are given in Table 3. While the superplasticizer was used as 1.6% by weight of the total binder, the permeability-reducing admixture was used as 2% of the cement. The dosages were determined based on manufacturers' recommendations.

Table 3. Concrete mix proportions (kg/m3).

Materials	D300	D300+PRA	D315	D315+PRA	D330	D330+PRA
Cement	300	300	315	315	330	330
Blast Furnace Slag	50	50	50	50	50	50
Water	147	147	153.3	153.3	159.6	159.6
Aggregate 1 (0-5mm)	899	899	889	889	874	874
Aggregate 2 (5-15mm)	430	430	426	426	419	419
Aggregate 3 (15-22mm)	526	526	520	520	512	512
Air content (%V)	2	2	2	2	2	2
Superplasticizer (SP)	5.6	5.6	5.84	5.84	6.08	6.08
PRA	-	6	-	6.30	-	6.60

The materials given in Table 3 were used in concrete production in accordance with the TS802 standard [25]. First, the dry mix was made by mixing cement, BFS, sand, and aggregates for 1-2 minutes. Then, some water was added, and the mixing continued. Superplasticizer was added to the mixture with the remaining water and mixing was continued for 2 more minutes. While the mixing process was continuing, a permeability-reducing admixture was added, and the mixing continued for 5 minutes. For the present experiments, 150 mm × 150 mm × 150 mm cubes and 100 mm x 200 mm cylindrical concrete samples were prepared. The samples were removed from the molds after 24 hours and cured in water until the day of the experiments.

2.2.2. Slump test

The test method was conducted according to TS EN 12350-2 standard [26]. The S3 class (10–15 cm) was chosen as the slump. Samples that gave slump in this range were cast into molds. In addition, the effect of PRA on the fresh state was examined. An image taken during the slump value measurement is shown in Figure 2.

Figure 2. Slump test.

2.2.3. Compressive strength test

According to the TS EN 12390-3 standard [27], the 7 and 28-day compressive strengths of cylindrical concrete samples (100mm×200mm) were determined. Three samples were used for each species. The appearance of the cylindrical concrete sample in the compressive strength press is shown in Figure 3.

Figure 3. Compressive strength measurement of a cylindrical concrete sample.

2.2.4. Depth of water penetration under pressure

The test method was used to determine the effect of PRA on the depth of water penetration at various cement dosages and it was carried out in accordance with the TS EN 12390-8 standard [28]. At 28 days of age, a 150 cm edge of cubic concrete samples were placed into the device and 500 kPa water pressure was applied for 72 hours. At the end of 72

hours, the sample removed from the device was split in half and the depth of water was measured with a digital caliper. Three samples were used for each species.

3. Results and Discussion

3.1. Slump

The permeability of concrete is largely influenced by its ability to be placed into a mold in a fresh state. Therefore, the negative effects of admixtures on slump value will directly affect hardened properties. The slump values of the concrete produced in the study are presented in Figure 4. Besides the control samples, all the samples containing admixtures were kept in the S3 slump class. Slump values decreased in the samples with all cement dosages. Slump values remained within the limits in all 3 sample types. PRA did not have any significant negative effects on workability. It was observed that PRA and the superplasticizer interact successfully. The effect of the decrease in slump values was observed to be primarily caused by cement. In a study by Michael et al. [29], it was found that permeability reducing admixture had no significant effect on slump value and did not affect workability properties, in parallel with this study.

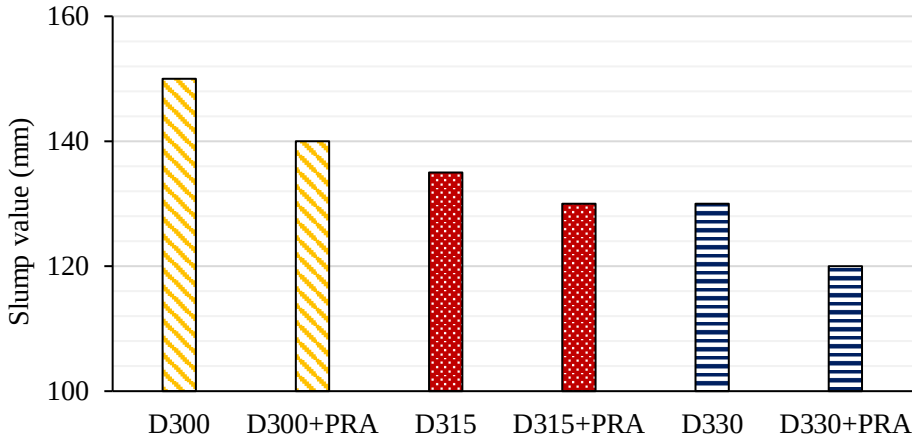

Figure 4. The slump values of all concrete mixtures.

3.2. Compressive strength

7 and 28-day compressive strength tests were conducted to observe the effect of PRA on compressive strength. The 7-day compressive strength results are presented in Figure 5. It was observed that PRA increased compressive strength by 9.44%, 5.33%, and 3.28% at cement dosages of 300, 315, and 330 kg/m3, respectively. The reason for this contribution is that PRA crystallized in the voids of concrete and so created a fuller volume. The effect of admixture continued as the concrete strength classes increased, but its effect decreased as the void ratio of concrete decreased. Thus, the effect of PRA was reduced by clogging fewer gaps. It was reported in a study by Yu et al. [16] that PRA supplementation to C30 and C40 concrete mixtures yielded similar results to the present ones, and the rate of contribution of PRA in strength decreased as the concrete grade increased.

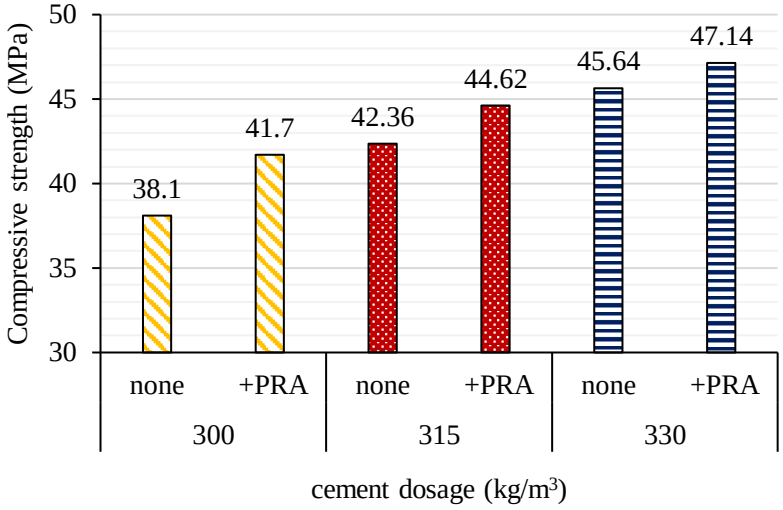

Figure 5. The 7-days compressive strength results.

The 28-day compressive strength results are presented in Figure 6. It was observed that PRA increased compressive strength by 4.35%, 2.78%, and 2.02% at cement dosages of 300, 315, and 330 kg/m3. Similar to the 7-day results, the contribution rate of the admixture to compressive strength decreased as cement dosage increased. However, it still contributed to increasing the compressive strength at each cement dosage.

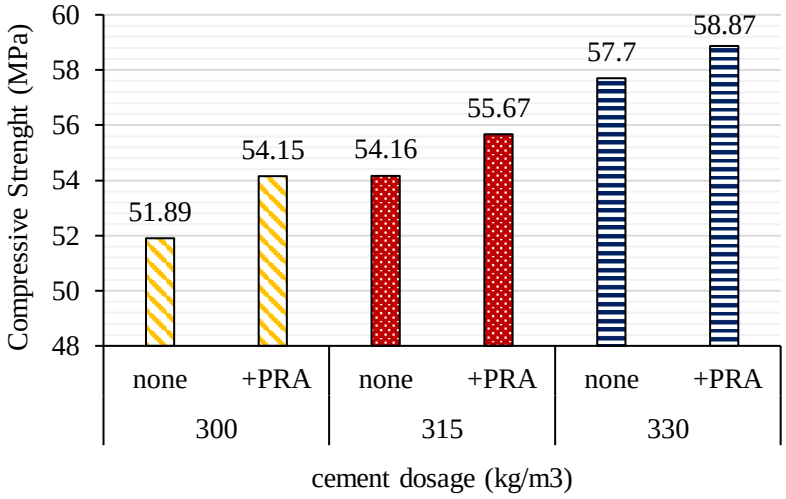

Figure 6. The 28-day compressive strength results.

3.3. Depth of water penetration under pressure

Three samples from each sample type were used for the test. A sample whose water penetration depth was measured during the experiment is presented in Figure 7. The average results are presented in Figure 8.

Figure 7. The process of measuring the depth of water penetration.

There are numerous pores in concrete structures, and these pores affect the permeability properties of concrete in many ways [30]. Crystal structures formed by using chemical admixtures can form in these pores and reduce the depth of water penetration values [31]. In parallel to this, in this study, PRA decreased the depth of water penetration in 300, 315, and 330 kg/m3 cement dosages by 22.06%, 26.90%, and 1.93%, respectively. A decreased depth of water penetration was observed when the cement dosage was increased from 300 to 315 kg/m3 in additived samples. However, the decrease due to increasing cement dosage was lower compared to the decrease owing to the use of PRA. This result is parallel to the study of Hassani Esgandani [32].

At these 300 and 315 kg/m3 cement dosages, the concrete structure had adequate voids that provided a suitable area for the crystallization of PRA. However, at a cement dosage of 330 kg/m3, suitable voids were not created for crystallization because the voids were already closed due to cement hydration. Thus, PRA was not effective at this dosage. At a cement dosage of 315 kg/m^3, the depth of water penetration decreased by up to 26.90% due to PRA supplementation into the concrete mixture. However, the effect of PRA on the depth of water penetration decreased with increasing cement dosage (330 kg/m^3). In previous studies, it has been observed that this type of admixture also contributes positively to self-healing behavior [33]. This study determined that PRA is more effective at lower dosages because it needs larger pores and cracks for its crystallization.

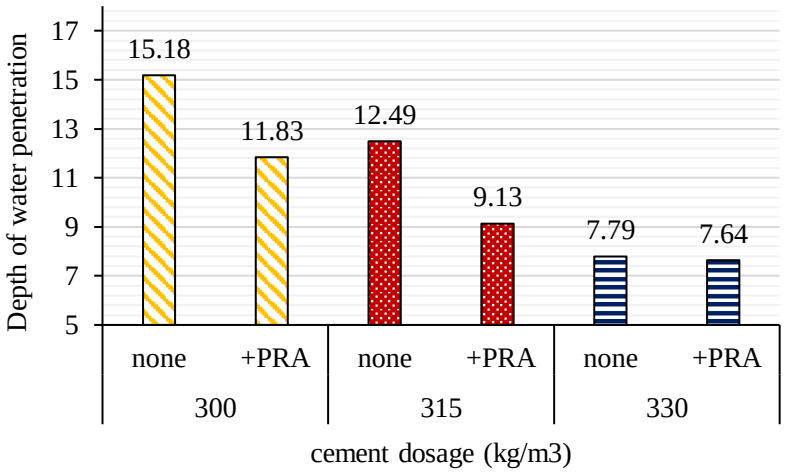

Figure 8. Depth of water penetration under pressure.

4. Conclusion

In this study, concrete samples containing three different cement dosages were produced, and the effects of PRA on the slump, compressive strength, and depth of water penetration were investigated. The following conclusions were drawn from the present findings:

- Although PRA worked in compliance with the superplasticizer, PRA generally reduced slump values, but present slump values were still within the limits.
- PRA increased the compressive strength values at all cement dosages. However, as the cement dosage increased, the compressive strength increased as expected, while the positive effect of the admixture on the strength decreased. At the lowest cement dosage, PRA had the highest effect (9.44%). In addition, as the curing day increased to 28 days, the contribution of the admixture to compressive strength decreased. While the compressive strength increased due to the closing voids because of the hydration of the cement, the effect of the admixture decreased because these voids were areas for the crystallization of the admixture to be formed.
- PRA was the most effective on the depth of water penetration under pressure. Decreases in water penetration depth of up to 26.90% were observed. However, while it was observed that the admixture was quite effective up to a certain dosage, the effect was quite low at high cement dosage.

References

[1] Akkaya, Y., Bayramov, F., and Taşdemir, M.A. (2003). Betonun kırılma mekaniği: tasarımda kullanılan mekanik özellikler ile kırılma parametreleri arasındaki bağıntılar. Türkiye Mühendis Haberleri; 426, 70–5.

[2] Baghabra Al-Amoudi, OS., Al-Kutti, WA., Ahmad, S., and Maslehuddin, M. (2009). Correlation between compressive strength and certain durability indices of plain and blended cement concretes. Cem Concr Compos 2009;31:672–6. https://doi.org/10.1016/j.cemconcomp.2009.05.005.

[3] Yıldırım, M., Bilir Özhan, H. (2023). Residual Durability Performance of Glass Fiber Reinforced Concrete Damaged by Compressive Stress Loads. Period Polytech Civ Eng https://doi.org/10.3311/PPci.21387

[4] Onaran, K. (2000). Malzeme Bilimi, Bilim Teknik Yayınevi, İstanbul, 244–55 (8).

[5] Sümer, M. (1994). Harçlarda Kılcal ve Basınçlı Su Altındaki Geçirimsizliğin Su-Çimento Oranı ile Değişimi, İMO Tek Dergi, 743–53.

[6] Özalp, F. (2016). Kür Koşulları ve Yalıtımın Yüksek Dayanımlı Betonların Geçirimlilik, İç-Yapı ve Mekanik Özeliklerine Etkileri. Phd Thesis. İTÜ, İstanbul.

[7] Singh, SB., Munjal, P., and Thammishetti, N. (2015). Role of water/cement ratio on strength development of cement mortar. J Build Eng, 4:94–100. https://doi.org/10.1016/j.jobe.2015.09.003.

[8] Ahmad, O.A., (2017). Production of High-Performance Silica Fume Concrete. Am J Appl Sci, 14:1031.1038. https://doi.org/10.3844/ajassp.2017.1031.1038.

[9] Detwiler, R.J., and Mehta, P.K. (1989). Chemical and Physical Effects of Silica Fume on the Mechanical Behavior of Co8ncrete. Mater J, 86:609–14. https://doi.org/10.14359/2281.

[10] Yeau, K.Y., and Kim, E.K. (2005). An experimental study on corrosion resistance of concrete with ground granulate blast-furnace slag. Cem Concr Res, 1391–9 (35). https://doi.org/10.1016/j.cemconres.2004.11.010.

[11] American Concrete Institute, editor. (2010). Report on chemical admixtures for concrete. 1. Print. Farmington Hills, MI: American Concrete Institute.

[12] Bilir Özhan, H., and Yildirim, M. (2020) Effects of Acid and High-Temperature Treatments on Durability of Bacterial Concrete. Uludağ Univ J Fac Eng , 1421–30. https://doi.org/10.17482/uumfd.816087.

[13] Riding, K.A., Tibbetts, C.M.,and Ferraro, C.C. (2020) Testing Methods to Assess the Durability of Concrete Permeability Reducing Admixtures. University of Florida. Dept. of Civil and Coastal Engineering.

[14] Yildirim, M., Özhan Bilir, H., Öz Girgin, H. (2023) Bacteria-based self-healing of cement mortars loaded at different levels and exposed to high temperature. Mag Concr 1–11. https://doi.org/10.1680/jmacr.22.00238.

[15] Teng, L.W., Lin, W.T., Chen, J., and Cheng, A., Hsu, H.M. (2014). The Component Analysis of Penetration Sealer Materials. Adv Mater Res, 842:74–7. https://doi.org/10.4028/www.scientific.net/AMR.842.74.

[16] Yu, Y., Yu, J., and Ge, Y. (2016). Water and chloride permeability research on ordinary cement mortar and concrete with compound admixture and fly ash. Constr Build Mater, 127:556–64. https://doi.org/10.1016/j.conbuildmat.2016.09.103.

[17] Tibbetts, C.M., Riding, K.A., and Ferraro, C.C. (2021). A critical review of the testing and benefits of permeability-reducing admixtures for use in concrete. Cement. https://doi.org/10.1016/j.cement.2021.100016.

[18] Munn, R.L., Chang, Z.T., and Kao, G. (2005). Performance of Australian Commercial Concretes Modified with a Permeability Reducing Admixture, Melbourne, Australia, (5) 11–7.

[19] Vessalas, K., Sirivivatnanon ,V., and Baweja, D. (2017) Influence of Permeability-Reducing Admixtures on Water Penetration in Concrete. ACI Mater J, 114. https://doi.org/10.14359/51701002.

[20] Hassani Esgandani, M., Vessalas, K., Baweja, D., and Schmidt, Z. (2014) Effect Of Chemical Admixtures On Water Penetration Of Concrete. RILEM Int. Workshop Perform.-Based Specif. Control Concr. Durab., RILEM.

[21] ACI Committee 212, (2016) American Concrete Institute. Report on chemical admixtures for concrete.

[22] Khatib, J.M, and Clay, R.M. (2004). Absorption characteristics of metakaolin concrete. Cem Concr Res 34:19–29. https://doi.org/10.1016/S0008-8846(03)00188-1.

[23] Akyol K. (2008). Su Yalıtımı ve Su Geçirimsizlik Katkı Oranlarının Beton Su Emmesine ve Basınç Dayanımına Etkilerinin Araştırılması. Master Thesis. Sakarya Üniversitesi.

[24] TS EN 197-1 / A3. (2012) Cement - Part 1: Composition, specifications and conformity criteria for common cements. Ankara

[25] TS 802. (2016). Design Concrete Mixes. Ankara.

[26] TS EN 12350-2. (2019). Testing fresh concrete - Part 2: Slump test. Ankara.

[27] TS EN 12390-3. (2019). Testing hardened concrete - Part 3: Compressive strength of test specimens. Ankara.

[28] TS EN 12390-8, (2019). Testing hardened concrete - Part 8: Depth of penetration of water under pressure. Ankara.

[29] Michael, J., Smith, S. H., Durham, S. A., and Chorzepa, M. G. (2018). Crack control in concrete walls through novel mixture design, full-scale testing, and finite element analysis. Construction and Building Materials, 166, 301-314. https://doi.org/10.1016/j.conbuildmat.2018.01.081.

[30] Halamickova, P., Detwiler, R. J., Bentz, D. P., and Garboczi, E. J. (1995). Water permeability and chloride ion diffusion in Portland cement mortars: relationship to sand content and critical pore diameter. Cement and concrete research, 25(4), 790-802. https://doi.org/10.1016/0008-8846(95)00069-O.

[31] Azarsa, P., Gupta, R., and Biparva, A. (2018). Crystalline waterproofing admixtures effects on self-healing and permeability of concrete. In Proceedings of the International Conference on New Horizons in Green Civil Engineering, University of Victoria, Victoria, BC, Canada, 25-27.

[32] Hassani Esgandani, M. (2017). Role of binder, permeability-reducing admixtures and cracking in the watertightness of concrete structures (Doctoral dissertation). University of Technology Sydney.

[33] Roig-Flores, M., Moscato, S., Serna, P., and Ferrara, L. (2015). Self-healing capability of concrete with crystalline admixtures in different environments. Construction and Building Materials, 86, 1-11. https://doi.org/10.1016/j.conbuildmat.2015.03.091.

J Inno Sci Eng,2023, 7(1):60-73
http://doi.org/10.38088/jise.1183127

Research Article

Coefficient of Acceptability for Joints in Furniture Frame Analysis under Cyclic Loads

Mesut Uysal [1*]

[1*] *Department of Forestry Industrial Engineering, Faculty of Forestry, Bursa Technical University, Bursa, 16310*

Cite this paper as:
Uysal, M. (2023). *Coefficient of Acceptability for Joints in Furniture Frame Analysis under Cyclic Loads*. Journal of Innovative Science and Engineering.7(1):60-73

*Corresponding author: Mesut Uysal
E-mail: mesut.uysal@btu.edu.tr

Received Date:02/10/2022
Accepted Date:24/02/2023

Abstract

This study aimed to determine the coefficient of acceptability for furniture joints on chair frames. In doing so, three chair configurations made of soft maple and yellow poplar were defined. Chairs were subjected to a front-to-back cyclic load test until non-recoverable failure occurred. Ultimate failure loads for each chair frame were used to determine the moment capacity of critical joints. Likewise, according to American Library Association, acceptable light, medium and heavy-duty service loads were subjected to chairs in the structural analysis to obtain acceptable moment capacities of critical joints, using the stiffness method. Then, lines were drawn from the initial strength of the joint to the moment capacities of the joint at the load level imposed on the chair. Differentiating the slopes between lifeline and acceptable levels gave a coefficient of acceptability. This coefficient would provide insight into the serviceability and durability of joints and chair frames.

Keywords: Cyclic load, Chair frames, Round mortise and tenon joints, Acceptance level, Performance test.

1. Introduction

The rational design of furniture dictates that any member and joint could be designed if their moment capacities are known [1]. Besides, joint design is vital in the strength design of the furniture even though it is its last step [2]. Most of the failures on chairs are owing to failed or loose joints rather than members [3]. Reliability of the joints results in the reliability of the chair because the strength of the chair depends on the weakest joints [4]. Therefore, the initial strength of a joint and its moment under imposed load were taken into consideration in this study to estimate the coefficient of acceptability. This estimation should give insight into the serviceability of the chair frames` life.

The performance test of chairs is a realistic load model with cyclic loads to assess a typical utilization and mode of failure in their service. In initial life, a chair has full strength based on its member and joint design, but the initial strength will decrease in service due to fatigue. Therefore, it fails before it cannot reach its initial strength. The ratio between the static load capacity of a chair and stepwise cyclic load capacity is 56% [5]. In the case of constant cyclic load subjected to the chair, failure occurred at 20% and 30% of the initial strength [6,7]. On the contrary, to evaluate the cyclic load capacity of a chair, American Library Association (ALA) specifications is used. This specification sets acceptable light, medium and heavy-duty service loads according to the loading application [8]. However, benchmarking the load capacity of the structure with these load levels results in a pass/fail criterion.

Likos et al. [9] studied a relationship between static load and cyclic load capacity of chair frames and stated that the ratio between cyclic and static load was 2/3. In another study, the relationship between the cyclic load capacity of full-frame chairs and the static load capacity level of T- and L-shaped joints was studied to estimate the cyclic load capacity level of full-frame chairs from the static load level of joints [10]. In doing so, an equation was established from this approach, and the average difference between test results and estimated values of full-frame chairs was 13%. Kasal et al. [11] studied performance test results of chair frames made of different tenon sizes. In this study, the cyclic load capacity of full-frame joints was estimated by using the static load capacity of joints, and the average ratio between them was 1,04. Kılıç et al. [12] studied performance test results under cyclic load in the experiment and finite element analysis. The estimated test result was used to compare with the ALA specification. Kuşkun et al. [13] studied the cyclic load capacity level of the full-frame chair and resulted that larger tenon sizes provided a highly acceptable rate for chairs. These studies give an insight into whether a chair passes or fails the performance test. On the other hand, the acceptability rate should be an intermediate coefficient to estimate how much better quality a chair would acquire during service life.

In this study, acceptability coefficients for critical joints on chair frames were estimated by comparing the lifeline of the joints and their acceptable levels. In doing so, three chair frames with one, two, and three stretchers made of both soft maple and yellow poplar wood were defined. Front-to-back cyclic load tests were applied horizontally on chairs, and cyclic load capacity levels were obtained. By stiffness method, critical joints with the highest moment were considered. Then, differentiation between slopes of the initial strength-to-failure moment and initial strength-to-acceptable levels was used to estimate the coefficient of acceptability.

2. Material and Methods

2.1. Materials and Construction of Furniture Frames

In this study, soft maple (Acer macrophyllum) and yellow poplar (Liriodendron tulipifera) wood specimenswere used in furniture construction. All 1-m long boards were obtained from a local sawmill in Northern Indiana, USA. Table 1 indicates some mechanical properties of these wood species.

Table 1. Some mechanical properties of soft maple and yellow poplar [14]

Wood species	Specific gravity	Modulus of rupture (N/mm^2)	Modulus of elasticity (N/mm^2)	Compression parallel to grain (N/mm^2)	Shear parallel to grain (N/mm^2)	Tension perpendicular to grain (N/mm^2)
Sugar maple	0.48	74	10000	41.0	11.9	3.7
Yellow poplar	0.42	70	10900	38.2	8.7	3.7

All boards were conditioned at 7% moisture content at least one month and then subsequently machined to dimensions for each member given in Table 2. All components were sequentially numbered and taken from a material pool, and each furniture member was randomly selected from this material pool.

Table 2. Member sizes for chair frame

Member	Thickness (mm)	Width (mm)	Length (mm)
Front leg	38.10	38.10	431.80
Rear leg	38.10	38.10	863.60
Stretcher	22.22	22.22	431.80

Round tenons, 19.05 mm-diameter and 38.10 mm-long, were cut in the tenoning machine, and matching mortises were machined on the drill press with tolerances of 0.254 mm (Figure 1). Tolerances were such that a tenon could be inserted 2/3 of its length into a mortise without using force [15].

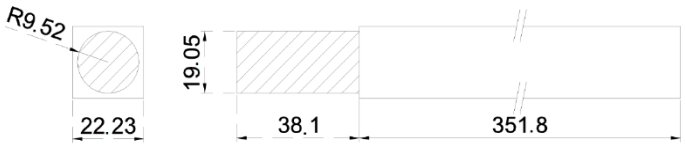

Figure 1. Configuration of the round mortise and tenon joints

40% solid content polyvinyl acetate (PVA) adhesive was used to coat the faces of the tenon and the mortise walls, and the full length of the tenon was inserted into the mortise and clamped in place. Specimens were clamped, remained at least 24 h and were stored in a conditioning room at 7% moisture content for at least one week before they were tested [16]. The side frame configurations of the chairs were given in Figure 2.

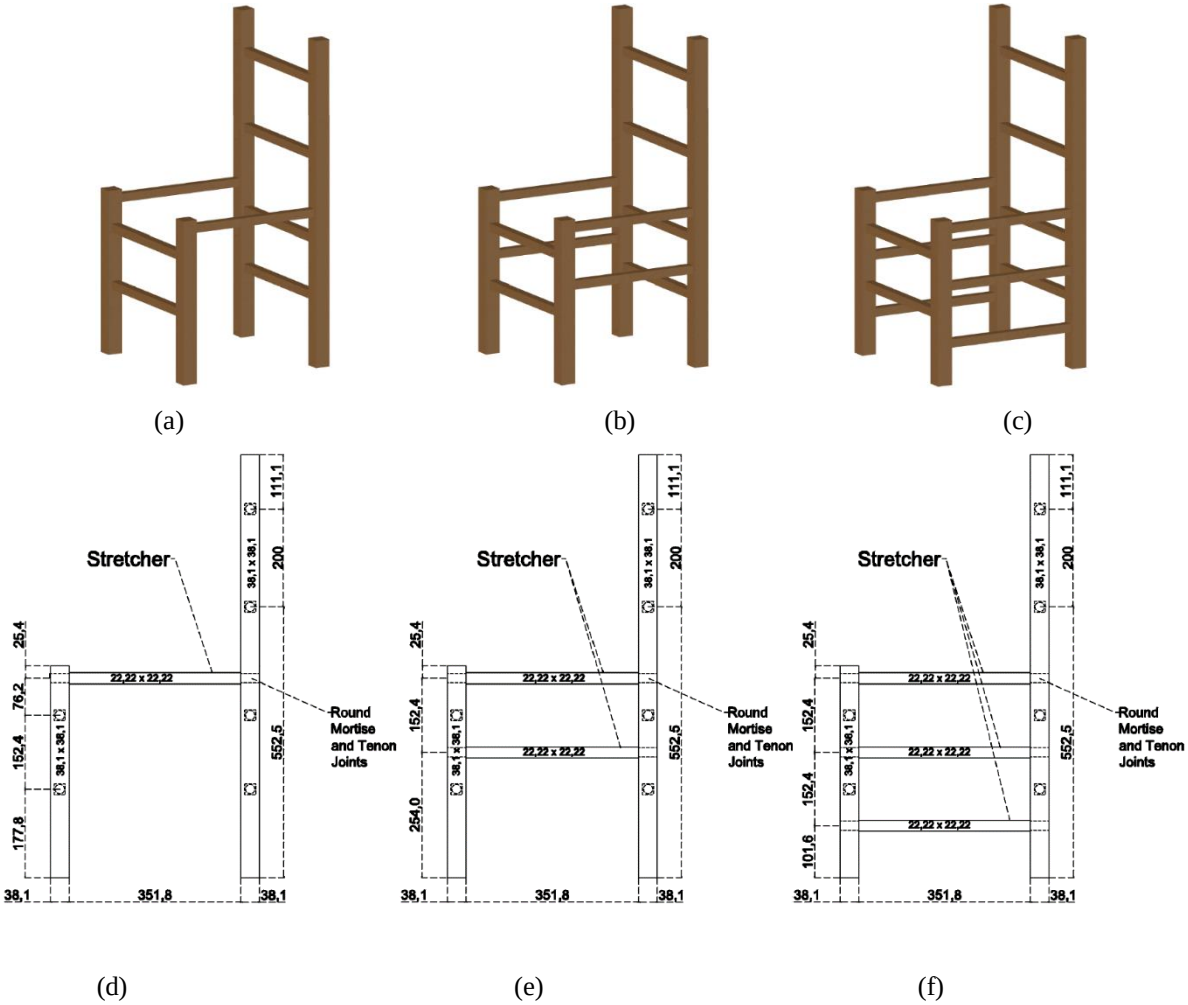

Figure 2. Configuration of the full-frame chair with a. one stretcher, b. two stretchers, and c. three stretchers, and dimensions and position of joints on side chair with d. one stretcher, e. two stretchers, and f. three stretchers

2.2. Performance Test of Chair Frames and Stiffness Method for Hyperstatic Frame Analysis

In the test procedure, a chair was mounted for the test shown in Figure 3. Reaction brackets were used to prevent chairs from sliding on the platform. A chain was passed over the front-to-back seat, connected to the load head on one end, and anchored to the platform on the other. In doing so, chairs were subjected to horizontal front-to-back load.

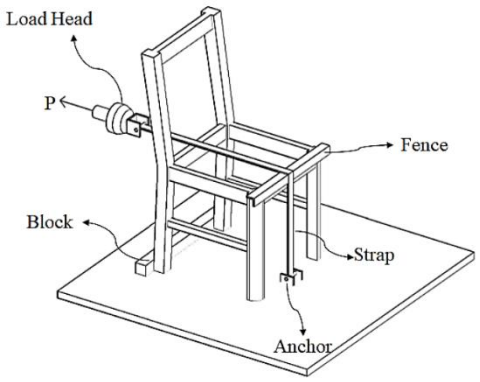

Figure 3. Configuration of the front-to-back cyclic load test set-up

Stepwise front-to-back cyclic load tests were imposed on the chair frames with an initial load of 222.50 N. Loads were applied on the chairs with a speed of 20 cycles/min. After 25000 cycles were completed, the load level was incremented to 111.25 N, and then the subsequent step started. Tests were continued until non-recoverable failure occurred or horizontal deflection exceeded 50 mm [8]. After the failure load level and cycle were obtained, the equation 1 was used to calculate the ultimate cyclic load level [17].

$$F_{C,ul} = (F_{C,fail} - F_i) + \left(F_i \times \frac{N_{C,fail}}{25000}\right) \quad (1)$$

where,

FC,ul: ultimate cyclic load level (N)
FC,fail: Cyclic failure load (N)
Fi: Incremental load (N)
NC,fail: Failure cycle.

In a structural analysis of the furniture frames, the degree of determinacy is significant to apply the structural analysis method. In the case of a side frame analysis, front and back legs were joined with a single member, rail, or stretcher. It is an isostatic structure (degree of determinacy is 0), so equilibrium equations can be used to get initial strength on joints. On the other hand, if one more stretcher is used in the side frame, the degree of determinacy is equal to 1, and the structure will be hyperstatic. Thus, equilibrium equations will not be enough in the structural analysis of the frame. Instead, the stiffness method is one of the intermediate procedures for the structural analysis of hyperstatic structures. The degree of determinacy is calculated by;

$$s = m + h - 3j \quad (2)$$

s: degree of indeterminacy
m: number of members
j: number of joint
h: number of degrees of freedom.

A structure contains members and joints called elements and nodes in the stiffness method, respectively. A node has 3 degrees of freedom and an element has 6 degrees of freedom (Figure 4). In the stiffness method, the structure is analyzed element by element, and an element stiffness matrix is used for each member. Afterward, each element stiffness matrix is accumulated to obtain a global stiffness matrix (for frame analysis). This global stiffness matrix relates global loadings and global displacements, resulting in internal forces and deflections on member ends. The stiffness method is applied as eq. 3 to eq. 9 [18].

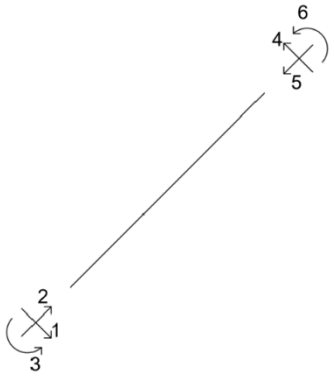

Figure 4. Degrees of freedom for element stiffness

$$\{Q\} = [K] \times \{D\} \quad (3)$$

$$[K] = \sum_{i=1}^{n} k_i \quad (4)$$

$$[k] = [T]^T \times [k'] \times [T] \quad (5)$$

$$k' = \begin{bmatrix} AE/L & 0 & 0 & -AE/L & 0 & 0 \\ 0 & 12EI/L^3 & 6EI/L^2 & 0 & -12EI/L^3 & 6EI/L^2 \\ 0 & 6EI/L^2 & 4EI/L & 0 & -6EI/L^2 & 2EI/L \\ -AE/L & 0 & 0 & AE/L & 0 & 0 \\ 0 & -12EI/L^3 & -6EI/L^2 & 0 & 12EI/L^3 & -6EI/L^2 \\ 0 & 6EI/L^2 & 2EI/L & 0 & -6EI/L^2 & 4EI/L \end{bmatrix} \quad (6)$$

$$T = \begin{bmatrix} \lambda_x & -\lambda_y & 0 & 0 & 0 & 0 \\ \lambda_y & \lambda_x & 0 & 0 & 0 & 0 \\ 0 & 0 & 0 & 0 & 0 & 0 \\ 0 & 0 & 0 & \lambda_x & -\lambda_y & 0 \\ 0 & 0 & 0 & \lambda_y & \lambda_x & 0 \\ 0 & 0 & 0 & 0 & 0 & 0 \end{bmatrix} \quad (7)$$

$$\lambda_x = cos\theta_x \quad (8)$$

$$\lambda_y = cos\theta_y \quad (9)$$

where,

Q: Global loadings for structure (N)
K: Global stiffness matrix for structure
D: Global displacements for structure (mm)
k_i: global stiffness matrix
n: number of elements
T: Force transformation matrix
k': element stiffness matrix
A: cross-section area of elements
E: Elasticity of material used in elements
L: Length of the element
I: Moment of inertia of the element
θ_x: angle of the element to the x-axis
θ_y: angle of the element to the y-axis.

2.3. Determination of the coefficient of acceptability

The overall strength of the structure reduces under dozens and hundreds of loadings in the course of its life span. Prediction of these loading in service is complicated (Figure 4.a). A furniture construction has an initial load capacity – ultimate load capacity – but it would be subjected to normal and abusive loads during its service life. The first crossing point is load level when imposed load and material strength cross each other. At this point, internal forces on joints or members initiate to exceed material strength capacity, so the structure itself is expected to fail. Load level at failure is compared to American Library Association (ALA) specifications to determine whether it passes or fails to light, medium, and heavy-duty acceptable load levels (Figure 4.b).

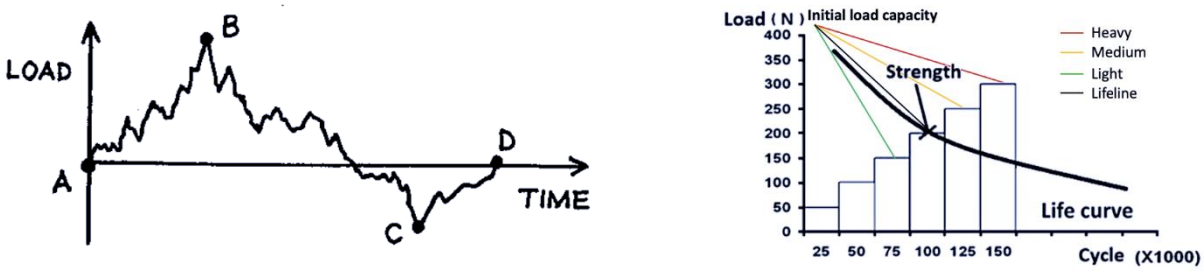

(a) (b)

Figure 4. a. Irregular load history in structure [19] and b. Relationship between load steps and product strength [20]

The bending moment capacity of RMT joints is calculated via eq. 10 and eq. 11, and then, it is multiplied by 3 to obtain its initial load capacity by considering the allowable bending capacity of wood in bending [2].

$$M_s = 0.97 \times \frac{W}{D^{1.5}} \times M \tag{10}$$

$$M = k \times \frac{\pi \times D^3}{32} \times \sigma_E \tag{11}$$

where,

M_s: The bending moment capacity of the tenon with shoulder
W: the width of the stretcher
D; Diameter of the tenon
M: Bending moment capacity of tenon without shoulder
k: coefficient (1.18)
σ_E: Modulus of rupture of materials used in the tenon.

The coefficient of acceptability (CoA) is calculated by differentiating the slope of the lifeline (m_L) and the slope of i^{th} acceptable load level (m_i) (i: light, medium, or heavy).

$$CoA = \frac{m_i - m_L}{m_L} \tag{12}$$

$$m = \frac{y_2 - y_1}{x_2 - x_1} \tag{13}$$

3. Results and Discussions

3.1. Front-to-Back Cyclic Load Capacity

Front-to-back cyclic load capacity determines the strength of the furniture construction because imposed load which is subjected during sitting and tilting on a chair in its service life is most likely to be encountered. According to the test results (Table 3 and Figure 5), the cyclic load capacity level increased by increasing the number of stretchers for chairs made of soft maple and yellow poplar wood. Cyclic load capacity for chairs made of soft maple wood with three stretchers was 76.56% and 771.87% higher than those of two stretchers and one stretcher, respectively. Likewise, chairs made of yellow poplar wood presented the same pattern; namely, chairs with three stretchers had 85.56% and 271.56% more strength than those of two stretchers and one stretcher, respectively.

Table 3. Results of front-to-back cyclic load test

Wood Species	# of Stretcher	Failure Load (N)	Failure Cycle	Ultimate Load (N)
Soft Maple	3	2002.50	11829	1943.76
	2	1112.50	22360	1100.93
	1	333.75	101	222.94
Yellow Poplar	3	2113.75	17829	2081.71
	2	1223.75	2063	1121.85
	1	667.50	817	560.26

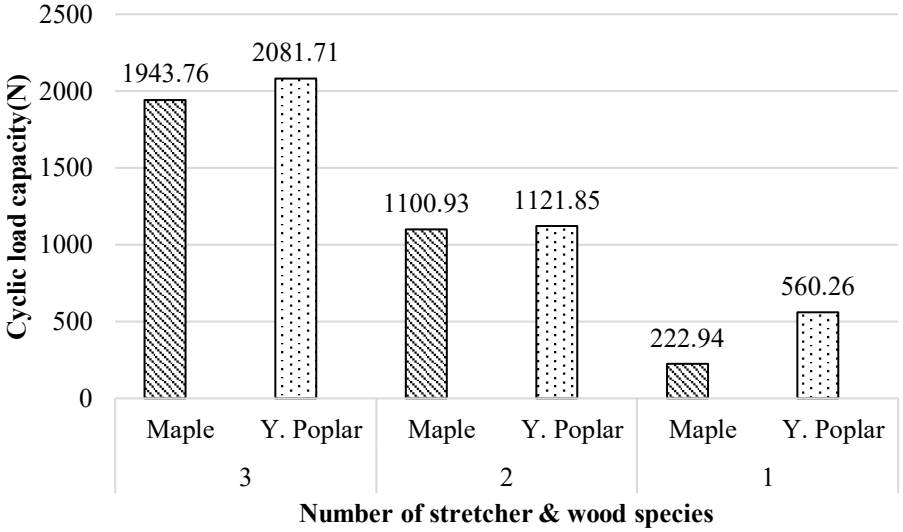

Figure 5. The ultimate cyclic load capacity of the chair frames

3.2. Structural Analysis of Chair Frame

Three chair configurations were defined, and each node on the chairs was numbered as Figure 6. Table 4 showed bending moment at the nodes where the cyclic failure load was subjected to node 3 horizontally. Chairs made of both soft maple and yellow poplar wood with one stretcher had a bending moment of 45.30 N.m and 113.83 N.m on node 2, respectively. Those of two and three stretchers had 84.69 N.m, 58.62 N.m, 86.43 N.m, and 62.58 N.m on node 4, respectively. As can be seen, an increasing number of stretchers in construction enhances the durability of the chair due to the fact that it causes a double-moment effect on members.

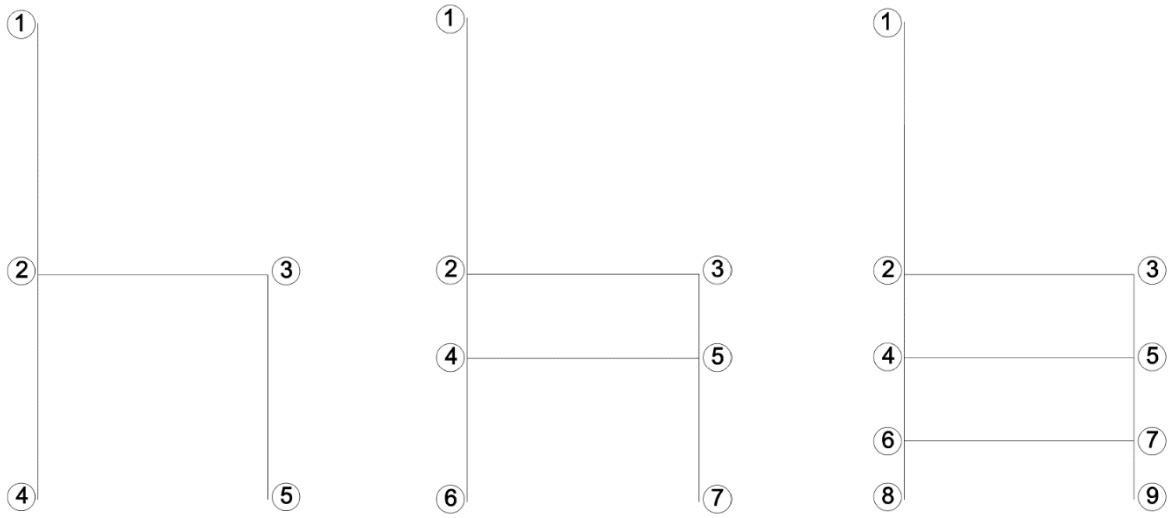

(a) (b) (c)

Figure 6. Nodes on chair frame for stiffness method

Table 4. Bending moment capacities on nodes at cyclic failure load (N.m)

Wood Species	# of stretchers	Nodes								
		1	**2**	**3**	**4**	**5**	**6**	**7**	**8**	**9**
Soft maple	1	0.00	**45.30**	0.00	0.00	0.00	-	-	-	-
	2	0.00	35.80	43.60	**84.70**	59.40	0.00	0.00	-	-
	3	0.00	44.81	43.90	**58.60**	58.40	43.90	43.10	0.00	0.00
Yellow poplar	1	0.00	**113.80**	0.00	0.00	0.00	-	-	-	-
	2	0.00	36.50	44.50	**86.40**	60.60	0.00	0.00	-	-
	3	0.00	47.10	46.90	**62.60**	62.50	47.00	46.00	0.00	0.00

*Note: The node having the highest moment capacity is shown in bold.

Table 5 demonstrates moment capacities on each node while acceptable load levels were imposed on chairs from node 3 horizontally. Likewise, the maximum moment occurred on node 2 for chairs with one stretcher, whereas on node 4 for chairs with two and three stretchers.

Table 5. Bending moment capacities on nodes at acceptable service load levels (N.m)

Load levels	# of stretchers	Nodes								
		1	**2**	**3**	**4**	**5**	**6**	**7**	**8**	**9**
Acceptable light-duty	1	0.00	**271.20**	0.00	0.00	0.00	-	-	-	-
	2	0.00	43.42	52.93	**102.78**	72.13	-	-	-	-
	3	0.00	30.21	30.12	**40.18**	40.07	30.15	29.51	-	-
Acceptable medium-duty	1	0.00	**317.50**	0.00	0.00	0.00	-	-	-	-
	2	0.00	50.66	61.76	**119.91**	84.15	-	-	-	-
	3	0.00	35.25	35.15	**46.88**	46.75	35.18	34.42	-	-
Acceptable heavy-duty	1	0.00	**406.91**	0.00	**0.00**	0.00	-	-	-	-
	2	0.00	65.13	79.40	**154.17**	108.19	0.00	0.00	-	-
	3	0.00	45.32	45.19	**60.27**	60.11	45.23	44.26	-	-

*Note: The node having the highest moment capacity is shown in bold.

3.3. The coefficient of acceptability for the critical joints

Figure 7 shows a trend from the initial life of the product to moments on critical joints at failure, acceptable light-duty service, acceptable medium-duty service, and acceptable heavy-duty service load. The initial moment capacity of the round mortise and tenon joints on chairs made of soft maple wood was 124.93 N.m, whereas those of yellow poplar was 141.78 N.m according to equation 10. In the case that initial moment capacities were higher than failure load and acceptable load levels, slopes presented a decreasing trend. On the contrary, they were in increasing trends ıf initial moment capacity were lower than failure load and acceptable load levels. Initial moment capacities for critical joints on chairs with one stretcher were lower than those of with acceptable load levels subjecting to chairs (Figure 7.a and 7.b). In Figure 7.c, d and e, initial moment capacities for critical joints on chairs with two stretchers made of both wood species and three stretchers made of soft maple wood were lower than the moments when acceptable heavy-duty service load was imposed on chairs. The slopes trending an increase from initial moment capacity to any moment capacity on nodes when acceptable load levels were applied stated that joints, and hence chairs, failed.

On the other hand, joints survived under imposed loads and passed the specified acceptable load capacity levels. Only chairs with three stretchers passed all the acceptance levels under horizontally front-to-back cyclic load. However, the chair made of soft maple wood failed to meet the acceptable heavy-duty service load level criteria. The purpose of the study is to determine the coefficient of the acceptability (CoA) of chairs in order to state how much chairs depending on critical joints performed better serviceability in the use of their life. Table 6 shows the coefficient of the acceptability for critical joints based on slopes between lifeline and acceptable service load. CoA was a positive value when that chair passed the performance test; otherwise, it is a negative value. Here, the coefficient of acceptability refers to how well serviceability is presented when the value is away from zero. For instance, the chair made of yellow poplar and soft maple wood with two stretchers passed the test with the moment capacity of 62.60 N.m and 58.60 N.m, respectively; namely, chairs made of yellow poplar had 6.83% greater strength than those of soft maple. On the other hand, the coefficient of the acceptability was differentiated 28.57% between chairs made of yellow poplar and the ones of soft maple wood; that is, not only the criteria about whether the product passed or failed the performance test and how much bending moment capacity on joints was obtained is significant but the coefficient of accessibility would also give a vital insight into serviceability and durability in their utilization in service.

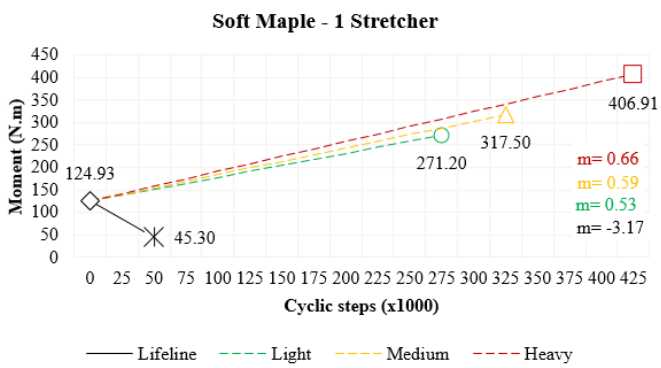

(a)

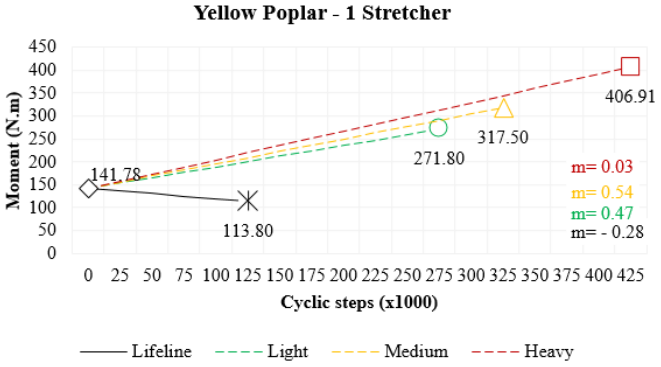

(b)

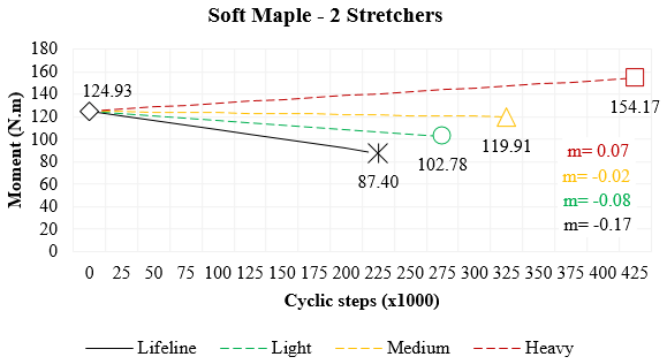

(c)

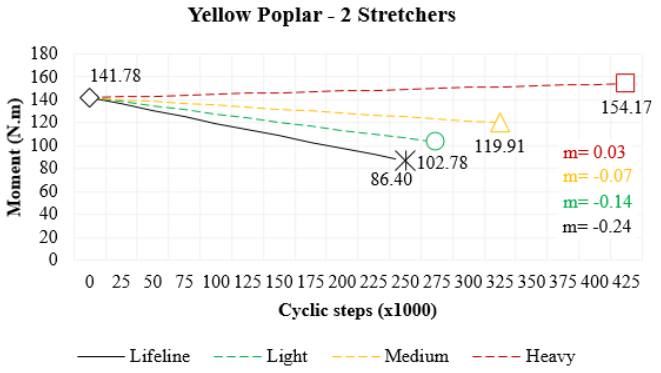

(d)

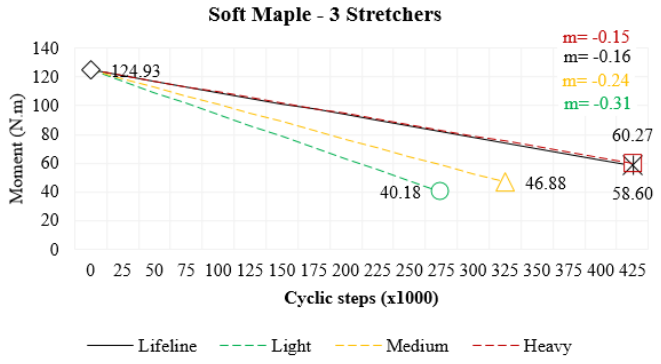

(e)

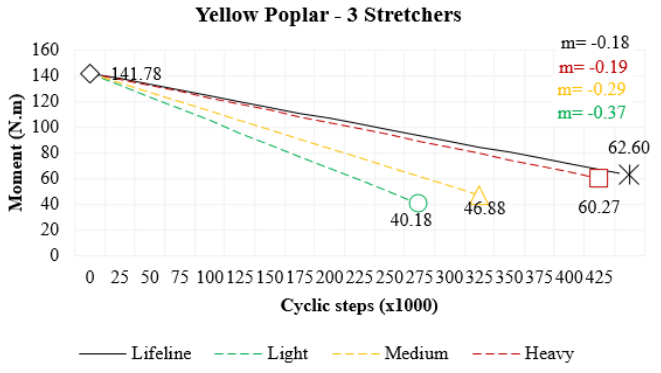

(f)

Figure 7. The slopes between moments on critical joints at failure, acceptable light-duty service, acceptable medium-duty service, and acceptable heavy-duty service load a. soft maple with one stretcher, b. yellow poplar with one stretcher, c. soft maple with two stretchers, d. yellow poplar with two stretchers, e. soft maple with three stretchers, and f. yellow poplar with three stretchers

Table 6. The coefficient of acceptability of critical joints and pass/fail criteria according to ALA specification

Wood Species	# of stretchers	Moment capacity at critical joints	Moment capacity at critical joint at acceptable light-duty cyclic load	Results	CoA	Moment capacity at critical joint at acceptable medium-duty cyclic load	Results	CoA	Moment capacity at critical joint at acceptable heavy-duty cyclic load	Results	CoA
Soft maple	1	45.30	271.20	Fail	-1.17	317.50	Fail	-1.19	406.91	Fail	-1.21
	2	87.40	87.42	Fail	-0.52	102.78	Fail	-0.91	119.91	Fail	-1.41
	3	58.60	40.18	Pass	0.91	46.88	Pass	0.49	60.27	Fail	-0.06
Yellow poplar	1	113.80	271.20	Fail	-2.70	317.50	Fail	-2.95	406.91	Fail	-1.11
	2	86.40	87.42	Fail	-0.42	102.78	Fail	-0.72	119.91	Fail	-1.12
	3	62.60	40.18	Pass	1.07	46.88	Pass	0.63	60.27	Pass	0.07

4. Conclusion

In this study, the coefficient of acceptability (CoA) for critical joints of chair frames was determined to provide insight into their serviceability and durability in service life. In doing so, three chair configurations made of soft maple and yellow poplar wood were used.

Critical joints on chair frames with one stretcher were node 2, whereas those of two and three stretchers were node 4. Based on moment capacities on these nodes obtained by imposing failure load and acceptable load level, joints, and hence chair frames, made of yellow poplar wood have greater strength than those of soft maple in in three-chair-configuration. Increasing the number of stretchers enhances chair durability because of the double-moment effect members; namely, the moment arm on the furniture member becomes narrower or the load is distributed to two and more members joined to one node when stretchers are added to the chair. Thus, the moment effect decreases on members or is fluctuated in both negative and positive zone on the moment diagram.

Knowing the initial strength of a joint is beneficial to design a durable and strong joint. Even theoretical structural analysis could determine whether a joint passes or fails according to an acceptable load level. According to the test results, the initial strength of joints for chairs with one and two stretchers did not meet any acceptable level, so they could fail in the early stage of their life. Besides, their CoA was negative, and their non-acceptability levels were high. On the other hand, when the number of stretchers increases, CoA turns to a positive value, e.g., chairs with three stretchers. In the light service load level, the CoA gives a better value of about 1; when severe load levels are applied, it is close to 0.

The CoA gives an insight into joint durability and serviceability in performance tests rather than only pass/fail tests. Therefore, if critical joints in chair frames are considered rather than full-frame strength in structural analysis, a better understanding of the lifetime or service of chair frames can be presented.

References

[1] Eckelman, C.A., Erdil, Y.Z and Haviarova, E. (2003). School Chairs for Developing Countries: Designing for Strength and Durability, Simplicity and Ease of Construction. For. Prod. J., 53: 1–8.

[2] Eckelman, C.A (2003) Textbook of product engineering and strength design of furniture. Purdue University, West Lafayette

[3] Zhang, J.L. , Quin, F. and Tackett, B. (2001). Bending strength and stiffness of two-pin dowel joints constructed of wood and wood composites. For. Prod. J., 51: 29–35. doi:10.1016/j.febslet.2005.03.016.

[4] Smardzewski, J. (2009). The reliability of joints and cabinet furniture, Wood Res., 54: 67–76.

[5] Kuskun, T. (2013). Effect of the tenon size and loading type on chair strength and comparison of actual test and finite element analyses results, M.S. Thesis. Mugla Sitki Kocman University, Mugla, Turkey. 123p

[6] Eckelman, C.A. (1974). Reasonable design stresses for woods used in furniture. Purdue Univ. Agric. Exp. Stn. Res. Bull., 916: 1–7.

[7] Ratnasingam, J., Ioras, F., and McNulty, F. (2010). Fatigue strength of mortise and tenon furniture joints made from oil palm lumber and some Malaysian timber. J. Appl. Sci., 10(22): 2869–2874.

[8] Eckelman, C.A. (1999). Performance test of side chairs. Holz Als Roh-Und Werkst., 57: 227–234.

[9] Likos, E., Haviarova, E., Eckelman, C.A., Erdil, Y.Z. and Ozcifci, A. (2013). Technical note: Static versus cyclic load capacity of side chairs constructed with mortise and tenon joints. Wood Fiber Sci., 45: 223–227.

[10] Kasal, A., Kuskun, T., Efe, H. and Erdil, Y.Z. (2015). Relationship between static front to back loading capacity of whole chair and the strength of individual joints. 27th Int. Conferance Reseach Furnit. Ind., Ankara, Turkey, 17 September 2015. pp. 422–429.

[11] Kasal, A., Kuskun, T., Haviarova, E. and Erdil, Y.Z. (2016). Static Front to Back Loading Capacity of Wood Chairs and Relationship between Chair Strength and Individual Joint Strength, BioResources, 11(4): 9359–9372. doi:10.15376/biores.11.4.9359-9372.

[12] Kiliç, H., Kasal, A., Kuşkun, T., Acar, M. and Erdil, Y.Z. (2018). Effect of tenon size on static front to back loading performance of wooden chairs in comparison with acceptable design loads, BioResources, 13(1): 256–271. doi:10.15376/biores.13.1.256-271.

[13] Kuskun, T., Kasal, A., Haviarova, E., Kilic, H., Uysal, M. and Erdil, Y.Z. (2018). Relationship between static and cyclic front to back load capacity of wooden chairs, and evaluation of the strength values according to acceptable design values. Wood Fiber Sci., 50(4): 402–410.

[14] Forest Products Laboratory – USDA (2010). Wood Handbook: Wood as an Engineering Material, USDA - General Technical Report,. Vol. General Te; ISBN: 1892529025.

[15] Uysal, M., Haviarova, E. and Eckelman, C.A. (2015). A comparison of the cyclic durability, ease of disassembly, repair, and reuse of parts of wooden chair frames. Material and Design, 87: 75–81. doi:10.1016/j.matdes.2015.08.009.

[16] Likos, E., Haviarova, E., Eckelman, C.A., Erdil, Y.Z., and Ozcifci, A., Effect of tenon geometry, grain orientation, and shoulder on bending moment capacity and moment rotation characteristics of mortise and tenon joints. Wood Fiber Sci., 44(4): 462–469.

[17] Uysal, M. and Haviarova, E. (2021). Evaluating Design of Mortise and Tenon Furniture Joints under Bending Loads by Lower Tolerance Limits. Wood Fiber Sci., 53(2) 109–125. doi:10.22382/wfs-2021-13.

[18] Hibbeler, RC. (2012). Structural Analysis, Pearson Prentice Hall, Upper Saddle River, New Jersey, 8th edition, 695 p. ISBN-13:978-0-13-257053-4.

[19] Nelson, D.V. (1979). Prediction of fatigue life under irregular loadings, Probabilistic Mechnanics Struct. Reliab., Tucson, Arizona, pp. 1–5.

[20] Erdil, Y.Z., Haviarova, E. and Eckelman, C.A. (2004). Product Engineering and Performance Testing in Relation. Wood Fiber Sci., 36(3) 411–416.

J Inno Sci Eng,2023, 7(1):74-87
http://doi.org/ 10.38088/jise.1170626

Research Article

Photovoltaic-Thermoelectric Power for Sustainable Cold Chains Needed for Covid-19 Vaccine Delivery and Use in Niger

Aichatou Galy Adam [1*], Bulent Yesilata [1]

[1] *Ankara Yildirim Beyazit University, Engineering and Natural Sciences Faculty, Energy Systems Engineering Department, Ankara, Turkey*

Cite this paper as:
Adam, G.A. and Yesilata, B. (2023). *Photovoltaic-Thermoelectric Power for Sustainable Cold Chains Needed for Covid-19 Vaccine Delivery and Use in Niger 7(1):74-87.*

*Corresponding author: Aichatou Galy Adam
E-mail: chatougaly@gmail.com

Received Date: 12/09/2022
Accepted Date: 13/03/2023

Available online at http://jise.btu.edu.tr/

Abstract

In areas where the access to an off-grid electricity is not possible or not reliable, the transport and conservation of vaccine and medicines is not possible. Nevertheless, these areas need and have right to access medicine. This need is much more critical nowadays since preservation of COVID-19 vaccines require cold-chain at some level of degree. Solar energy can be used to power the refrigerator destined to keep the medicines and vaccines cool. Even tough stand-alone photovoltaic (PV) is already used to power these coolers, our work shows that the use of a Photovoltaic-Thermoelectric hybrid generators could allow a great improvement of the autonomy. The output power of the PV alone and the hybrid are investigated under Niger meteorological conditions. These two systems coupled with a medical cooler are investigated. The results show that the hybrid system produces considerably more power to be stored in the battery, indicating much longer autonomy. Under the same conditions, when the PV reached its lowest efficiency of 12.24% , the hybrid was at his efficiency peak 19.62%. Thus, a rise of 5.88% was achieved. Our work presented here is important for giving a message to the international organizations that sustainable cold chains needed for equitable COVID-19 vaccine distribution is clearly possible with solar PV/TE driven DC refrigerators.

Keywords: COVID-19 vaccine cooler, DC refrigerator, Niger, PV/TE power, Solar PV, Efficiency

1. Introduction

Electricity is one of the most important assets in the development of a country. Electricity can be made using charcoal, uranium, petroleum, renewable energy, and so on. Niger is the fourth country worldwide to produce uranium, it also possesses a lot of gas and petroleum deposit (90000 barrels/day could be produced by the country), the sun irradiation is also non negligible, and it also has hydraulic potential due to its river.

Noting that Niger is rich in all these energy sources, it comes as a surprise that the country is not electrically independent. Indeed, in 2017, 73.8% [1] of the electricity used in the country comes from Nigeria. Noting that electricity is used for water production, the lack of power also influences the access to water. In 2018, only 12.93% [1] of the population had access to the electricity, and 72% [1] of that rate is from the population of Niamey, the capital city. The rural population, which represents 80% [1] of the population, has an access rate to the electricity of 3.14% [1] in 2016.

In these conditions, in rural areas it is difficult to access medical attention, mostly when it comes to vaccines and preservation of medicines that require a certain temperature. Since the electricity in those areas is not accessible, to extend the medical care to the furthest village, we should be able to conserve the medicines, vaccines, and other supplies under the best conditions possible. The use of generators would be quasi impossible due to the cost and availability of the fuel.

Solar energy could be the solution to the problem in a world where the research of new eco-friendly energy sources is the focus. The solar energy is a very promising type of energy to be exploited in the country. The average time of irradiance is of 9 hours per day in the capital city in 2019. The irradiance is in between 5.1 kWh/m2 and 6.3 kWh/m2 [2].

The solar energy can be used as a stand-alone power for a DC refrigerator in order to keep the vaccine under a temperature range of 2 ℃ to 8 ℃, which is within the standard of the world health organization (WHO). This temperature range is suitable for most of recently-developed Covid-19 vaccines (i.e., AstraZeneca, Janssen, Sinovac and Novavax), excepting that BioNTech require cold storage at -70°C.

A solar-powered refrigerator is a refrigerator that is powered by solar energy. The system can either use a photovoltaic (PV) or a thermal energy module. This type of refrigerator is used to keep perishables good in places where electricity is not available or to reduce the uses of fossil fuels. The solar powered refrigerator can be both used in houses or in the medical field. Vaccines need to be kept under some conditions for them not to turn bad. In some countries where the electricity is neither available nor reliable, the solar refrigerator comes as the best solution.

PV panel have already been used to power refrigerators destined to vaccines storage. Nevertheless, even if this type of system is the best answer for an access of the rural areas to the vaccines and medicines, its implementation and use is challenging, especially in terms of making an important investment at once. Also, the PV panel efficiency is affected by the sun. In a country like Niger, where the temperature reaches 45 under shade, the efficiency of the panel can reach it lowest and the panel can deteriorate quickly. As it was demonstrated, adding a thermoelectric generator (TEG) to a PV module to create a PV-TEG hybrid is a good way to improve the overall efficiency.

The idea would be to implement the hybrid in the back of the PV panel to have an PV-TEG hybrid refrigerator system. The PV-TEG hybrid has a higher efficiency than the PV panel alone. The increase of the efficiency means that the hybrid produces more power output than the PV stand alone. This increase in power means that more energy could be

saved by the battery, thus increasing the autonomy of the refrigerator in case of lack of irradiance or a low production of power due to cloudy days. Also, due to the fact the power output of the hybrid is higher, a smaller PV panel could be used compare to a PV stand-alone powered refrigerator. The reduction in the size of the PV panel will lead to a reduction in the overall size of the system.

All in all, this research can serve as a support for others studies in the improvement of the efficiency of PV systems, but also lead the way for more investigation, application and improvement of PV module in Niger.

2. Working principle of the system

A PV refrigerator is basically a refrigerator which is powered by a PV panel. The PV panel produces the electricity necessary for the refrigerator to function. The main important thing is to make sure that the refrigerator and the PV array the electrical characteristics are a match. The PV array should be able to cover the need in voltage and electric current of the refrigerator. These values are usually given by the manufacturers for both modules.

The solar refrigerator uses a PV-TEG hybrid to collect and transform the sun into electricity and batteries to store energy, a battery charge regulator, and a controller.

The hybrid should preferably be able to provide more than the power necessary to run your refrigerator. This should ensure that your refrigerator will not have less than

the required power for it to function.

The refrigerator part works as a normal refrigerator powered with fuel-based electricity. Nevertheless, it has a higher insulation around the storage place.

Batteries are used to store the extra energy that is not used by the refrigerator. This energy will be used to keep the vaccines cool when the sun will not be available: night-time or cloudy days. The battery will allow us to provide our refrigerator with stable power. Depending on the batteries used, the system could keep keeping cool for five days in the absence of sun. Mostly a lead battery with a long life and a deep cycle are chosen. The battery characteristics are given by its voltage and ampere-hours. The latter allow you to know how much current is used through a certain amount of time. For example, a 50 amp-hour can supply a current of 2 A for a duration of 25 hours. Thus, choosing the best battery for your refrigerator the ampere needed by the latter and the autonomy you would expect your system to have.

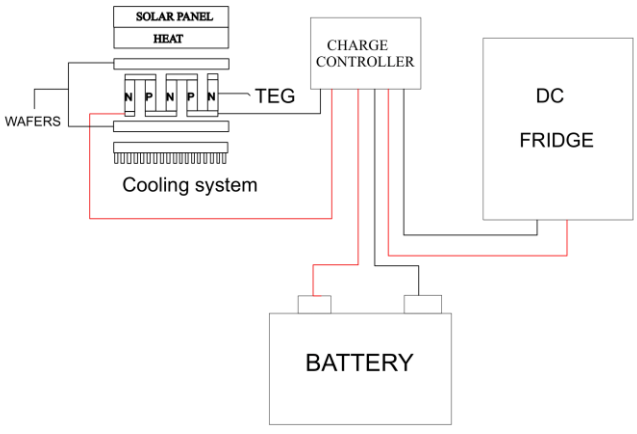

Figure 1. Simple schematic of a DC fridge powered by a PV/TEG hybrid

Charge regulator are not only used to control the current and the power delivered to the refrigerator in order not only

to exceed its tolerated range but also to avoid overcharging the battery. The power output of the PV panel's output changes throughout the day because of different factors such as the temperature and irradiation. These changes can damage your system if not taken care and regulated. A charge regulator allows you to control these fluctuations and thus to protect your system and allow it to work under the best conditions.

Where you need an inverter to supply a normal refrigerator with an AC standard current taking in account that the PV panel and battery power output are in DC mode, using a solar refrigerator which is DC powered, you can skip the inverter. The DC powered refrigerators are also built to work with solar energy which make them more efficient. This type of fridge is usually built to operate with 12/24v, which make them safer.

The PV-TEG module size and characteristic are chosen to meet the requirement of the system.

2.1. Previous work

The feasibility of using solar power for vaccines refrigeration is not a new idea, and many research and approaches were conducted on this issue.

A small refrigerator's performances were investigated by Alshqirate et al. [3]. The results were satisfying and gave acceptable performance results when deep discharge batteries were used. The solar module was able to produce enough power for the refrigerator to work without interruptions or delay. The used batteries had a good charging and discharging alternance capacity.

In 2012, Henriques [4] and his team implemented a mobile vaccine refrigerator with a parallel photovoltaic system in Kenya, an African country. They aimed to allow the transportation of vaccine without any lost in the vaccines number. Their implementation was based on a mobile system and another one which was fixed to the car used to transport them. The system used a low DC vapor compressor refrigerator, a PV panel, battery, an inverter, and a charge controller. The selected refrigerator was able to maintain the temperature between the requirement of 2 °C to 8 °C. The mobile system (fixed on the truck) could ensure an autonomy of 3 days and the stationary system (present at the located hospital) was able to go reach 10 days of autonomy.

It was proved that a PV system efficiency was not affected by the addition of load [5]. The efficiency of the PV system when connected to a fridge was not affected. Hence, it can be safe to combine the two system without having a drop in the efficiency of the PV panel.

A thermoelectric refrigerator was used as load for a PV system by Saidue et al. [6]. They used a PV system, a battery bank, a thermoelectric fridge, an inverter, and a charge controller. Their system was able to produce an autonomy of 3 days in case there is no sun available. They could keep the fridge temperature at a degree ranging from 1-7 °C and in average 4°C. The thermoelectric fridge was used thanks to its low starting power and because it is environmentally-friendly and it does not produce noise. Nevertheless, they report that this result can be improved by increasing the insulation of the fridge and improving the efficiency in term of heat exchange.

It was also proven by Modi et al. [7] that a normal domestic fridge can be powered by solar panel without any problem. The refrigerator worked normally as if it was connected to electricity grid. For the chosen refrigerator, they used a 140 Wp PV module and a battery bank composed of 2 batteries of 12 V-135A-H. However, they advised to choose a PV module with higher power output and a larger battery capacity in order to run the system sustainably. The forehand system was able to maintain the temperature to a range of 0-8°C, which is the range approved by World Health Organization for vaccine refrigeration.

The system discussed by Siddarth and his colleagues [8] consisted of a PV panel of 150 W with a voltage of 12 V, a battery of 75 Ah with a voltage of 12 V, which will allow a 50 W vapor compression refrigerator to be run smoothly. They demonstrated theoretically that their system has an autonomy of 12 hours. They also discussed that by introducing ice as a phase change material (PCM), they can reduce the size of the PV module, which will reduce the overall cost of the system.

The performance analysis of a vapor compression refrigerator and a vapor absorption refrigeration was conducted [9]. The two of them were powered and as a result they found that the vapor compressor refrigeration needs more time to cool the cabinet, but it does use less power than the vapor absorption refrigerator. The vapor absorption refrigeration coupled with the PV array is found to be the best system for rural areas to conserve medicine or food. The latter system could hold a temperature range of 6-10°C. Another positive point is that this system investment and maintenance cost less than the one with a vapor compressor, and also produce less noise.

A new system made of a portable refrigerator powered by PV array was presented in a study conducted by Buitendach et al [10] . The system was made of a well isolated refrigerator unit using an air thermoelectric cooling module, a control system for checking the temperature in and out of the cooler but also the voltage and capacitor of the battery. Their system was able to maintain a temperature range of 2-8 °C. This system can keep cool up to 250 vaccines and the temperature could be controlled with an accuracy of 1°C. In addition, the temperature, battery voltage and remaining capacity are being shown and it can keep the vaccines up to 3 days.

A solar powered refrigerator was assembled by Hossain [11] et al. using local materials in order to keep vaccine in a range of -15°C to 30°C. A solar panel was used along with an evaporator, a compressor, an inverter and an expansion valve. The system was tested under different weather temperature. They proved that it is compatible and the best solution in rural areas and refugees' camps, where the electricity is not sustainable.

A system [12] made of a solar powered DC refrigerator, a microcontroller to monitor the temperature, two PV panel connected in parallel was implemented. Their experiment showed that this type of refrigerator can be powered by using renewable energy, in this case solar energy. A DC refrigerator needs less power leading to the minimization of the loss. This will allow to reduce the cost and make the system more affordable to install in countries under development.

An experiment was conducted in Marrakesh, Morocco making in a PV powered refrigerator system under temperature and irradiance recorded trough winter, spring, and summertime. The PV module used a maximum power point tracking controller to produce the maximum power possible, a battery which was used along with Luenberger charge estimation, a converter, and a refrigerator. These components were chosen taking in account that the system should be light, strong and be the less expensive as much as possible. This system proposed by Doubabi et al. [13] is found to be compatible for keeping vaccines under a 4°C temperature, which meet the requirement of world health organization (WHO) for the storage of vaccines. The system could keep the vaccine cool up to 15 hours.

The superiority of the efficiency of the hybrid compared to the efficiency of the PV stand alone was demonstrated by many researchers. The TEG would use the extra heat of the PV cell to create electricity, thereby increasing the efficiency of the PV panel. The use of a thermoelectric generator with a dye sensitized solar cell (DSSC) get the efficiency goes from 9.39% to 13.8% [14]. Many types of solar cells were tested with a TEG, it was found that the copper indium gallium selenide photovoltaic has shown the highest efficiency, but the cost of the solar cell make its use difficult [15]. Beeri et al. [16] found that the hybrid made of a multi junction PV and TEG gave an efficiency of

32% and they predicted that in the future, this efficiency could reach 50%. Also introducing a PCM into the PV-TEG showed a good improvement in the efficiency [17]. Dallan's team [18] proved that indeed the addition of the TEG to the PV panel is beneficial and the electric efficiency could be increased to 39%; however, a drawback system is needed to counter the reduction of the fill factor. A rise of 3% in the efficiency of the system made of a concentrating photovoltaic and a TEG was reached [19]. A roof integrated PV-TEG system presented a 23% efficiency [20]. An experiment was conducted not only for 24h but also on the long term, (one year) [21]. It was found that the temperature of the PV-TEG under the maximum irradiance was of 44.2°C while the temperature of the stand alone was of 57.1°C. A rise of 1.65 % and 1.72% respectively in the electrical and energy efficiency for the PV-TEG compared to the stand alone. The use of a PCM and TE at the back of the solar cell allowed Luo et al.[22] to reduce the cell temperature from 79.72°C to 57.39 °C. The cell temperature of the simple PV-TE was of 73.62°C. The efficiency of the PV-PCM-TE module had an increase of 17.57% compared to the PV stand alone and a 2.37% increase compared to the PV-TE module. The efficiency increase was more considerable in summer (3.53 %) than in winter (0.6%).

3. Mathematical modelling of a PV-TEG

A PV-TEG is made of a PV module and TEG. The PV module uses the sunlight to produce electricity. However, the more the panel gets heated, the less it is efficient. The heat could reduce the efficiency of the PV panel by 25%. A TEG uses temperature difference between its two side (hot and cold side) to create electricity. The TEG is joined to the back of the PV module to use the heating of the PV panel to create more electricity. The PV temperature will be considered as the temperature of the hot plate of the TEG. Thus, the hybrid will present a better efficiency than the stand-alone PV panel.

The temperature of the PV device is given by:

$$T_{PV} = T_a + c.G \tag{1}$$

$$c = (T_{noct} - 20)/800 \tag{2}$$

where T_a represents the surrounding temperature, G irradiance of the sun and C is a parameter that differ from one installation to another and it is calculated using the capacity of the heat exchange between the PV cell and the surrounding.

The efficiency of the PV module is given by

$$\eta_{PV} = \eta_{PVref}.\left[1 - \beta.\left(T_{PV} - T_{ref}\right)\right] \tag{3}$$

where β represents the coefficient of the temperature efficicency, η_{PVref} represent the efficiency of the device under the standard test conditions, T_{ref} represent the temperature reference, usually taken as 25°C.

The equation of the power output of the is:

$$P_{PV} = \eta_{PV}.G.A \tag{4}$$

A is the area of the cell that the irradiation is falling on

The power output of a TEG is given by:

$$P_{TEG} = Q_{hs} - Q_{cs} \tag{5}$$

$$Q_{hs} = n * (S\,.I.T_{hs} + \overline{K}.(T_{hs} - T_{cs}) - (1/2)\,.R_{te}.I^2) \tag{6}$$

$$Q_{cs} = n * (S.I.T_{cs} + \overline{K}\,.(T_{hs} - T_{cs}) + (1/2)\,.R_{te}.I^2) \tag{7}$$

$$P_{TEG} = n(S.I.(\,T_{hs} - T_{cs}) - R_{te}.I^2) \tag{8}$$

$$I = S.(T_{hs} - T_{cs})/R_{te} + R_L \tag{9}$$

Where R_L is the load resistance

For matching purpose, let's consider that R_{te} and R_e are sharing the same value.

The efficiency of the TEG becomes:

$$\eta_{TEG} = P_{TEG}/Q_{hs} \tag{10}$$

The power of the hybrid is given by:

$$P_{HY} = P_{PV} + P_{TEG} \tag{11}$$

Its efficiency is:

$$\eta_{HY} = P_{HY}/G.A \tag{12}$$

$$\eta_{HY} = \eta_{TEG} + \eta_{PV} \tag{13}$$

For our simulation, we used the mono-crystalline Silicon PV panel and TEG specified below

Table 1. PV specifications

Size	$40 * 40\ mm^2$
Number of couples thermoelement	128
Thermoelement cross section(W * D)	$1{,}4 * 1{,}4\ mm^2$
Maximum temperature	320 C
L_{TE} (length of thermoelement) (mm)	1,6
$S\ \ (^{\mu V}/_{K})$	282
$\overline{K}$	1.20 W/(m·K)
Number of TEG used in series	615

Table 2. TEG's specifications

Size	1480mm*665mm*35mm
Maximum power (Pmax)	150W
Optimum operating voltage (Vmp)	17.2V
Optimum operating current(Imp)	8.72A
Open-circuit voltage(Voc)	21.6V
Short-circuit current(Isc)	9.92A
Isc temperature coefficient	(0.065 ±0.015)%/℃
Voc temperature coefficient	-(80 ±10)mV/℃
Peak power temperature coefficient	-(0.5 ±0.05)%/℃
Operating temperature	-40℃ to 85℃

Table 3. Refrigerator's specification

Gross / Net volume (l)	52 / 45
Set temperature (preset)	+5°C
Set temperature (setting range) can be adjusted in steps of 0.1°C	+4°C to +15°C
Temperature cold / warm alarm limit	+3°C / +7°C
Hold over time (+5°C to +10°C)	1 h 15
Climate class (ambient temperature range)SN	(+10°C to +32°C)
Defrosting technique	Natural
Refrigerant type	R600a
External dimensions H x W x D (mm)	670 x 495 x 575
Inner dimensions H x W x D (mm)	470 x 375 x 350
Supply voltage (V)	220-240
Frequency (Hz)	50/60
Power (W)	100
Energy consumption (kWh/24h)	0.42/0.45
Heat emission (Kcal/h)	12
Compressor running time (%)	32
Noise level (dB(A)) (at 1m height & 1m distance)	35/36

4. Results and Discussion

In order to conduct our research, we implemented our model using Matlab. Our calculations were conducted using average data of the months of January and September. A specific day, 7th May was chosen because it represented the hottest day in the country during the year 2019. The data used were the irradiance and temperature collected from the Meteorology Center of Niger, nevertheless the irradiance for the 7th May were accordingly approximated, and for the other months the daily average data were used. The figures 2 and 3 given below show corresponding irradiance and

temperature data.

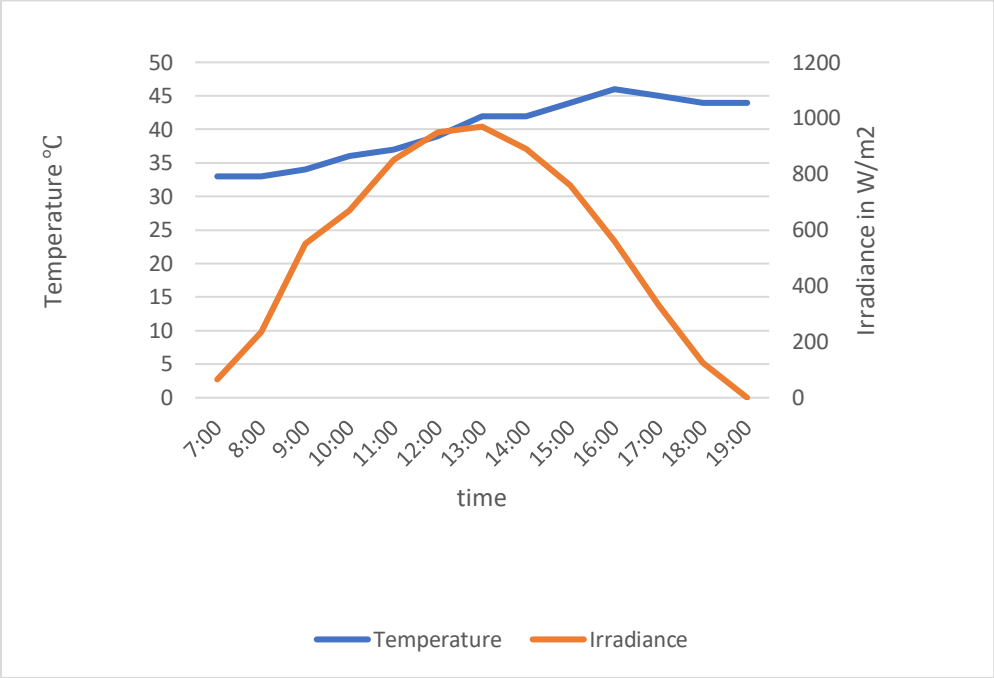

Figure 2. Curves of the average irradiance and temperature on 7th May 2019 in Niamey

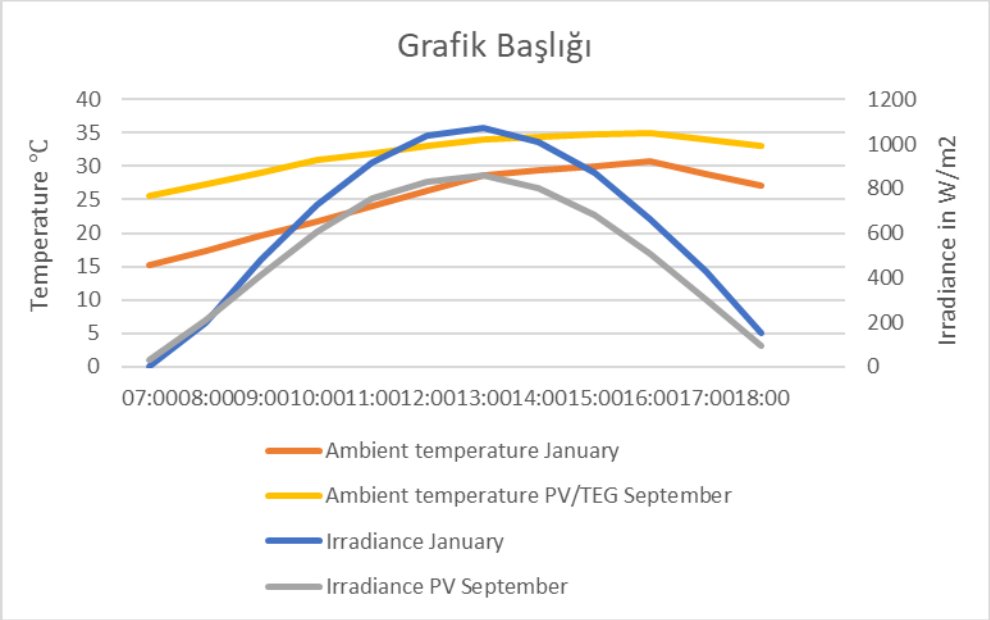

Figure 3. Curves of the average temperature and irradiance in January and September 2019 in Niamey

From the figures 4, 5, 6 and 7 given below we can see the power output and efficiency of a PV panel when used alone and when used with a TEG. The PV-TEG has shown a greater performance than the stand alone and this regardless of the day.

For example, on the 7th of May, the hybrid showed a peak of 186.9 W while at the same point the stand-alone's power was of 117.13W (see Fig.4). In addition, at the same date, when the efficiency of the hybrid is of 19.62% , at the same point the stand alone presented an efficiency of 12.24% (see Fig.6).

The results obtained with the data in January and September are here to correlate and support the results obtained the 7th May. We can see on the curves a good improvement in the total power output and efficiency of the PV coupled

with the TEG than when the PV is used alone. The highest power output in January is of 196.69 W for the hybrid against a 134.79 W (Fig. 5) for the stand alone in January, while the power was of a value of 153.224 W for the hybrid and 108.79 W in September (Fig. 5) . The efficiency went up to a highest value of 18.69% for the hybrid from 12.81 % (Fig. 7) for the stand alone under January's conditions which is a rise of 5.88%. Under September's conditions, a 18.29 % for the hybrid and an efficiency of 13.09% for the stand alone which is a total rise of 5.2% (Fig. 7).

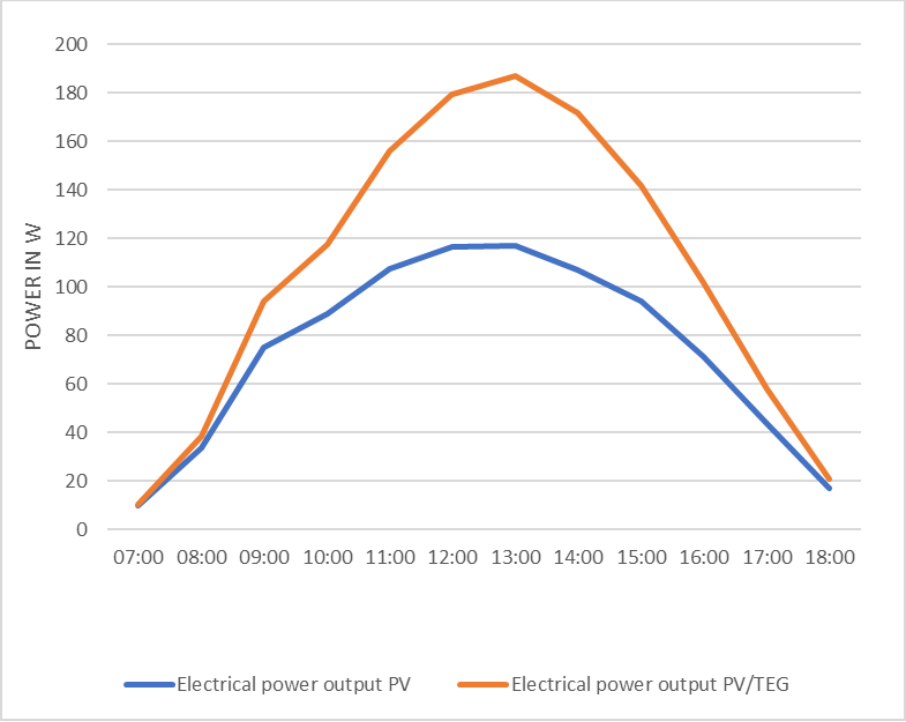

Figure 4. PV and PV-TEG power output in May 2019

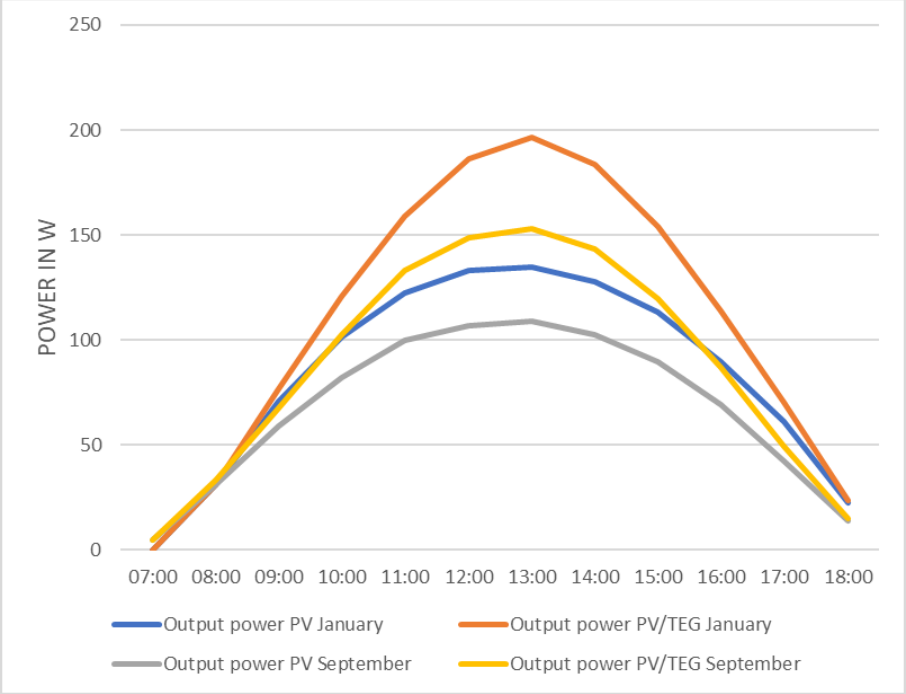

Figure 5. PV and PV-TEG power output in January and September 2019

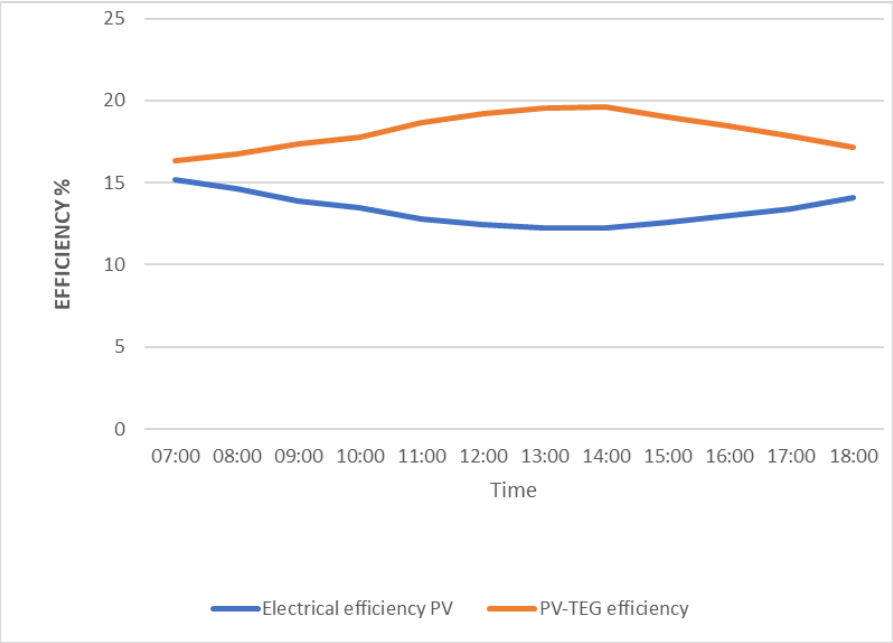

Figure 6. Efficiency of PV panel and PV/TEG on 7th May 2019

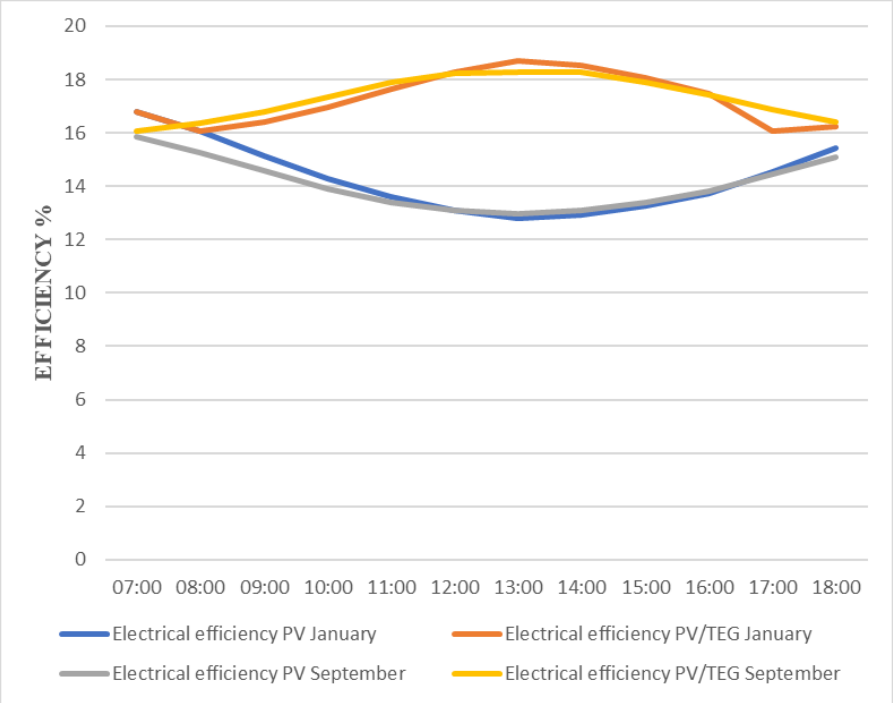

Figure 7. Efficiency of PV panel and PV/TEG in January and September 2019

A medical refrigerator manufactured by B-medical systems is used. Its technical specifications are given in Table 3. A refrigerator with a power consumption of 30 W is used with our hybrid and stand-alone system designs. For the 12 hours of irradiance throughout the day, a total of 882.56 Wh energy was produced by the stand-alone PV versus 1277.53 Wh for the hybrid. The same refrigerator with a power consumption of 30 Watt and a capacity of 52 L is used with these two different systems. Taking in account that the fridge consumption is 450 Wh/day, we would be able to store approximatively up to 827.53 Wh which would give us nearly 44 hours of autonomy, while with the stand-alone PV panel, we would be able to only store 432.55 Wh, which corresponds to 23 hours of autonomy. The autonomy provided by the hybrid powered refrigerator is almost the double of that provided by the PV stand-alone system.

The table 4 below is a recapitulative of the produced, stored power and the autonomy hours under the three different conditions. It can be seen from these results that the use of a hybrid is an important asset to be considered in vaccine refrigeration.

Table 4. Recapitulation of power and autonomy of the two different systems in January

	January		**7th May**		**September**	
	PV power	**Hybrid power**	**PV power**	**Hybrid power**	**PV power**	**Hybrid power**
Total output power	1007.93	1315.87	882.558	1277.53	810	1058.59
Saved output power	557.93	865.87	432.558	827.53	360	608.59
Days coverage	1.23	1.92	0.96	1.83	0.8	1.35
Autonomy hours	29.75	46.08	23.04	44.13	19.2	32.4

5. Concluding Remarks

The access to electricity is a real challenge in the rural areas in Niger, not to say in the whole country. The access rate to electricity is 12.93% in the whole country, and only 3.14 % of the rural population has access to the on-grid electricity. With most of the electricity imported from Nigeria, besides the numerous power sources available in the country, to extend medical care to the rural areas, solutions must be found. Indeed, vaccines and medicines need to be well stored for them not to perish. The potential of the country in solar energy is an interesting answer to be investigated. The country has a high irradiance and has an average of 9 hours of irradiance per day. Solar energy could be used to power the refrigerators destined to the storage of the vaccines and medicine.

To achieve better performance of such system solar powered fridge, the use of a Hybrid PV-TEG is considered. It was shown that the efficiency and power output of the hybrid is superior to the ones of the stand-alone PV panel. The efficiency of the hybrid was found to be 7.38 % higher than the stand-alone efficiency at the moment the cell temperature reached the highest point. That increase in the efficiency of the hybrid, will allow to create more power to be stored in batteries for times when sun will not be available. Thus allowing a rise in the autonomy of the solar powered refrigerator. For our designed system, the autonomy procured by the hybrid is almost the double of the one provided by the PV stand alone for the same refrigerator. The use of hybrid can also allow to reduce the size of the PV panel necessary to power the system, thus reducing the size of the overall system.

Our work comes as a support to the already existing base affirming that a thermoelectric coupled to a PV module is a very good mean to reduce the heating and hence improve the efficiency. This work is a first conducted under the Niger weather, which is in real need of an energetic solution.

We believe that PV-TEG system can be a good solution for sustainable cold chains for equitable delivery and use of Covid-19 in Niger and in most of the sun-rich African countries. The WHO can arrange such a campaign call for G7 or G20 countries to afford, provide and organize delivery of large amount PV-TEG refrigerator systems into the countries in need.

References

[1] L'ENERGIE, R.D.N.M.D., *PROSPECTUS D'INVESTISSEMENT DE L'ENERGİE DURABLE POUR TOUS (SEforALL) DU NIGER*. 2019.

[2] Dankassoua, M. and S. Yahaya, *Evaluation of Solar Potential at Niamey: Study Data of Insolation from 2015 and 2016.* Smart Grid and Renewable Energy, 2017. 8(12): p. 394-411.

[3] Alshqirate, A., M. Tarawneh, and M. Hammad, *Performance study of a domestic refrigerator powered by a photovoltaic generator.* Applied Solar Energy, 2015. 51(1): p. 1-5.

[4] Henriques, J.J., et al. *Implementation of a Mobile Vaccine Refrigerator with Parallel Photovoltaic Power Systems.* in *2012 IEEE Global Humanitarian Technology Conference.* 2012. IEEE.

[5] Deshmukh, S. and S. Kalbande, *Performance evaluation of photovoltaic system designed for DC refrigerator.* Int J Sci Res, 2015. 4(2): p. 18-23.

[6] Saidur, R., et al., *Performance investigation of a solar powered thermoelectric refrigerator.* International journal of mechanical and materials engineering, 2008. 3(1): p. 7-16.

[7] Modi, A., et al., *Performance analysis of a solar photovoltaic operated domestic refrigerator.* Applied Energy, 2009. 86(12): p. 2583-2591.

[8] Siddharth, R., et al. *Design and Simulation of a Vapour Compression Refrigeration System Using Phase Change Material. in MATEC Web of Conferences.* 2018. EDP Sciences.

[9] Sharma, N.K., et al., *Performance Analysis of Vapour Compression and Vapour Absorption Refrigeration Units Working on Photovoltaic Power Supply.* International Journal of Renewable Energy Research (IJRER), 2016. 6(2): p. 455-464.

[10] Buitendach, H., I.N. Jiya, and R. Gouws, *Solar powered peltier cooling storage for vaccines in rural areas.* 2019.

[11] Hossain, A., et al. *Low Power Consuming Solar Assisted Vapor Compression Refrigerator To Preserve Emergency Medicines And Vaccines In Rural Areas. in 2019 1st International Conference on Advances in Science, Engineering and Robotics Technology (ICASERT).* 2019. IEEE.

[12] Tsado, J., et al. *Solar powered DC refrigerator with a monitoring and control system.* in 2018 IEEE PES/IAS PowerAfrica. 2018. IEEE.

[13] Doubabi, H., et al., *Modeling and design of a solar-powered refrigerator for vaccines transportation in remote regions.* Journal of Solar Energy Engineering, 2020. 142(4).

[14] Wang, N., et al., *A novel high-performance photovoltaic–thermoelectric hybrid device.* Energy & Environmental Science, 2011. 4(9): p. 3676-3679.

[15] Zhang, J., Y. Xuan, and L. Yang, *Performance estimation of photovoltaic–thermoelectric hybrid systems.* Energy, 2014. 78: p. 895-903.

[16] Beeri, O., et al., *Hybrid photovoltaic-thermoelectric system for concentrated solar energy conversion: Experimental realization and modeling.* Journal of Applied Physics, 2015. 118(11): p. 115104.

[17] Cui, T., Y. Xuan, and Q. Li, *Design of a novel concentrating photovoltaic–thermoelectric system incorporated with phase change materials.* Energy Conversion and Management, 2016. 112: p. 49-60.

[18] Dallan, B.S., J. Schumann, and F.J. Lesage, *Performance evaluation of a photoelectric–thermoelectric cogeneration hybrid system.* Solar Energy, 2015. 118: p. 276-285.

[19] Kil, T.-H., et al., *A highly-efficient, concentrating-photovoltaic/thermoelectric hybrid generator.* Nano energy, 2017. 37: p. 242-247.

[20] Van Sark, W., *Feasibility of photovoltaic–thermoelectric hybrid modules.* Applied Energy, 2011. 88(8): p. 2785-2790.

[21] Fini, M.A., D. Gharapetian, and M. Asgari, *Efficiency improvement of hybrid PV-TEG system based on an energy, exergy, energy-economic and environmental analysis; experimental, mathematical and numerical approaches.* Energy Conversion and Management, 2022. 265: p. 115767.

[22] Luo, Z., et al., *Simulation study on performance of PV-PCM-TE system for year-round analysis.* Renewable Energy, 2022. 195: p. 263-273.

J Inno Sci Eng,2023, 7(1):88-105
http://doi.org/10.38088/jise.1206920

Research Article

Remaining Useful Life Estimation via Cascaded Self-Attention and ResNet Models

Adem Avci [1*], Nurettin Acir [2]

[1] *Bursa Technical University, Department of Electrical and Electronics Engineering, Bursa, Turkey*
[2] *National Defence University, Turkish Air Force Academy, Department of Electronics Engineering, Istanbul, Turkey*

Cite this paper as:
Avci, A. and Acir, N. (2023). *Remaining Useful Life Estimation via Cascaded Self-Attention and ResNet Models* 7(1):88-105.

*Corresponding author: Adem AVCI
E-mail: adem.avci@btu.edu.tr

Received Date: 18/11/2022
Accepted Date: 23/02/2023

Abstract

Prognostics and Health Management occupy an important place in modern industrial maintenance to increase the reliability of systems. Determining the Remaining Useful Life of the system or its parts is vital accurately to maintaining critical parts of the system and successful prognostics and health management. This study proposes a data-based Remaining Useful Life prediction method with a network consisting of a cascade-connected Self-Attention and Residual Network layer. The network is fed by multiple sensor signals to monitor the aero-engines. The proposed model contains four main parts: The Gaussian Noise Layer, the Self-Attention Layer, the Residual Network Layer, and the layer to estimate Remaining Useful Life. The model is created to be more robust and susceptible to noise using the Gaussian Noise Layer. The Self-Attention Layer focuses on crucial points through time. The Residual Network Layer uses feature extraction and makes the model more profound help of the skip connection. Finally, the Remaining Useful Life estimation is made using highly correlated features obtained from the fully connected layer and the output layer. In addition, a new loss function has been offered, similar to the evaluation metrics in the literature. With the proposed model and loss function, 11.017 and 12.629 in root mean square error, 157.19 and 218.6 in score function are obtained in the FD001 and FD003, respectively. The superior performance of these results on the C-MAPSS dataset is demonstrated by comparing the other state-of-the-art methods in the literature.

Keywords: Remaining useful life, Self-attention, Prognostics and health management, Deep learning, Residual Layer

1. Introduction

As the complexity of systems increases in modern industry, maintenance and prognostic become more crucial. With the developments in sensor technologies, computing systems, and learning algorithms, Prognostic and Health Management (PHM) put to use in various areas such as aero-engines [1], electric motors [2], battery systems [3], and nuclear plants [4]. PHM aims to monitor systems and their parts with the help of sensor data and estimate the degradation of this systems. Also, PHM diagnoses abnormal activity, detects possible failures, estimates machines' state of health, and predicts the Remaining Useful Life (RUL) of the system or its equipment. Hence, in industry, maintenance schedules can be planned effectively, unnecessary parts replacement during maintenance can be avoided, and maintenance costs are reduced. PHM can prevent catastrophic failures by estimating the current and future states of systems and, with this, improve the reliability and performance of systems. RUL can show the remaining life with time cycles or hours according to the area studied. RUL is defined in the literature as the time from the current time to time occurred failure [5].

The RUL estimation has generally been categorized in recent PHM studies with three different approaches [6]. These are model-based approach, data-driven approach, and hybrid approach. Life estimation is being studied by creating mathematical models with prior knowledge of the system examined in model-based PHM approaches [7]. The studies in the literature identify degradation in systems and developed the model-based approach such as Paris's law [8] and exponential models [9]. However, as the system's complexity increases, the performance of these mathematical models in life estimation problems begins to decline. In addition, deviations may occur in the models created as the operating conditions of systems change.

On the other hand, data-driven approaches include the detection of errors with the help of sensors on the systems and estimating RUL. Big data collected from sensors provides the development of degradation models. Machine learning and deep learning structures, which have developed in recent decades, can show more successfully the status of a machine's health together with big data. Hybrid models aim to achieve better results by eliminating the deficiencies of model-based and data-driven approaches. However, unlike the data-based approach, particular expertise is required to develop and integrate a physical system into the degradation model. The following subsection provides a brief overview of research studies using the data-driven approach to estimate RUL.

1.1. Literature Review

In the literature, better predictions are made using machine learning and deep learning algorithms in data-driven approaches. Each data point is committed independently in machine learning approaches, and estimations are performed. In this context, studies were carried out with Support Vector Regression (SVR) [10], Relevance Vector Regression (RVR) [10], Random Forest (RF) [11], and similar algorithms. In addition, the data points were evaluated independently in the Multilayer Perceptron (MLP) algorithm, and RUL estimation was made [10]. With the performance of deep learning algorithms in the last decades, it has been frequently used in RUL estimation. Among these algorithms, Convolutional Neural Networks (CNN), Recurrent Neural Networks (RNN), and their derivatives produced successful results in RUL estimation. Babu et al. proposed a two-dimensional deep CNN to estimate aero-engines RUL [10]. Firstly, sensor signals were normalized, and the time windowing method was employed to train deep CNN (DCNN). Also, their models included two convolutional and average pooling layers,

then used a Fully Connected (FC) layer. Automatic feature extraction has been provided with the convolutional layer, and RUL estimation has been made. In another study, Li et al. offered a novel DCNN [12]. They set the C-MAPSS dataset as two-dimensional inputs with a time windowing pre-processing technique. They employed five convolutional layers in their model, each of which is made up of a 1-D filter. The dropout technique was used to avoid overfitting problems in their model.

Since the RUL dataset is a time sequence, it has a suitable structure for dynamic networks. Zheng et al. suggested a dynamic neural network consisting of Long Short-Term Memory (LSTM) layers [13]. Their model included two LSTM layers, two FC layers, and a neuron as the output layer. Then, they tested their networks with a different number of LSTM cells in LSTM layers and a different number of neurons in FC layers. LSTM layers were able to extract complex features in the time domain and thus obtained better Root Mean Square Error (RMSE) values compared to RNN. Wu et al. wielded a vanilla LSTM network in their work [14]. Also, new features were extracted from operating conditions values by the dynamic difference technique. These features were used with chosen sensor signals that change with time. In their work, Yu et al. accomplished RUL prediction in two stages [15]. First, the dataset is processed using selecting sensor signals, the normalization process, and the time windowing technique, which has different window lengths. Then, the machine's Health Index (HI) is estimated with a Bi-directional LSTM(BLSTM)-based autoencoder model and linear regression. Finally, RUL values are mapped with estimated HI. In another study, Wang et al. propounded a BLSTM-based network [16]. Their model included two BLSTM layers, 2 FC layers, and the output layer, which has a neuron. Palazuelos et al. proposed a novel capsule neural network that Hinton et al. offered to overcome the shortcomings of CNN [17]. The capsule structure was first used for the C-MAPSS dataset in this study.

Some studies use the feature extraction attributes of LSTM and CNN networks together. Al-Dulaimi et al. wielded LSTM and CNN structures as parallel branches in their study [18]. Thus, capturing the CNN structure's spatial and the LSTM structure's temporal features are considered together. Al-Dulaimi et al. added gaussian noise layers to parallel network structure in their study [19]. The LSTM path in the previous work was changed with the BLSTM path that added noise layers. Thus, they obtained better results in RUL estimation. J. Li et al. have adopted the parallel network structure in their study [20]. The parallel branches consisted of Convolution layers and LSTM layers. Summing the outputs of these paths is connected to the LSTM layer, FC layer, and output layer, respectively. Song et al. proposed a novel neural network in series connection [21]. Their model had two BLSTM layers and two FC layers stacked after the autoencoder layer. The feature extraction was made by autoencoder, and long-range dependencies of temporal features were utilized with BLSTM. The dropout technique was used as regularization. Ragab et al. offered autoencoder-based LSTM [22]. In the decoder part of their model was placed attention mechanism. A path to reconstruct the input data and another to estimate RUL was offered. In model training, summing reconstruction loss and RUL loss were used. In their model, Liu et al. wielded a feature extraction layer consisting of a channel attention mechanism and a transformer with temporal attention [23]. Tan et al. proposed a novel network consisting of an attention layer [24]. They used the attention layer after four Convolution layers and connected the FC layer and output layer. Two different lengths of the time window are used in their study. In [25], on the other hand, LSTM and self-attention structure were used together. With the self-attention structure, it was ensured to focus on the critical points in the data, and RUL estimation was made by transferring the information to the following layers with the LSTM layers.

1.2. Contributions

It is made to estimate RUL on the time series like aero-engines data in this study. The time series data were considered with different network structures in the literature. RNN, LSTM, and Gated Recurrent Unit (GRU) structures were used in these studies. Against previous works, these networks fetched good results due to dynamic structure. However, there was no further improvement in results due to limited and noisy data. The Self-Attention Layer has been added to the models, resulting in better results. In addition, the formation of more robust structures in the models was provided with different techniques. Although Residual Network (ResNet) layers have been used in different studies, it has been observed that it causes overfitting in the datasets in the experiments. In the previously mentioned literature, they have obtained state-of-the-art results by using each in different models. However, robust, deep structures focused on relevant points in the time domain have not been used together. Also, this study determined this gap in the literature, and network models were developed on better estimations.

The main contribution of this study to the literature is as follows:

1) With the Self-Attention layer, it has been ensured to focus on the crucial points in the time series. Thus, the proposed model detected the vital points for a good estimation of time series data in each sensor signal.
2) By adding the noise layer, it is planned that the proposed model will operate more robustly and make more accurate estimations. The Gaussian Noise layer is just used in the training process. Moreover, the model has become more robust in the noise layer.
3) Using the ResNet structure ensures that the backpropagation can reach the first layer. Thus, the network structure can be made deeper.
4) Also, the Convolution layer is used with the stride technique instead of the pooling layer to avoid losing information. Thus, while feature extraction was performed, dimension reduction was also made together.

Self-Attention and ResNet structure were wielded as cascaded, and better results were obtained with estimation performance compared to other studies. However, the proposed model has limitations. One of them, the model input, is created with a constant input shape. Also, the dataset used in the study has sub-datasets, and fixed input data is not created with the same pre-processing steps. For this reason, sub-datasets with the same input form are used. In addition, model structure, hyperparameters, and weighting coefficients should be changed to obtain better results in each sub-dataset.

The rest of this study is organized as follows: In the second part, the offered Cascaded Self-Attention ResNet Network (CSARN) model and the methods used in the model are explained. In addition, the C-MAPSS dataset on which the proposed model is tested is detailed, and the pre-processing steps for RUL estimation are explained. In the third part, the experimental work carried out is explained. The results obtained with the experimental study are reported and graphed. It is also compared with other studies in the literature. The last part summarizes all the work, and information about future work is given.

2. Materials and Methods

This section presents the proposed model for RUL estimation and the studied dataset. Within the scope of this

study, a self-attention-based model is created. Since the dataset has a noisy structure, a Gaussian Noise layer has been added to the beginning of the model. Then, it is transferred to the following layers by detecting the most critical points in the time domain with the Self-Attention layer. Both automatic feature extraction is provided with the ResNet layers, and training is improved with the skip connection structure. An FC structure is used in the last layers, and RUL estimation is made with the last layer.

The C-MAPSS dataset produced by NASA Ames Research Lab is introduced. The sensor information that they contain in the dataset is given in detail. The pre-processing steps on the dataset are explained before training the proposed model. The selection of the sensors in the dataset, the normalization process, the time windowing technique details applied to the dataset, and the target data prepared according to the degradation model are explained. Finally, the metrics to evaluate the predictions made on the test dataset with the trained model are presented.

2.1. Proposed Method

2.1.1. Self-Attention Module

CNN shows remarkable performance in automatic feature extraction. Convolution operation, by its nature, provides translational equivariance and translational invariance features in operations [26]. Convolution, introduced by LeCun et al. for the first time in neural networks, achieved great success, especially in image classification and object detection. By scanning with the filters created with fixed lengths on the input data, the features are automatically extracted for all the data. As we move from the first CNN layer to the last CNN layer in deep networks, the complexity of the extracted features increases and gets closer to the desired estimations. The translational equivariance feature of convolution operation provides valuable information in local data, but capturing global dependencies in time series signals is not feasible.

The Attention mechanism, developed and frequently used recently, shows a significant impact where it is used [27]. It was used in natural language processing (NLP) first and showed great success in its field. The Attention mechanism ensures that the models are focused on the critical regions in sequential data. Unlike the attention mechanism, the Self-Attention mechanism transfers the necessary information from a single content to the following layers. In the Self-Attention structure shown in Figure 1, a single content is entered into the block. With the help of this input data Convolution layer, three different contents are created, and the block output is focused on the most critical parts. Within the scope of this study, it was ensured that the Self-Attention mechanism was influential throughout the time domain in the dataset used. The crucial parts in the time domain are transferred to the following layers at the output of the block. By focusing on essential regions, regression performance would be improved with the help of Self-Attention mechanisms.

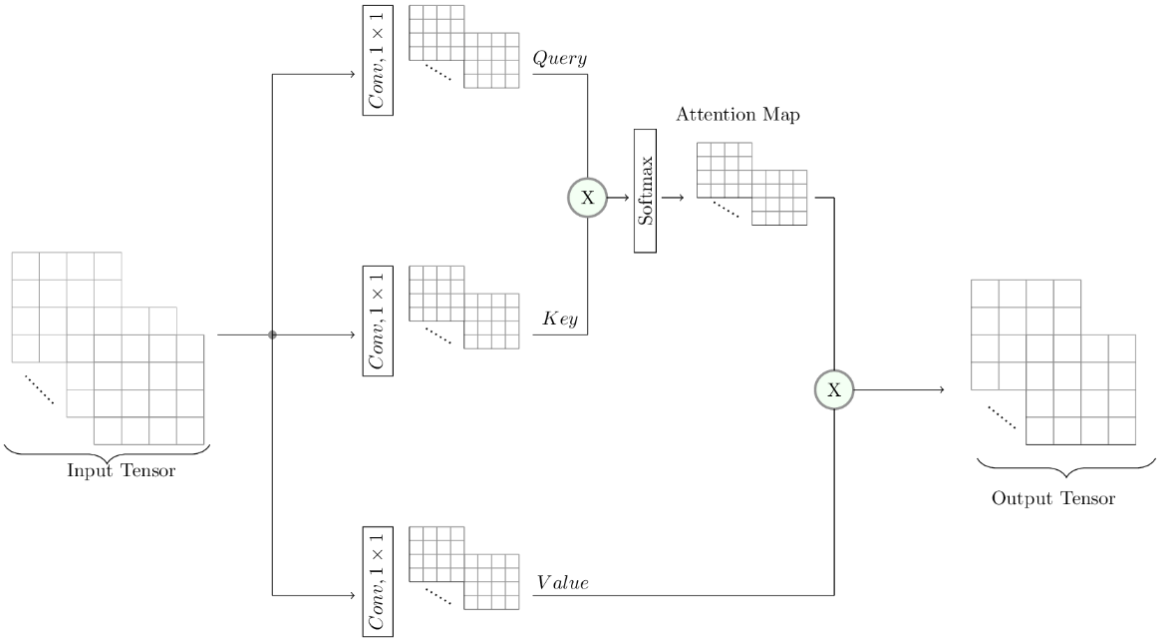

Figure 1. Self-Attention layer in the proposed model

The Self-Attention layer used in this study is shown in Figure 1. Input data is divided into three tensors with Convolution layers: Query, Key, and Value. The resulting Query and Key tensors are multiplied by the Hadamard product and passed through the softmax activation function across the time domain. Thus, it is ensured that it focuses on the most appropriate points in the time domain for our regression problem. Output data is procured by multiplying the same dimensional Value Tensor with the attention map. The equation expressing the Self-Attention layer is shown below [27].

$$A_M = softmax(Query, Key)Value \quad (1)$$

2.1.2. ResNet Module

More complex features are extracted as the network structure becomes deeper in deep learning models. Adding more layers increases the number of model parameters, but the models' performance is generally improved. However, vanishing/exploding gradient problems arise as the network structures get deep. In addition, while the model coefficients are updated with the backpropagation algorithm during the training, updating the first layers with deepening becomes more challenging. Residual Convolution Block has been proposed in the ResNet model to fix the reported update problem [28]. With this structure, it is aimed to spread the loss effect in the output layer to the first layers. The ResNet Block structure used in our study is shown in Figure 2. As shown in the structure, while feature extraction continues from one branch, a skip connection is established from the other branch. Thus, even if the network structure continues to deepen, the gradient effect is aimed at reaching the first layers through the second path.

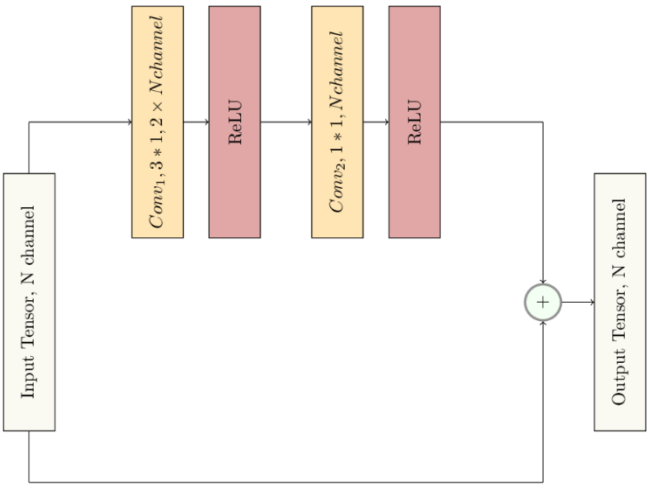

Figure 2. ResNet block in the proposed model

2.1.3. Cascade Self-Attention ResNet Network (CSARN)

Cascaded Self-Attention ResNet Network (CSARN) consists of four different layers connected in series. These are Convolution, Self-Attention, ResNet, and FC layers, respectively. The proposed model structure is shown in Figure 3. First, the Gaussian Noise layer, which has zero mean and 0.01 standard deviation, was added to the proposed model. This layer is only wielded during model training. Then, the Convolution layer with ten filters with a filter size of 11x1 is connected to the model in series. In addition, the number of filter numbers was kept constant for all Convolution layers, except the convolutional layer before the Flatten layer used in the model. After the first Convolution layer, the Self-Attention layer was added. Thus, it is ensured that the relevant points in the input data are focused and transferred to the subsequent layers. The proposed ResNet layer and the Convolution layer were added to the model twice after the Self-Attention layer. In the Convolution layer, size reduction was achieved by taking stride set 2 throughout the time domain.

Moreover, in this and the following Convolution layers, the filters are used with a filter size is 7x1. After the last Convolution layer, the structure is connected to the FC layers with the Flatten layer. There are dropout layers with a dropout rate of 0.3 between the FC1 and FC2 layers, as shown in Figure 3, and between the FC2 and FC3 layers. There have 140 and 90 neurons in the FC 2 and 3 layers, respectively. The FC layers are finally connected to the output layer with a single neuron. 'ReLu' is used as the activation function in all model layers. In addition, the regularization parameter in all layers in the model was set as 0.0002.

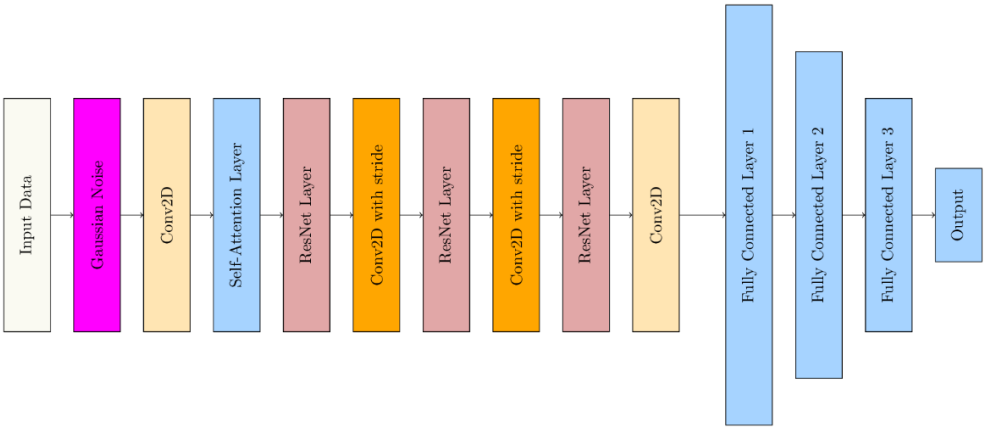

Figure 3. Proposed model for RUL prediction

2.2. Experimental Configuration

2.2.1. Dataset Description

In this paper, the proposed model is evaluated on NASA Commercial Modular Aero-Propulsion System Simulation (C-MAPSS) turbofan engine dataset [29]. This dataset contains synthetic data generated on MATLAB Simulink environment by NASA Ames Research Lab. The aero-engine model while creating the dataset is shown in Figure 4.

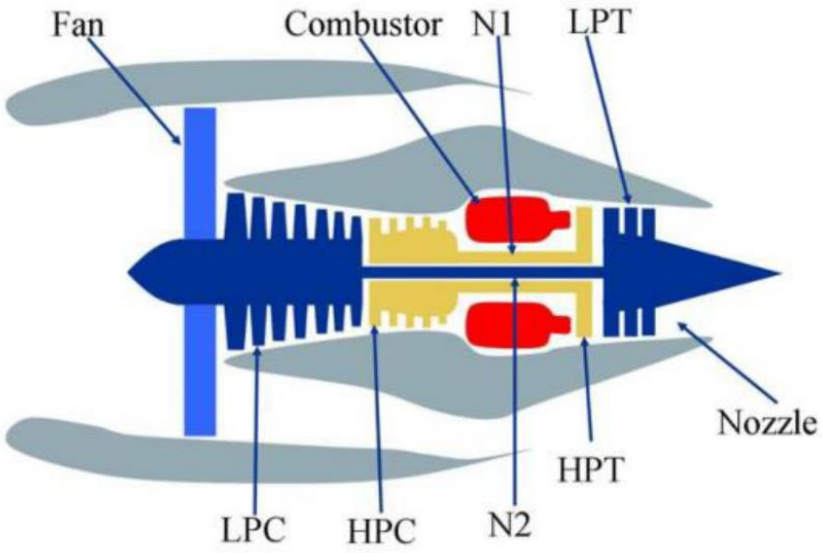

Figure 4. C-MAPSS turbofan engine [29]

The dataset consists of 4 sub-datasets, each with different conditions and failure modes. These sub-datasets were generated at six different operational conditions by operating the engines at altitudes between sea level and 40000 ft, in the speed range 0 to 0.84 Mach, and throttle resolver angle between 20 and 100. Also, RUL scenarios on the datasets were simulated on the deterioration of two of the engine's five rotating elements (Fan, LPC, HPC, HPT, and LPT) [29]. Input parameter values in each motor simulation in the dataset are changed to ensure that they have different RUL values. The engines in the training set were run to time that occurs break down. However, in the test dataset, the engines were run from the start to a specific time. The details of C-MAPSS are listed in Table 1.

Table 1. Details of the C-MAPSS dataset

Dataset	NASA C-MAPSS			
	FD001	FD002	FD003	FD004
Train sets	100	260	100	249
Test sets	100	259	100	248
Operating Conditions	1	6	1	5
Fault Conditions	HPC	HPC	HPC, Fan	HPC, Fan
Training Samples	20631	53759	24720	61249
Min/Max Cycles for Train set	128 / 362	128 / 378	145 / 525	128 / 543
Min/max cycles for Test set	31 / 303	21 / 367	38 / 475	19 / 486

The simulated engines were followed with 58 different sensor data, but a dataset was created with 21 of them. In addition, three sensor data measuring environmental conditions have been added to the dataset. The sensor data and their units are listed in Table 2, respectively.

Table 2. All sensors in the C-MAPSS dataset

Symbol	Description	Units
T2	Total temperature at fan inlet	°R
T24	Total temperature at LPC outlet	°R
T30	Total temperature at HPC outlet	°R
T50	Total temperature at LPT outlet	°R
P2	Pressure at fan inlet	psia
P15	Total pressure in bypass-duct	psia
P30	Total pressure at HPC outlet	psia
Nf	Physical fan speed	rpm
Nc	Physical core speed	rpm
epr	Engine pressure ratio (P50/p2)	-
Ps30	Static pressure at HPC outlet	psia
phi	Ratio of fuel flow to Ps30	pps / psi
NRf	Corrected fan speed	rpm
NRc	Corrected core speed	rpm
BPR	Bypass ratio	-
farB	Burner fuel-air ratio	-
htBleed	Bleed Enthalpy	-
Nf_dmd	Demanded fan speed	rpm
PCNFR_dmd	Demanded corrected fan speed	rpm
W31	HPT coolant bleed	lbm / s
W32	LPT coolant bleed	lbm / s

2.2.2. Normalization

The C-MAPSS dataset comprises 26 columns with engine ID, time cycles, three operational conditions, and 21 sensor values. Each of the 21 sensors that are comprised of the C-MAPSS dataset does not change over time. While some sensor values in the dataset decrease towards the end of the engine's life, some increase. Data collected from seven sensors numbered 1, 5, 6, 10, 16, 18, and 19 remain constant over time. These sensor signals are reported not to provide any helpful information by studies in the literature, but they are used in the scope of this work [30].
The data are normalized before training the model we propose. The z-score normalization process was used to ensure that the trained model converges fast and that the features with higher values than other sensor values do not dominate and adversely affect the model's training. Equation 2 shows the z-score normalization process.

$$x_{norm}^{i,j} = \frac{x^{i,j} - \mu^j}{\sigma^j} \quad \forall i,j \tag{2}$$

The μ^j value in Equation 2 shows the mean of the feature, and the σ^j shows its standard deviation of the feature.

2.2.3. Time Windowing

Data collected from sensors as time series must be preprocessed to train, especially to capture the associative connections in the time domain. The time windowing technique is used to capture these associative connections. Thus, the dataset is workable for dynamic and static networks. The sub-datasets in Table 1 have engines with different data lengths. In these sub-datasets, window sizes were determined according to the engine with the lowest data in order to be used in each engine training and test dataset. The FD001 and FD003 sub-datasets are used because the window sizes could be 30 in this study. As the engines in the FD002 and FD004 sub-datasets can have less than 30 samples, they did not use in this study. This windowing process is shown in Figure 4. In this study, the stride process in time windowing was set one. In the time windowing process shown in Figure 4, the status of the

features from the raw dataset after normalized and shifted is shown.

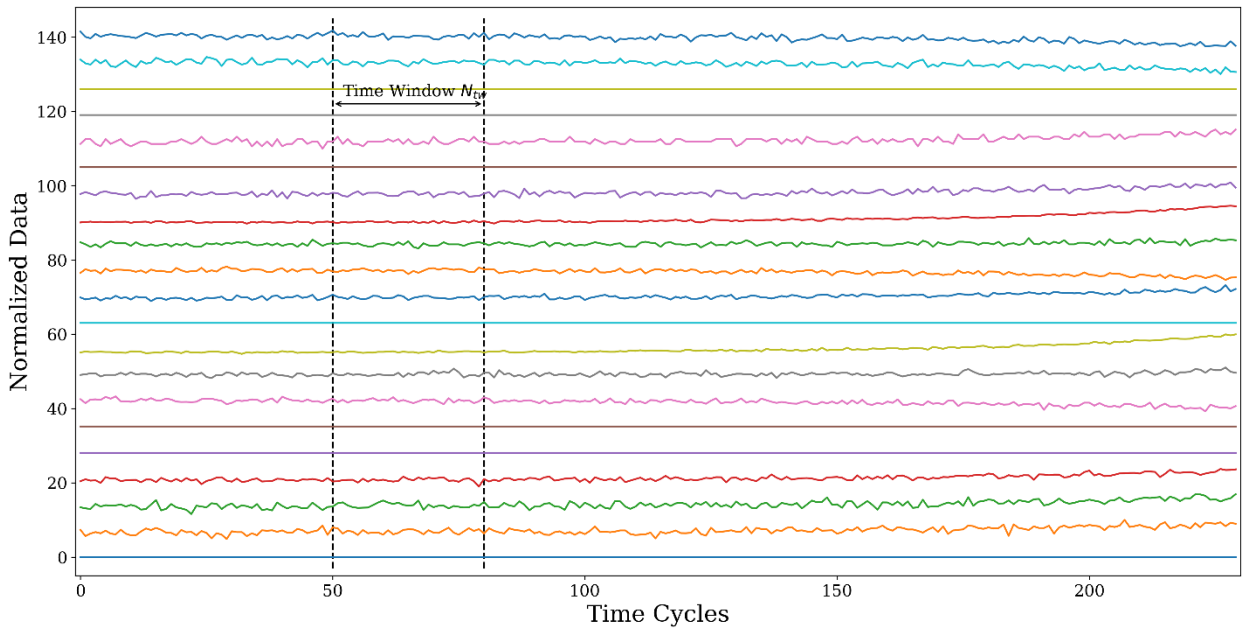

Figure 4. Processing of time windowing with selected features

2.2.4. RUL Labeling

In real-world applications, it is thought that the life of the system studied will end linearly. It is expected that the life of the system or its part will decrease with each operating cycle. However, when the collected data is examined, there is not much change in the initial sensor values of the systems. Sensor values will be changed towards the end of their life compared to the start time. For this reason, Heimes et al. presented a piece-wise degradation model [31]. Linear and piece-wise degradation models are shown in Figure 5 together.

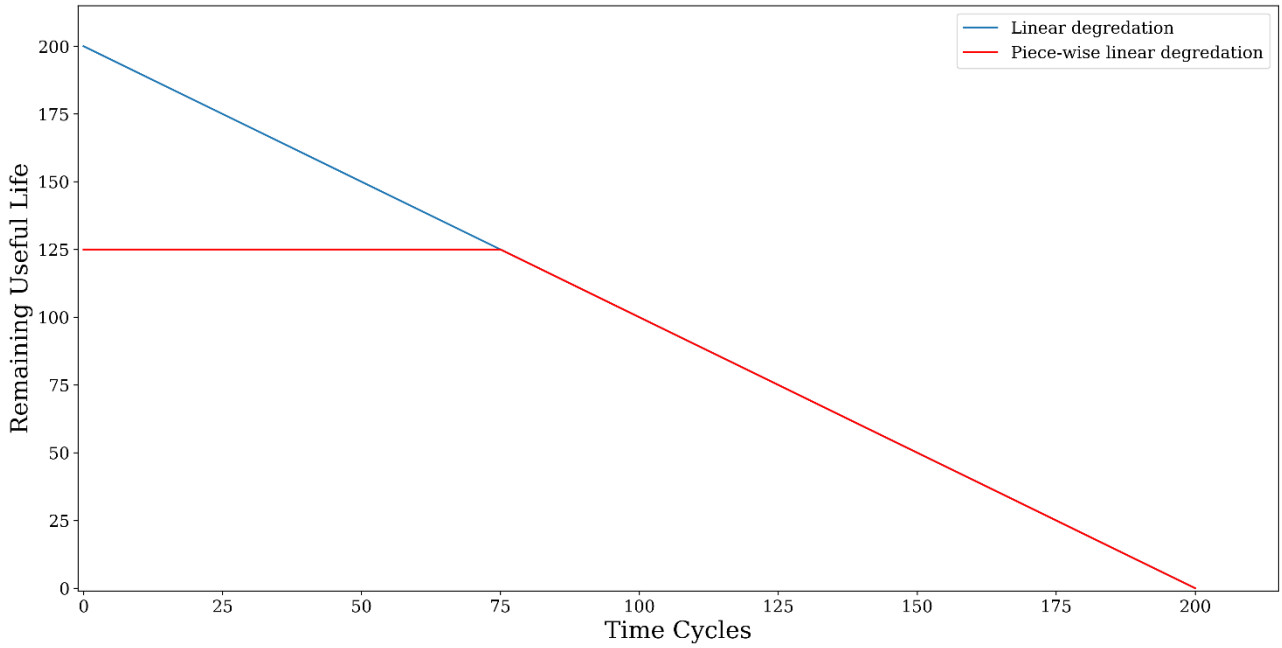

Figure 5. Piece-wise linear degradation function

In the piece-wise degradation model shown in Figure 5, the aero-engines were initially considered healthy. The R_{early} value was determined according to the minimum number of samples in the training datasets. In the C-MAPSS

summary shown in Table 1, the minimum number of samples in the training data appears to be 128. In the literature, it is set between 120-130. Within the scope of this study, the R_{early} value was set as 125.

2.2.5. Evaluation Metrics

All developed predictive models are evaluated with two different functions in the literature. These functions are RMSE and Score functions. Also, Mean Absolute Percentage Error (MAPE) evaluation metric is used in the prediction problems. The RMSE and MAPE functions are shown in equations 4 and 5, respectively. Also, RMSE is widely used in prognostic and health management problems.

$$d_i = RUL_{predicted} - RUL_{actual} \tag{3}$$

$$RMSE = \sqrt{\frac{1}{N}\sum_{i=1}^{N} d_i^2} \tag{4}$$

$$MAPE = \frac{1}{N}\sum_{i=1}^{N} \frac{\left|RUL_{actual} - RUL_{predicted}\right|}{RUL_{actual}} \tag{5}$$

In equations 3 and 4, the d_i value is shown as the difference between the estimated RUL and the actual RUL value. In addition, the score function was suggested to compare the models on the Data Challenge at the 2008 PHM conference [31]. In the score function expressed in equations 6 and 7, the errors obtained as positive and negative produce different values. While the errors obtained as negative are more tolerable, the errors with positive values create higher scores as they can cause catastrophic failures.

$$S_i = \begin{cases} e^{-\frac{d_i}{13}} - 1, & for\ d_i < 0 \\ e^{\frac{d_i}{10}} - 1, & otherwise \end{cases} \tag{6}$$

$$Score = \sum_{i=1}^{N} S_i \tag{7}$$

3. Result and Discussion

In this section, the details of the proposed model and experimental work on the dataset are given. The procedures and methods of the experiments are explained. The results obtained with the proposed model are reported. In addition, the performances on the dataset in RUL estimation are given. Lastly, a comparative table of the results obtained with the proposed system and the other studies in the literature is presented.

3.1. Experiments

In the scope of this paper, the FD001 and the FD003 sub-datasets are selected from the C-MAPSS dataset. A new dataset is created, taking 21 sensor data that monitor aero-engines. Then, the dataset is normalized with the z-score normalization method and is made suitable for training. In order to make more accurate estimations by utilizing historical data, a time windowing technique has been applied to the dataset. The data was processed by determining a 30-length fixed time window (N_{tw}). Thus, each input data is sized as N_{tw} x N_{ft} with 21 selected sensors (N_{ft}). These processes have been applied to both the training and test datasets. RUL labeling was done with a piece-wise

linear degradation model for the values to be estimated during the training. Thus, the necessary preparations for training the proposed CSARN model were made, and then the hyperparameter settings were made.

In the CSARN model, Self-Attention layers and ResNet layers are formed by cascade connection. Each layer and its hyperparameters in the model are given in Table 3. The model coefficients are adjusted to be optimized with adam optimizer [32]. The batch size was determined as 32 during model training. The random validation split was set as 20% for model validation during training. The model is set to train for 250 epochs. Early stopping was used to prevent overfitting. Model training is stopped 20 epochs after the training loss, and validation loss values start to diverge. Thus, model training was stopped beforehand to prevent overfitting before reaching the maximum number of epochs.

Table 3.The details of the CSARN model

Layer Name	Input Size	Output Size	Description
Gaussian Layer	30x21x1	30x21x1	Std value=0.01
Conv 1	30x21x1	30x21x10	11x1,10 filter
Self-Attention	30x21x10	30x21x10	
ResNet Layer 1	30x21x10	30x21x10	
Conv 2	30x21x10	15x21x10	7x1,10 filter, stride 2x1
ResNet Layer 2	15x21x10	15x21x10	
Conv 3	15x21x10	8x21x10	7x1,10 filter, stride 2x1
ResNet Layer 3	8x21x10	8x21x10	
Conv 4	8x21x10	2x21x5	7x1,5 filter
Flatten	2x21x5	210	
Dropout + FC	210	140	Dropout rate=0.3
Dropout + FC	140	90	Dropout rate=0.3
FC	90	1	

Also, the loss function is proposed, like the score function from evaluation metrics. The proposed loss function is shown in equation 7.

$$loss = 5 \times \begin{cases} -d_i \times e^{-\frac{d_i}{13}} - 1, & for\ d_i < 0 \\ d_i \times e^{\frac{d_i}{10}} - 1, & otherwise \end{cases} \quad (8)$$

In the above equation, d_i represents the difference between the predicted RUL and the actual RUL value. The trained model was used for RUL estimation in the test dataset. As with the score function, a loss function that is designed could tolerate negative values.

3.2. Experimental Analysis and Results

In this section, the performance of the proposed CSARN model on the FD001 and FD003 datasets has been examined. Model training was done with the training set of each sub-dataset and tested on its test dataset. There are 100 motors in the test datasets. In the data of these engines, data has been collected from the beginning, and at a point before the end of the engine's life, the data acquisition from the engine was stopped. As of this point, the RUL of the engine has been estimated. The estimation values obtained were also interpreted and examined according to the evaluation metrics used in the literature.

The estimations obtained for each engine in the FD001 test dataset are shown in Figure 6 from smallest to largest for better visualization. In addition, the actual RUL values and the RUL labeling part suitable for the piece-wise linear degradation model are given together. As seen in the figure, the estimations made towards the end of the life of the motors give more precise results. In addition, it is seen that the variance of the results obtained in the middle part of the estimated values is higher than in other parts.

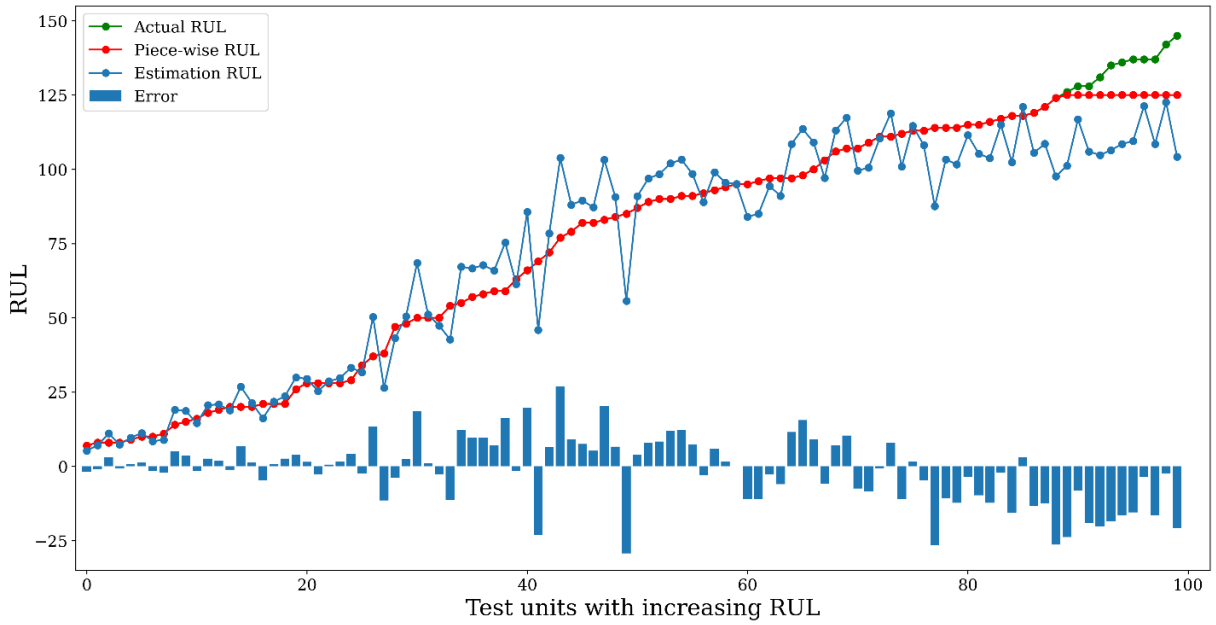

Figure 6. RUL estimation of all engines in the FD001 test dataset

In the same way, the engine's lives are predicted for the FD003 test dataset and are shown in Figure 7. The graph shows the estimated RUL values, piece-wise RUL values, and actual RUL values. The obtained results with high score values are expected with the same model because the FD003 dataset has two failure modes. As in the FD001 dataset, it is seen that the variance is higher in the middle part of the RUL values.

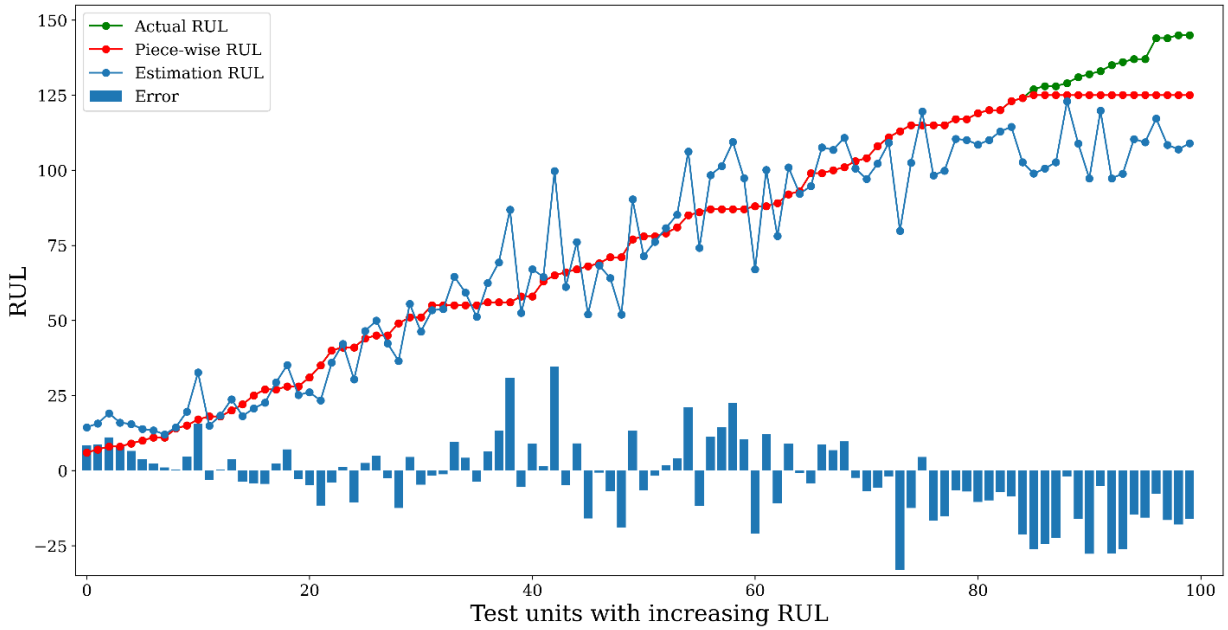

Figure 7. RUL estimation of all engines in the FD003 test dataset

The evaluation results made on the sub-datasets used with the proposed model are given in Table 4. The evaluations were obtained with the RMSE and Score functions used in the literature. In the FD001 and FD003 sub-datasets, RMSE values were obtained as 11.017 and 12.629, respectively. Likewise, when the Score function is evaluated, it is seen that the results obtained are 157.19 and 218.6. Also, the obtained MAPE results are 0.127 and 0.193, respectively. When the dataset is examined under a single operating condition but in two different failure modes, the results obtained with the same model are higher. This situation shows that the data obtained from the system has become more complex, and the degradation model has become harder to predict.

Table 4. The obtained results via the proposed model

	FD001			FD003		
	RMSE	Score	MAPE	RMSE	Score	MAPE
CSARN	11.017	157.19	0.127	12.629	218.6	0.193

To illustrate the effect of the model on the motors in the training and test dataset, real and estimated RUL plots of randomly selected motors from the FD001 are shown in Figure 8. Likewise, random motors were selected in the FD003 dataset and are shown in Figure 9.

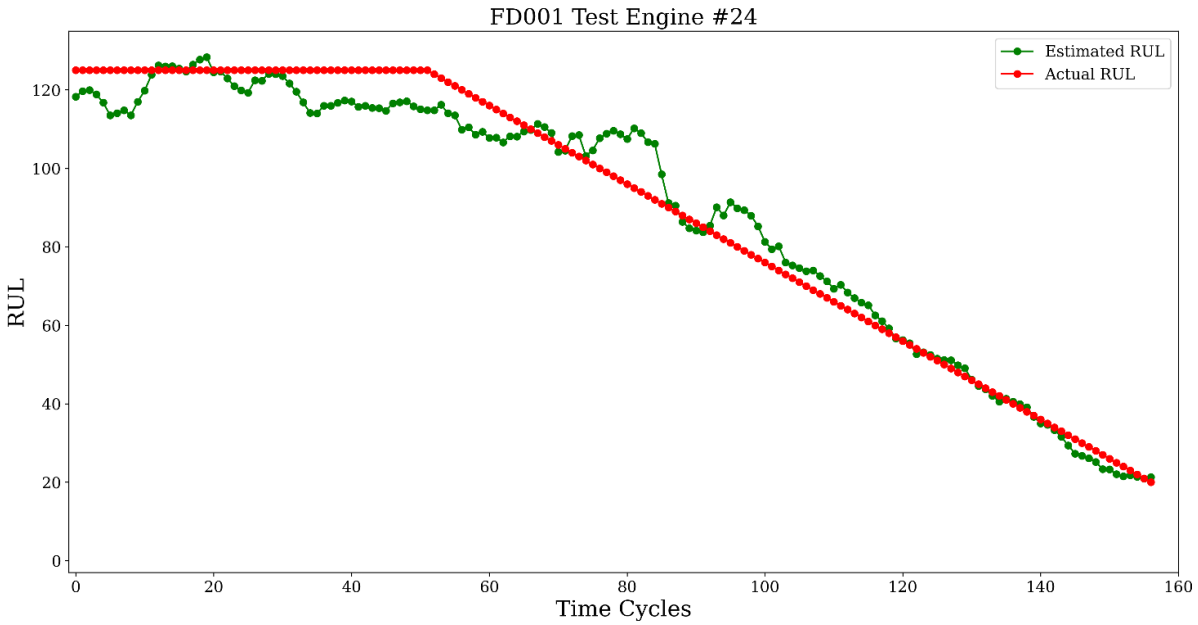

Figure 8. RUL prediction results in each time cycles engine no 24

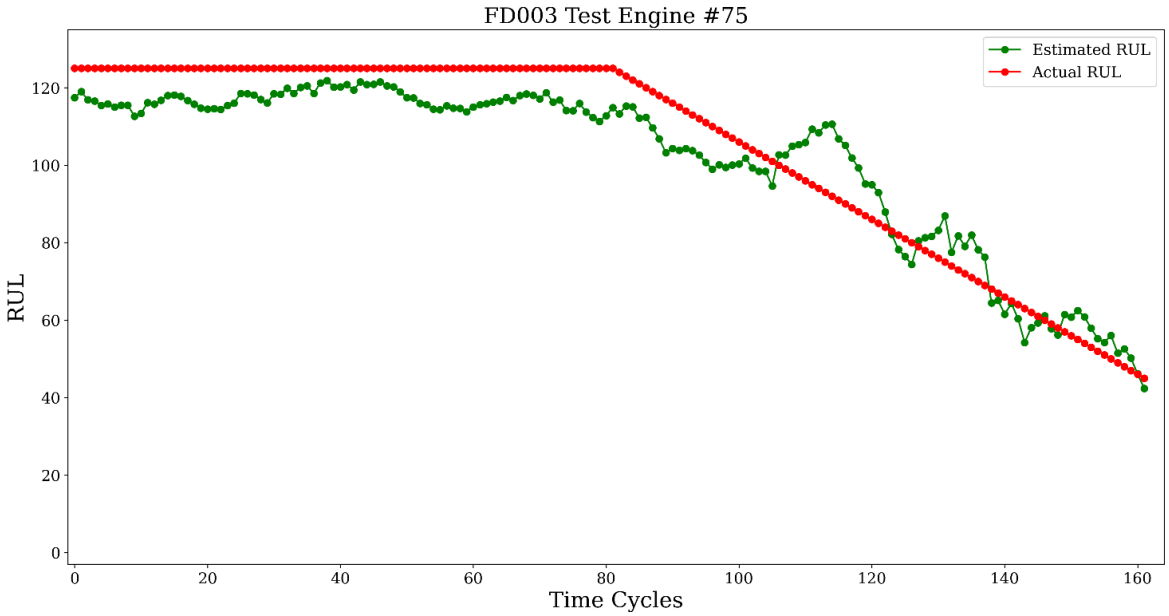

Figure 9. RUL prediction results in each time cycles engine no 75

3.3. Comparison with other studies

In this section, experimental studies and other state-of-the-art methods in the literature are compared. The results obtained in the comparison are given in chronological order. The results of the proposed CSARN method and other methods are shown in Table 5.

Table 5. Comparison the CSARN model and the state-of-the-art models in literature

Methods	Year	FD001		FD003	
		RMSE	Score	RMSE	Score
MODBNE [11]	2016	15,04	334,23	12,51	421,91
D-LSTM [13]	2017	16,14	338	16,18	852
HDNN [18]	2019	13,017	245	12,22	287,72
CNNTW [33]	2019	12,18	224,16	15,67	1279,85
CapsNet [17]	2019	12,58	276,34	11,71	283,81
DAG [20]	2019	11,96	229	12,46	535
NPBLSTM [19]	2020	12,321	238,34	**11,364**	226,482
ATS2S [22]	2020	12,63	243	11,44	263
CNN-BiLSTM [34]	2021	12,13	174	11,96	242
CNN+ATT [24]	2021	11,48	198	12,31	251
LSTM-MLSA [30]	2021	11,567	252,86	12,134	370,39
Bi-LSTM-Two Stream [35]	2022	11,96	206,33	13,41	223,36
BiGRU-TSAM [36]	2022	12,56	213,35	12,45	232,86
CSARN	2022	**11,017**	**157.19**	12,629	**218,6**

As can be seen in Table 5, the proposed model gave the best results in the evaluation of score function in the FD001 and FD003 sub-datasets compared to other models in the literature. However, in the FD003 sub-dataset, obtained the RMSE value is not the best, but it is a fair result. Especially in the score function, much better success was achieved compared to other studies. In the proposed model, the Self-Attention layer and the loss function that we have proposed have been effective.

4. Conclusion

In this study, the effect of the cascaded structure of Self-Attention and ResNet layers on RUL estimation was investigated. It was focused on important points with the Self-Attention layer for better estimation in the time domain. The model was established as an end-to-end structure that can do automatic feature extraction with Convolution layers. In addition, with the ResNet structure integrated into the model, the effect of the loss value from the last layer to the first layer is effectively spread. Different actions were taken to prevent overfitting within the study's scope and in the tested models. First of all, Gaussian noise was added by modeling the data. Thus, it was ensured that the model works more robustly or produces results in noisy data. In addition, it was tried to prevent the model from memorizing during training by adding dropout layers between FC layers. However, the weight coefficients in each model layer were multiplied by a regularization coefficient to prevent overfitting. Finally, while training the model, it was ensured that the training process was stopped without memorizing the proposed model with the early stopping mechanism. The performance of the proposed model was tested on the FD001 and FD003 sub-datasets of the C-MAPSS dataset. The best score value was obtained in these sub-datasets. In addition, the lowest RMSE value was found in the FD001 sub-dataset. These sub-datasets have been chosen because training can be done without structural changes in the proposed model.

Compared to other state-of-the-art models in the literature, successful results were obtained on RUL estimation. In future studies, the proposed model's extension to other sub-datasets and its performance in other test datasets will be examined within the scope of this study. Also, on the second loss function, which merges with the proposed loss function because of the success on the score function, will be worked on. In addition, the contributions of other dynamic network structures (LSTM, GRU) found in the literature to the proposed model structure will be investigated in future studies.

References

[1] Xu, J., Wang, Y., & Xu, L. (2013). PHM-oriented integrated fusion prognostics for aircraft engines based on sensor data. IEEE Sensors Journal, 14(4), 1124-1132.

[2] Nandi, S., Toliyat, H. A., & Li, X. (2005). Condition monitoring and fault diagnosis of electrical motors—A review. IEEE transactions on energy conversion, 20(4), 719-729.

[3] Kara, A. (2021). A data-driven approach based on deep neural networks for lithium-ion battery prognostics. Neural Computing and Applications, 33(20), 13525-13538.

[4] Park, J., & Jung, W. (2015). A systematic framework to investigate the coverage of abnormal operating procedures in nuclear power plants. Reliability Engineering & System Safety, 138, 21-30.

[5] Hou, G., Xu, S., Zhou, N., Yang, L., & Fu, Q. (2020). Remaining useful life estimation using deep convolutional generative adversarial networks based on an autoencoder scheme. Computational Intelligence and Neuroscience, 2020.

[6] Li, H., Zhao, W., Zhang, Y., & Zio, E. (2020). Remaining useful life prediction using multi-scale deep convolutional neural network. *Applied Soft Computing*, *89*, 106113.

[7] Correia, J. A., De Jesus, A. M., & Fernández-Canteli, A. (2012). A procedure to derive probabilistic fatigue crack propagation data. *International Journal of Structural Integrity*.

[8] Liao, L. (2013). Discovering prognostic features using genetic programming in remaining useful life prediction. *IEEE Transactions on Industrial Electronics*, *61*(5), 2464-2472.

[9] Li, N., Lei, Y., Lin, J., & Ding, S. X. (2015). An improved exponential model for predicting remaining useful life of rolling element bearings. *IEEE Transactions on Industrial Electronics*, *62*(12), 7762-7773.

[10] Sateesh Babu, G., Zhao, P., & Li, X. L. (2016, April). Deep convolutional neural network based regression approach for estimation of remaining useful life. In International conference on database systems for advanced applications (pp. 214-228). Springer, Cham.

[11] Zhang, C., Lim, P., Qin, A. K., & Tan, K. C. (2016). Multiobjective deep belief networks ensemble for remaining useful life estimation in prognostics. IEEE transactions on neural networks and learning systems, 28(10), 2306-2318.

[12] Li, X., Ding, Q., & Sun, J. Q. (2018). Remaining useful life estimation in prognostics using deep convolution neural networks. Reliability Engineering & System Safety, 172, 1-11.

[13] Zheng, S., Ristovski, K., Farahat, A., & Gupta, C. (2017, June). Long short-term memory network for remaining useful life estimation. In 2017 IEEE international conference on prognostics and health management (ICPHM) (pp. 88-95). IEEE.

[14] Wu, Y., Yuan, M., Dong, S., Lin, L., & Liu, Y. (2018). Remaining useful life estimation of engineered systems using vanilla LSTM neural networks. Neurocomputing, 275, 167-179.

[15] Yu, W., Kim, I. Y., & Mechefske, C. (2019). Remaining useful life estimation using a bidirectional recurrent neural network based autoencoder scheme. Mechanical Systems and Signal Processing, 129, 764-780

[16] Wang, J., Wen, G., Yang, S., & Liu, Y. (2018, October). Remaining useful life estimation in prognostics using deep bidirectional LSTM neural network. In 2018 Prognostics and System Health Management Conference (PHM-Chongqing) (pp. 1037-1042). IEEE.

[17] Ruiz-Tagle Palazuelos, A., Droguett, E. L., & Pascual, R. (2020). A novel deep capsule neural network for remaining useful life estimation. Proceedings of the Institution of Mechanical Engineers, Part O: Journal of Risk and Reliability, 234(1), 151-167.

[18] Al-Dulaimi, A., Zabihi, S., Asif, A., & Mohammadi, A. (2019). A multimodal and hybrid deep neural network model for remaining useful life estimation. Computers in industry, 108, 186-196.

[19] Al-Dulaimi, A., Zabihi, S., Asif, A., & Mohammed, A. (2020). NBLSTM: Noisy and hybrid convolutional neural network and BLSTM-Based deep architecture for remaining useful life estimation. Journal of Computing and Information Science in Engineering, 20(2), 021012.

[20] Li, J., Li, X., & He, D. (2019). A directed acyclic graph network combined with CNN and LSTM for remaining useful life prediction. IEEE Access, 7, 75464-75475.

[21] Song, Y., Shi, G., Chen, L., Huang, X., & Xia, T. (2018). Remaining useful life prediction of turbofan engine using hybrid model based on autoencoder and bidirectional long short-term memory. Journal of Shanghai Jiaotong University (Science), 23(1), 85-94.

[22] Ragab, M., Chen, Z., Wu, M., Kwoh, C. K., Yan, R., & Li, X. (2021). Attention-based sequence to sequence model for machine remaining useful life prediction. Neurocomputing, 466, 58-68.

[23] Liu, L., Song, X., & Zhou, Z. (2022). Aircraft engine remaining useful life estimation via a double attention-

based data-driven architecture. Reliability Engineering & System Safety, 221, 108330.

[24] Tan, W. M., & Teo, T. H. (2021). Remaining useful life prediction using temporal convolution with attention. Ai, 2(1), 48-70.

[25] Xia, J., Feng, Y., Lu, C., Fei, C., & Xue, X. (2021). LSTM-based multi-layer self-attention method for remaining useful life estimation of mechanical systems. Engineering Failure Analysis, 125, 105385.

[26] Zhao, H., Jia, J., & Koltun, V. (2020). Exploring self-attention for image recognition. In Proceedings of the IEEE/CVF Conference on Computer Vision and Pattern Recognition (pp. 10076-10085).

[27] Vaswani, A., Shazeer, N., Parmar, N., Uszkoreit, J., Jones, L., Gomez, A. N., ... & Polosukhin, I. (2017). Attention is all you need. Advances in neural information processing systems, 30.

[28] He, K., Zhang, X., Ren, S., & Sun, J. (2016). Deep residual learning for image recognition. In Proceedings of the IEEE conference on computer vision and pattern recognition (pp. 770-778).

[29] Saxena, A., Goebel, K., Simon, D., & Eklund, N. (2008, October). Damage propagation modeling for aircraft engine run-to-failure simulation. In 2008 international conference on prognostics and health management (pp. 1-9). IEEE.

[30] Xia, J., Feng, Y., Lu, C., Fei, C., & Xue, X. (2021). LSTM-based multi-layer self-attention method for remaining useful life estimation of mechanical systems. Engineering Failure Analysis, 125, 105385.

[31] Heimes, F. O. (2008, October). Recurrent neural networks for remaining useful life estimation. In 2008 international conference on prognostics and health management (pp. 1-6). IEEE.

[32] Kingma, D. P., & Ba, J. (2014). Adam: A method for stochastic optimization. arXiv preprint arXiv:1412.6980.

[33] Yang, H., Zhao, F., Jiang, G., Sun, Z., & Mei, X. (2019). A novel deep learning approach for machinery prognostics based on time windows. Applied Sciences, 9(22), 4813.

[34] Song, J. W., Park, Y. I., Hong, J. J., Kim, S. G., & Kang, S. J. (2021, May). Attention-based bidirectional LSTM-CNN model for remaining useful life estimation. In 2021 IEEE International Symposium on Circuits and Systems (ISCAS) (pp. 1-5). IEEE.

[35] Jin, R., Chen, Z., Wu, K., Wu, M., Li, X., & Yan, R. (2022). Bi-LSTM-Based Two-Stream Network for Machine Remaining Useful Life Prediction. IEEE Transactions on Instrumentation and Measurement, 71, 1-10.

[36] Zhang, J., Jiang, Y., Wu, S., Li, X., Luo, H., & Yin, S. (2022). Prediction of remaining useful life based on bidirectional gated recurrent unit with temporal self-attention mechanism. Reliability Engineering & System Safety, 221, 108297.

J Inno Sci Eng,2023, 7(1):106-121
http://doi.org/10.38088/jise.1162151

Research Article

Fuzzy Modeling of non-MCDM Problems Under Indeterminacy

Gürkan Isik [1*]

[1*] *Department of Industrial Engineering, Faculty of Engineering and Natural Sciences, Bursa Technical University, Bursa, 16310*

Abstract

Fuzzy set theory (FST) is a popular approach for modeling the uncertainties of real-life problems. In some cases, uncertainty level of the events may not be determined surely because of some environmental factors. There are various FST extensions in the literature that consider such indeterminacy cases in modeling. Since some parts of the theories of FST extensions overlap with some others, the theories and the nature of considered scenarios must be understood well to obtain reliable results. Nevertheless, most of the studies in the literature do not conceptually analyze the nature of the uncertainty and decides an FST extension as a pre-step of the study without expressing an apparent reason. Therefore, the quality of the obtained results becomes questionable. Most of the FST extensions have been developed in line with the requirements of Multi-Criteria Decision-Making (MCDM) problem thus assumptions and limitations of these theories can cause reliability issues for the fuzzy models of the problems different from MCDM. In the scope of this study, capabilities, advantages, and disadvantages of well-known FST extensions that consider indeterminacy are conceptually analyzed and compared in line with the needs of modeling of the continuous systems, MCDM problems, and different problems from MCDM. The analysis has also been illustrated on numerical examples to make findings clear. The analysis showed that some extensions have clear advantages over others for specific scenarios. This study is an invitation to fulfill the gap in the field of fuzzy modeling of the different problems from MCDM.

Keywords: Fuzzy modeling, Fuzzy set extensions, Indeterminacy, MCDM.

Cite this paper as:
Uysal, M. (2023). *Fuzzy Modeling of non-MCDM Problems Under Indeterminacy*. Journal of Innovative Science and Engineering.**Error! Reference source not found.**:106-121

*Corresponding author: Gürkan Isik
E-mail: gurkan_isik@msn.com

Received Date:15/08/2022
Accepted Date:19/01/2023

1. Introduction

Vast majority of real-world applications of engineering problems include uncertainty. However, most of the engineering techniques have been designed for certain events so their results can have reliability problem. Fuzzy set theory (FST) provided a big contribution to the literature for modeling of uncertainty. FST has been extended in different perspectives to model the uncertainties having different natures originated from their causes such as hesitation of the experts about the event. It is crucial to choose the most suitable FST extension in modeling to achieve reliable results. Zadeh [1] proposed the FST to deal with the problems in which the source of uncertainty is caused by the lack of clear criteria of class membership rather than the existence of random variables. For an Ordinary Fuzzy Set (FS), certainty level about an event is represented with membership degree (MD) concept. While MD is getting bigger, the certainty of the event increases.

In some cases, it is difficult to decide the MDs of the elements because of some factors such as lack of expertness about the event or system. In such cases, uncertainty level cannot be well-defined. This situation is named as "Indeterminacy" scenario and Indeterminacy Degree (IDD) represents the level of lack of information about MD. Atanassov [2] extended the FST with the name Intuitionistic FS (IFS) to provide better modeling of cases that include lack of information about MD. In IFS theory, IDD is decided based on MD and Non-Membership Degree (NMD). In some cases, such as collecting data from multiple sources can cause inconsistency between MD and NMD. This should also be handled in modeling to reach reliable results for these scenarios. For this aim, Smarandache [3] generalized IFSs as Neutrosophic Set (NS) in a theoretical perspective by allowing independent MD, NMD and IDD to give ability to model with inconsistent data. However, logical meaning of "independency of IDD" is a question mark for most of the scenarios. Yager [4] suggested Pythagorean FS (PFS) as a theoretical extension of IFSs based on Pythagoras' theorem for the modeling of the systems with inconsistent data. For PFSs, the sum of the squares of MD and NMD is limited by one. In PFS theory, IDD is dependent on MD and NMD, but it gives ability to model the scenarios including inconsistency. However, allowed inconsistency level is limited for PFSs. To extend this limitation, Yager [5] generalized the PFS for q^th power of the MD and NMD with the name q-Rung Orthopair FS (q-ROFS). Q-ROFS theory gives more flexibility than PFS theory but deciding the best fitting q brings calculation complexity. Senapati & Yager [6] offered Fermatean FS (FFS) by changing the condition of PFSs as the sum of the 3^rd power of MD and NMD is limited by one. This approach provides a larger limitation for inconsistency level than PFS theory. These extensions give ability to model inconsistency and indeterminacy cases, but they may not always be sufficient to model the uncertainty in a reliable way. Lack of information about the event may also be caused by the refusal of the information source to provide information. Cuong & Kreinovich [7] generalized the IFSs with the name Picture FS (PcFS) by considering a new concept named "neutral membership degree" (NeMD) besides MD, NMD and IDD to give ability to model the refusal case. PcFS is capable of modeling the scenarios including indeterminacy with consistent data. If the scenario also includes inconsistency, it is not suitable for modeling. Kahraman & Kutlu Gündoğdu [8] developed Spherical FS (SFS) as a generalization of PcFSs by employing a similar approach with PFS theory to allow inconsistent data case. In SFS theory, the sum of the squares of the MD, NMD and NeMD is bounded by one.

In the literature, there are huge number of studies using FST extensions. Vast majority of these studies focus on one-time Multi-Criteria Decision-Making (MCDM) problem. For this reason, theories have been built in line with the requirements of MCDM problem. Most of the formulations do not offer sufficient capabilities for modeling of

continuous systems, different problems than MCDM, and even the Decision Making (DM) problems that need sensitive calculation in decision cycle. For these types of problems, usage of the reviewed FST extensions without making novel contributions by integrating more sophisticated mechanisms brings reliability issue for the obtained results or makes sensitivity analysis dysfunctional. For example, if the variability of the collected data increases during a time, the collected data may become useless with the PFS model of a continuous system because of violating the inconsistency limitation. Even worse, if this is noticed after a while, the results will be unreliable during this period. There are reliability issues for also MCDM problems in most of the studies that use one of the reviewed FST extensions. Because, these studies do not present the motivation lying behind their FST extension preference. This prevents evaluating the compatibility of the FST extension with the scenario. For example, in the review studies conducted by Kaya et al. [9], Mardani et al. [10], and Salih et al. [11], the suitability of the scenarios to the preferred FST extensions is not considered in a conceptual perspective. Similarly, none of the studies cited in these review studies, provide a satisfactory justification for their FST extension choices and discuss the suitability of the preferred FST extension with the considered scenario from a conceptual perspective. In most of the studies such as [12], a linguistic term set including indeterminacy is pre-determined without presenting any reason, and experts choose between these terms without making any additional justification as if they are using ordinary FS during the assessment operations. This means that the indeterminacy is emerged by the initial configuration itself not by the hesitancy of the experts. It is clear that such an application will yield results having reliability issue. There are some other review studies in the literature investigating the FST extensions, but they generally focus on the mathematical aspect. For example, Kahraman et al. [13] classified the FST extensions in two groups as hesitancy dependent (IFS, PFS, FFS, q-ROFS) and refusal degree dependent (NS, PcFS, SFS) with a mathematical definition-oriented perspective and does not present a conceptual analysis. Unlike the mentioned studies, only Sevastjanov & Dymova [14] criticizes the necessity and applicability of NSs, PFSs and SFSs in a conceptual perspective but it does not present a detailed comparison.

In the scope of this study, it is aimed to conceptually analyze and compare the FST extensions that consider indeterminacy to build a guide for the selection of the suitable FST extension in fuzzy modeling of the non-MCDM problems (continuous systems and the problems different from one-time MCDM problems) by considering indeterminacy. By this way, an initial step is taken for filling the gap in the field of improving the reliability of fuzzy modeling of the different problems from MCDM. It is expected that this study will also create a motivation for studies to increase the reliability of MDCM models.

The paper is organized as follows: FST extensions including indeterminacy are analyzed and compared according to some pre-determined criteria in Section 2. The comparative analysis is summarized, opinions and findings are presented in Section 3. Conclusions and future research directions are presented in Section 4.

2. Material and Methods

Various extensions of FST have been offered to handle different type of uncertainties. Close to twenty FST extensions and their hybrid combinations have been studied in the literature. Indeterminacy is considered as a part of uncertainty in nearly half of these studies. Figure 1 shows the relations between the popular FST extensions considering indeterminacy. More than 50.000 studies were conducted since 2012 by using these FST extensions according to Google Scholar database. When the studies are analyzed in detail, it is seen that considered scenarios are too similar. For this reason,

understandings the theories and the nature of scenarios is crucial to obtain reliable results. Following subsections are summarizing the theoretical backgrounds of these FST extensions.

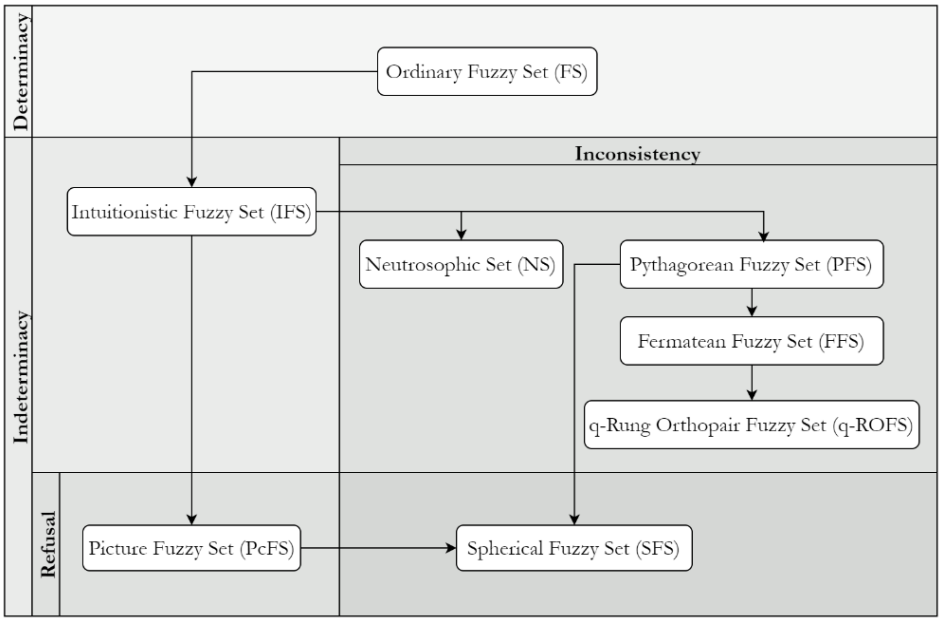

Figure 1. Relations between fuzzy set extensions that consider indeterminacy

2.1. Fuzzy Set Extensions Considering Indeterminacy

The uncertainty is modelled with the membership function (MF) concept based on a continuous variable x in [0, 1] in FST. A set element can be partially member and non-member simultaneously in FST. The level of uncertainty of the membership of a set element is represented with the term MD. If MD is high, the uncertainty is low; and if it is low, the uncertainty is high [1]. A FS (namely ordinary FS) is defined as below:

Definition 1: Let X be a given universe, $\mu_{\tilde{A}}(x) \in [0,1]$ be the MF and $\vartheta_{\tilde{A}}(x)$ be the NMF. An FS $\tilde{A}$ is defined as $\tilde{A} = \{ x, \mu_{\tilde{A}}(x) \mid x \in X \}$ and satisfies Eq. (1) [1]:

$$\mu_{\tilde{A}}(x) + \vartheta_{\tilde{A}}(x) = 1 \tag{1}$$

MFs can have different shapes but the most popular ones are triangular and trapezoidal FSs. Figure 2 shows examples for these popular MF shapes. A triangular FS is represented with three points as (a,b,c): the limiting two of them having MD = 0 (a and c) are "support points" and third point having MD = 1 (b) is "core". A trapezoidal FS is represented with four points as (a,b,c,d): the limiting two points a and d are the support points and the interval having MD=1 [b,c] is core. For a trapezoidal FS, every point inside [b,c] interval is a core point.

If it is hard to decide the FS shape, support points and the core, direct usage of ordinary FSs may not be possible. In most real cases, it is more practical to use interval-valued numbers as MF and NMF. These type of FSs are named Interval Valued FSs (IVFSs). An IVFS is defined as below:

Definition 2: Let X be a given universe and, $\mu_{\tilde{A}}^{-}(x)$, $\mu_{\tilde{A}}^{+}(x)$ are fuzzy subsets of X. An IVFS $\tilde{A}$ on X is defined as $\tilde{A} = \{ x, [\mu_{\tilde{A}}^{-}(x), \mu_{\tilde{A}}^{+}(x)] \mid x \in X \}$ and satisfies Eq. (2) [15]:

$$\mu_{\tilde{A}}^{-}(x) \leq \mu_{\tilde{A}}^{+}(x), \forall x \in X \tag{2}$$

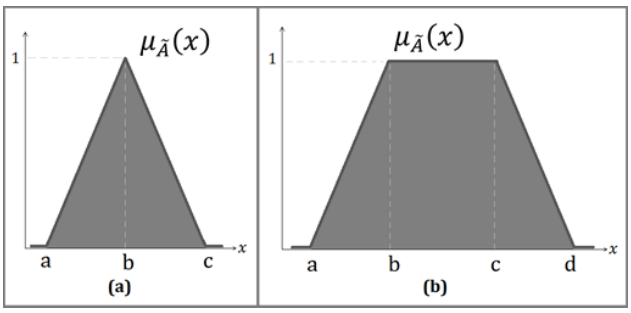

Figure 2. Membership functions; (a) triangular and (b) trapezoidal fuzzy sets

2.1.1. Intuitionistic Fuzzy Sets

In FSTs, MD and NMD are complement of each other and the sum of MD and NMD is equal to 1 for each set element. However, it may not always be possible to determine the MD and NMD values such that whose summation is equal to 1. This type of scenarios is named "incomplete information case". IFSs have been proposed for modeling the uncertainties including incomplete information case. An IFS is defined as below:

Definition 3: Let X be a given universe, $\mu_{\tilde{\tilde{A}}}(x) \in [0,1]$ be the MF and $\vartheta_{\tilde{\tilde{A}}}(x)$ be the NMF. An IFS $\tilde{\tilde{A}}$ is represented as $\tilde{\tilde{A}} = \{ x, \mu_{\tilde{\tilde{A}}}(x), \vartheta_{\tilde{\tilde{A}}}(x) \mid x \in X \}$ and satisfies Eq. (3) [2]:

$$\mu_{\tilde{\tilde{A}}}(x) + \vartheta_{\tilde{\tilde{A}}}(x) \leq 1 \tag{3}$$

In IFS theory, MD and NMD of set elements are interdependent since the value of MD limits the possible values of NMD. The difference between 1 and the sum of MD and NMD is named Indeterminacy Degree (IDD) and is calculated as shown in Eq. (4) [9]:

$$\pi_{\tilde{\tilde{A}}}(x) = 1 - \mu_{\tilde{\tilde{A}}}(x) - \vartheta_{\tilde{\tilde{A}}}(x) \tag{4}$$

IFS formulation generalizes the ordinary FS formulation. It becomes equivalent with ordinary FSs when 0 is assigned to IDD.

2.1.2. Picture Fuzzy Sets

IFS theory assumes that the lack of information about MD and NMD is caused by indeterminacy. However, it can be caused by some other factors such as refusal of the one who make assessment. Voting is a proper example of a such scenario. The voters can be grouped as: (i) vote for, (ii) vote against, (iii) vote blank, (iv) non-voting [7]. Consideration of this type of scenarios yields a new FST extension namely Picture Fuzzy Set (PcFS). A PcFs is defined as below:

Definition 4: Let X be a given universe, $\mu_{\tilde{A}}(x) \in [0,1]$ be the MF and $\vartheta_{\tilde{A}}(x) \in [0,1]$ be the NMF and, $\eta_{\tilde{A}}(x) \in [0,1]$ be the neutral membership function (NeMF). A PcFS $\tilde{A}$ is represented as $\tilde{A} = \{ x, \mu_{\tilde{A}}(x), \vartheta_{\tilde{A}}(x), \eta_{\tilde{A}}(x) \mid x \in X \}$ and satisfies Eq. (5) [7]:

$$\mu_{\tilde{A}}(x) + \vartheta_{\tilde{A}}(x) + \eta_{\tilde{A}}(x) \leq 1 \tag{5}$$

Refusal degree (RD) is calculated as shown in Eq. (6) [7]:

$$\rho_{\tilde{A}}(x) = 1 - \mu_{\tilde{A}}(x) - \vartheta_{\tilde{A}}(x) - \eta_{\tilde{A}}(x) \tag{6}$$

2.1.3. Neutrosophic Sets

In some cases, such as providing information from multiple sources, the sum of MD and NMD can exceed 1 and the main condition of FST presented in Eq. (1) is violated. This scenario is named as "inconsistent information case". If inconsistency is available on data and it is planned to use ordinary FSs or IFSs in modeling, the data must be converted by using an approximation approach or the data must be recollected until reaching consistent data. However, it may not be possible to collect suitable data even if it is tried again and again. An assumption or a change in data collection procedure may be needed to collect suitable data but this generally means loss of information. If the transformation is made on the collected data, it will also cause loss of information. Both these approaches can reduce the model's reliability. To avoid such transformations, NS theory was suggested in the literature. NS is the generalization of IFS. NS gives ability to set values for membership, non-membership, and indeterminacy independent from each other. This leads up the ability of modeling with inconsistent data.

The terminology for NSs is different than IFS terminology. The MD is named "truthiness" and NMD is named "falsity". As a characteristic feature of NS theory, the indeterminacy is handled as a separate term. An NS is defined as below:

Definition 5: Let $t \in [0,1]$ be truthiness, $f \in [0,1]$ be falsity and, $i \in [0,1]$ be indeterminacy. A NS $\tilde{\tilde{A}}$ is defined as $\tilde{\tilde{A}} = (t, i, f)$ and satisfies Eq. (7) [3]:

$$0 \leq t + i + f \leq 3 \tag{7}$$

Some problems may not be suitable for modeling with inconsistent data. For such cases, loss of information is inevitable. For such problems, the data can be normalized by dividing each of the terms with total of the terms to satisfy Eq. (8) [16]. After the normalization, the model becomes conceptually near-equivalent to IFS model.

$$t + i + f = 1 \tag{8}$$

2.1.4. Pythagorean Fuzzy Sets

For the considered problem, if the inconsistency is always occurred under a specific limit, PFS can be used for modeling the event. A PFS is defined based on two concepts: support for membership and support against membership.

Definition 6: Let X be a given universe, and $\theta(x) \in [0, \pi/2]$ be a radian angle. The support for membership ($A_Y(x)$) and the support against membership ($A_N(x)$) for a PFS $\tilde{A}$ are defined as in Eq (9) [4].

$$A_Y(x) = r(x) \times \cos\big(\theta(x)\big),\ A_N(x) = r(x) \times \sin\big(\theta(x)\big) \tag{9}$$

The strength of commitment ($r(x) \in [0,1]$) and the direction of commitment ($d(x) \in [0,1]$) are defined as shown in Eq. (10) [4]:

$$r(x) = \sqrt{\big(A_Y^2(x) + A_N^2(x)\big)},\ d(x) = \frac{(\pi - 2 \times \theta(x))}{\pi} \tag{10}$$

Eq. (11) shows the definition of a PFS $\tilde{A}$ with the terminology and symbols of IFS theory.

$$\tilde{A} = \{ x, \mu_{\tilde{A}}(x) = A_Y(x), \vartheta_{\tilde{A}}(x) = A_N(x) \mid x \in X \}, \mu_{\tilde{A}}^2(x) + \vartheta_{\tilde{A}}^2(x) \leq 1 \tag{11}$$

Depending on this definition, IDD of an element $x \in X$ is obtained as shown in Eq. (12):

$$\pi_{\tilde{A}}(x) = \sqrt{1 - r^2(x)} = \sqrt{1 - \left(\mu_{\tilde{A}}^2(x) + \vartheta_{\tilde{A}}^2(x)\right)} \tag{12}$$

2.1.5. Fermatean Fuzzy Sets

Modeling with PFS is possible if and only if the inconsistency of data is under a limit. If the inconsistency violates Eq. (11) for some of the set elements, PFSs cannot be used. The general approach may be using NSs. However, if the independency of MD, NMD and IDD is not a desired circumstance, NS may not be suitable. FFS is a similar FST extension with PFS but its inconsistency limit is larger than PFS. An FFS is defined as follows:

Definition 7: Let X be a given universe, $\alpha_{\tilde{\mathcal{F}}}(x) \in [0,1]$ be MD, and $\beta_{\tilde{\mathcal{F}}}(x) \in [0,1]$ be MD for a set element $x \in X$. An FFS $\tilde{\mathcal{F}}$ is represented as $\tilde{\mathcal{F}} = \{ x, \alpha_{\tilde{\mathcal{F}}}(x), \beta_{\tilde{\mathcal{F}}}(x) \mid x \in X \}$ and satisfies Eq (13) [6].

$$0 \leq \alpha_{\tilde{\mathcal{F}}}^3(x) + \beta_{\tilde{\mathcal{F}}}^3(x) \leq 1 \tag{13}$$

Thus, IDD of an element $x \in X$ is found as shown in Eq. (14) [6]:

$$\pi_{\tilde{\mathcal{F}}}(x) = \sqrt[3]{1 - \left(\alpha_{\tilde{\mathcal{F}}}^3(x) + \beta_{\tilde{\mathcal{F}}}^3(x)\right)} \tag{14}$$

2.1.6. Q-rung Orthopair Fuzzy Sets

q-ROFS is the generalization of the IFS, PFS, and FFS for q^{th} power of the MD and NMD. The comprehensiveness of inconsistency increases while q is getting bigger. A q-ROFS is defined as follows:

Definition 8: Let X be a given universe, q be a positive real number, $A^+(x) \in [0,1]$ be the degree of support for membership, and $A^-(x) \in [0,1]$ be the degree of support for non-membership. A q-ROFS $\tilde{A}$ is represented as $\tilde{A} = \{ x, A^+(x), A^-(x) \mid x \in X \}$ and satisfies Eq (15) [5].

$$0 \leq A^+(x)^q + A^-(x)^q \leq 1 \tag{15}$$

q-ROFS can be rewritten with the same terminology with IFSs as shown in Eq. (16):

$$\tilde{A} = \{ x, \mu(x), \vartheta(x) \mid x \in X \}, 0 \leq \mu(x)^q + \vartheta(x)^q \leq 1 \tag{16}$$

Accordingly, IDD is calculated as in Eq. (17) [5]:

$$\pi_{\tilde{A}}(x) = \sqrt[q]{1 - (\mu(x)^q + \vartheta(x)^q)} \tag{17}$$

2.1.7. Spherical Fuzzy Sets

PcFS does not allow modeling the uncertainties including inconsistent data. SFS is the generalized version of PcFS giving ability to model inconsistent data scenarios. The generalization is made with a similar logic with PFSs. A SFS is defined as below:

Definition 9: Let X be a given universe, $\mu_{\tilde{A}}(x) \in [0,1]$ be the MF, $\eta_{\tilde{A}}(x) \in [0,1]$ be the NeMF, $\vartheta_{\tilde{A}}(x) \in [0,1]$ be the NMD. A SFS $\tilde{A}$ is represented as $\tilde{A} = \{x, \mu_{\tilde{A}}(x), \vartheta_{\tilde{A}}(x), \eta_{\tilde{A}}(x) | x \in X \}$, and satisfies Eq. (18) [8]:

$$0 \leq \mu_{\tilde{A}}^2(x) + \vartheta_{\tilde{A}}^2(x) + \eta_{\tilde{A}}^2(x) \leq 1 \tag{18}$$

Accordingly, RD of an element $x \in X$ is yielded as shown in Eq. (19):

$$\rho_{\tilde{A}}(x) = \sqrt{1 - \left(\mu_{\tilde{A}}^2(x) + \vartheta_{\tilde{A}}^2(x) + \eta_{\tilde{A}}^2(x)\right)} \tag{19}$$

2.2. Conceptual Comparison of Fuzzy Set Extensions

The mentioned FST extensions in previous section are developed in line with the needs of Multi-Criteria Decision-Making (MCDM) problem. MCDM problems require single time modeling, and the process is finalized once a decision is made. If a new decision is needed and the environmental conditions are changed, the decision process should be rebuilt. However, some of the Decision Making (DM) problems and some other engineering problems are constructed for continuous systems. For example, Acceptance Sampling Plan (ASP) is a DM problem that assumes a continuous incoming item flow in decision process. Thence, the variability of the defectiveness of the incoming items should be considered by the decision process. The main purpose of this study is to assess the capabilities, advantages and disadvantages of the FST extensions that consider indeterminacy in a conceptual perspective for the modeling of continuous systems. This analysis can guide for the selection of the most appropriate FST extension in modeling of continuous systems.

Understanding the scenario has vital importance for successful modeling. FST extension must be decided after understanding the scenario and the causes of uncertainty well. The uncertainty of the considered scenario can be caused by the environment or the system itself. Hence, different FST extensions may be more suitable in different environments for the same problem. Essentially, understanding of the scenario is not sufficient for a high-quality modeling. FST extensions should also be well-understood. In this study, FST extensions have been analyzed based on the following criteria: (i) ease of calculation and implementation, (ii) scenario comprehensiveness, (iii) applicability in real cases and (iv) number of assumptions to obtain a useful guide for selection of the most appropriate FST extension in modeling of continuous systems. The rest of this section compares the FST extensions based on these criteria.

2.2.1. Ease of Calculation and Implementation

When an engineering technique is modified to handle the uncertainty, the complexity of the formulations increases. As the formulation becomes more complex, it requires more complex input data. The system to be modeled and the environment must give ability to collect suitable complex data to use the complex formulation efficiently. Since it may not be possible to collect complex data in some real cases, complex formulations may not be practicable in some scenarios. From this point of view, ordinary FS is the most advantageous alternative in terms of ease of implementation and calculation. On the other hand, using too simpler FST extension may cause reliability issues. For this reason, possibly complex but applicable FST extension should be selected. Even if the scenario seems suitable for modeling with a more complex FST extension, possible simplifications without loss of information should be made. By this way, the ease of calculation and implementation is provided without facing reliability issues. If the scenario allows conversion to ordinary FSs with ignorable loss of information, it is better to use ordinary FSs for gaining simplicity. Similarly, if the scenario allows conversion to IFS with neglectable loss of information, NS, SFS, PcFS, PFS, FFS and q-ROFS should be avoided. If indeterminacy and inconsistency is available together and both cannot be eliminated without loss of information, NS may be the best FST extension preference in terms of calculation simplicity. On the other hand, if linguistic approach is used, NS can harm the interpretability because of additional independent term representing indeterminacy. Because the logical meaning of independency of indeterminacy term can cause confusion for some cases. PFS, FFS and q-ROFS may be preferred if the independency of MD, NMD and IDD is not a desired case. Among these, the FST extension that is closer to ordinary FS should be selected to provide ease of calculation and implementation and reduce loss of

information. Because, when a looser inconsistency limit is decided, indeterminacy term will be calculated bigger, and the accuracy of the results will be reduced. Therefore, if the inconsistency limit is appropriate, the first choice should be PFS, then FFS and so on. If the scenario allows conversion to IFS with neglectable loss of information, it may be better to use IFS. It should be noted that one should be cautious while using PFS, FFS, SFS or q-ROFS for modeling of continuous systems without using a mechanism guaranteeing to collect data suitable with the inconsistency limitations. Otherwise, the system can produce values violating inconsistency limit and the model can have reliability issue.
If the scenario includes refusal case and it cannot be eliminated, the elimination of inconsistency should be evaluated for simplicity. If it is possible, PcFS becomes usable.

2.2.2. Scenario Comprehensiveness

Some of the FST extensions are the generalization of others. Generalization means covering them with some extra scenarios. For example, SFS is the most comprehensive FST extension. It may seem better to choose the most comprehensive FST extension in modeling but the complexity in calculation is the cost of this preference. If and only if the complexity is acceptable and this selection is value added for the further analyses, it will be better to select the comprehensive one. For example, NS is the generalizations of IFS. If the interested scenario includes inconsistent data case and the calculation complexity is acceptable, NS can be preferred. Otherwise, it would be better to use IFSs. Similarly, if the refusal case is a valid for the problem, PcFS can be preferred instead of IFSs.
With this point of view, NS is more advantageous than PFS, FFS, and q-ROFS. Modeling with PFS is possible if and only if the inconsistency level of data is always occurred under a limit. If the inconsistency violates Eq. (11) for some of the set elements, PFS cannot be used. As presented in previous section, FFS, and q-ROFS are FST extensions developed by a similar logic with PFS but with a greater inconsistency limit. Unfortunately, the risk of violating the validity condition (Eqs. (13) and (16)) is possible when a continuous system is modeled by using them. If they are not supported with a data collection mechanism limiting the inconsistency, the more reasonable approach is using NS. It should be noted that usage of NS may not be suitable if the independency of MD, NMD and IDD is not a desired circumstance or brings confusion and complexity.

2.2.3. Applicability in Real Cases

The applicability of an FST extension in real cases is related with the real-life availability of the scenario. If the main concern of the FST extension is not a common real issue, the applicability will be low. Each additional parameter brings complexity to the model, and the application may sometimes fail due to the complexity. If some parameters such as refusal are negligible, it would be better to simplify the scenario.
Usage of PFS, FFS, SFS, and q-ROFS in modeling of continuous systems is a bit problematic. Because, if there is no mechanism guaranteeing to collect data suitable with the inconsistency limitations, the collected may become incompatible with the model. In a such case, a transformation is needed, but loss of information is faced because of transformation operation. Another problem related to reliability is that the unsuitability of the scenario with the model may not be understood for a while during the application. If the system starts producing unsuitable data after a while, the obtained results may become garbage. Thus, it would be better to avoid using PFS, FFS, and q-ROFS while modeling continuous systems. Moreover, they do not offer more capabilities than NS and bring calculation complexity and risk of

violating the validity condition because of high inconsistency. If there is an ability to make system enhancement to avoid inconsistency, it should be the first thing to be done. After such an enhancement, IFS will be suitable for the scenario. Similar comparison can be made between SFS and PcFS.

2.2.4. Number of Generalizing Assumptions

Each FST extension is built on some assumptions. If an FST extension is preferred without understanding its assumptions, there is a risk of applying it to a wrong scenario and the reliability problem can be occurred for the obtained results. If an FST extension having fewer generalizing assumptions is preferred, the probability of facing with the reliability problem decreases. Generally, simpler FST extensions have more generalizing assumptions. For example, ordinary FS assumes that MD can be decided surely for all set elements. However, it may not be the case for the scenarios including human factor. Because of some factors such as hesitation of experts while assessing the uncertainty can cause lack of information about MD. IFS, NS, PFS, FFS and q-ROFS assume that the only cause of lack of information about MD is indeterminacy, but this is also a generalizing assumption. PcFS and SFS narrow the generalization of this assumption and propose the refusal concept as a new source of the lack of information about MD.

FST extensions have also assumptions about the inconsistency. Ordinary FS, IFS and PcFS have designed for the scenarios that do not produce inconsistent information. NS accepts inconsistent data and assumes that the root cause of the inconsistency is collecting data from multiple sources. For this reason, it considers MD, NMD and IDD as independent terms and allows unlimited inconsistency. However, the theory misses the logical paradoxes for the opposite asymptotic limits ($t = 1, i = 1, f = 1$) and ($t = 0, i = 0, f = 0$) [14]. PFS, FFS, q-ROFS and SFS assume that the nature of the inconsistency has a pattern with an exponential mathematical expression so it will always be occurred under a limit. In fact, it is hard to prove that the inconsistency of the system has a mathematical pattern in long run for the continuous systems.

3. Results and Discussion

Both ordinary FS and FST extensions have some advantages over the others. Ordinary FS has advantages in terms of ease of implementation and calculation. On the other hand, FST extensions are more powerful in terms of scenario comprehensiveness. The best preference is to select the FST extension having possibly minimum number of generalizing assumptions and maximum simplicity. The explanation given in the previous section shows that there is a trade-off between these two. Thus, deciding an optimal FST extension requires deep understanding of the theories and the considered scenario. Table 1 shows the summary assessment of the FST extensions based on some factors.

Table 1. Comparison of FST extensions based on pre-determined criteria

FST Extension	Applicability In Real Cases	Ease of Calculation	Number of Generalizing Assumptions	Scenario Comprehensiveness
FS	High	High	High	-
IFS	High	Medium	Medium	Indeterminacy
NS	Medium	Medium	Low	Indeterminacy + Inconsistency
PcFS	Medium	Low	Low	Indeterminacy + Refusal
SFS	Low	Very Low	High	Indeterminacy + Refusal + Limited Inconsistency
PFS	Low	Low	High	Indeterminacy + Limited Inconsistency
FFS	Low	Low	High	Indeterminacy + Limited Inconsistency
q-ROFS	Low	Low	High	Indeterminacy + Limited Inconsistency

There are some limitations about FST extensions. IFS theory mainly attends to MD and NMD. Indeterminacy arises from the lack of information about MD and NMD. However, lack of information about MD and NMD may be caused by some other factors from indeterminacy in some scenarios. For example, some experts can refuse to make an assessment. Modeling with IFS can bring reliability problem for such scenarios. Disregarding the refusal case is an important limitation of IFSs. PcFS may be preferable alternative for such scenarios. The meaning of the word "refusal" is rejecting to make an assessment. Cuong [7] gives voting example for explaining the meaning of the term by dividing the voters into four groups: voting for a party, voting blank, voting against a party, refusing to vote. Representing the fourth group in some studies can be meaningful and PcFS gives useful results. However, it should not be ignored that even for the same voting example, the same data for another study may mean missing information depending on the research question.

NS theory looks like a good option to model the scenarios including both indeterminacy and inconsistency. Unlike PFS theory, it does not put a limit for inconsistency, but some discussions are available on the independency of truthiness, indeterminacy, and falsity terms. NS theory is seemed mathematically allows this independency, but paradoxes occur for the limit values of the terms: $t = 1, i = 1, f = 1$ and $t = 0, i = 0, f = 0$ [14]. If the data for the modeled problem is generally emerged near the limits, one should be cautious about the obtained results.

Since PFS, FFS, and q-ROFS are theoretical extensions of IFS, there are some discussions in the literature about the applicability of them in real case applications. Sevastjanov et al. [14] ask these questions for PFS: "what $\mu_{\tilde{A}}^2$ means in a natural language?" and "for which superiority was $\mu_{\tilde{A}}^2$ chosen over other powers such as $\mu_{\tilde{A}}^3$ and $\mu_{\tilde{A}}^4$?". In addition, how to ensure that Eq. (11),(13),(16) are satisfied in all cases in real life applications is also an issue to be considered. Another issue about PFS, FFS, and q-ROFS is that the indeterminacy is produced synthetically depending on the gap between 1 and the sum of the q^{th} (2 for PFS, 3 for FFS) power of the terms. Which means that the greatness of IDD is directly dependent on initial model configuration. For example, assume that the sum of the 2^{nd} power of MD and NMD exceed 1 but 3^{rd} power of MD and NMD does not exceed 1. The one who models this problem can think that using FFS is the best choice. However, another people can decide to model the problem by using q-ROFS and can use a non-integer value such as 2.75 that does not violate the main condition of q-ROFS presented in Eq. (15). Similarly, If FFS is preferred for a problem instead of PFS, the greatness of the IDD dramatically increases just because of this modeling decision. Here is the question to answer: "Does the model design really affect the hesitancy of the experts?". This issue is what we named as "synthetically production of indeterminacy". This can be concluded that the indeterminacy is subjective and unreliable in PFS, FFS, and q-ROFS. Even though the greatness of IDD may not cause a huge loss of information for MCDM problems and the ranking of alternatives can be done with an ignorable error risk, it may cause reliability issue for the fuzzy models of non-MDCM problems requiring sensitivity calculation. If the problem formulation uses IDD directly in calculations and the greatness of IDD highly affects the obtained results, the obtained results will not be reliable. Acceptance Sampling Plan (ASP) is a good example for this type of problems. If the inconsistency is inevitable case and the "independency of indeterminacy term" is not a desired circumstance, it can be considered to use an advanced data collection procedure such as proposed in [17] that scales the indeterminacy in a flexible way suitable with the main condition of PFS given in Eq. (11). Similar critics can be done for SFS by considering the greatness of RD by considering Eq. (19).

Table 2 shows the obtained IDD values of IFS, PFS, q-ROFS, and NS for given 9 evaluations. The first 6 evaluations are consisting of MD and NMD while the remaining 3 of them consist of MD, NMD, and IDD. The evaluations are ranked by using the Score and Accuracy functions suggested by [18], [4], [6], [5], [19]. Results show that greatness of IDD causes little loss of information between PFS and FFS while ranking fuzzy evaluations. Amount of loss of information increases for q-ROFS while q is getting bigger. There is a difference between the results of IFS and NS too. Table 3 includes 9 evaluations that are consist of MD, NMD, and IDD and the obtained ranking results for NS, PcFS, and SFS. Results of FST extensions are different from each other in Table 3 too. In can be concluded that event for MCDM problems, the FST extension decision and the initial modeling configuration affect the obtained results.

Table 2. Comparison of produced IDD values and assessment rankings of IFS, PFS, FFS, q-ROFS, and NS for given input values

	Input			Calculations															
				FS		IFS		PFS		FFS		q-ROFS (q=1.38)		q-ROFS (q=10)		NS (Normalized)			
#	MD	NMD	IDD	IDD	Rank	IDD	Rank	IDD	Rank	IDD	Rank	IDD	Rank	IDD	Rank	MD	NMD	IDD	Rank
1	0.6	0.4	-	0.00	2	0.00	5	0.69	6	0.90	6	0.34	6	1.00	4	0.60	0.40	0.00	5
2	0.7	0.3	-	0.00	1	0.00	2	0.65	1	0.86	1	0.31	1	1.00	1	0.70	0.30	0.00	2
3	0.6	0.3	-	N/A*	N/A	0.10	4	0.74	4	0.91	5	0.43	4	1.00	4	0.60	0.30	0.10	7
4	0.6	0.2	-	N/A	N/A	0.20	3	0.77	3	0.92	4	0.51	2	1.00	4	0.60	0.20	0.20	9
5	0.7	0.5	-	N/A	N/A	N/A	N/A	0.51	5	0.81	3	0.02	5	1.00	1	0.58	0.42	0.00	6
6	0.7	0.4	-	N/A	N/A	N/A	N/A	0.59	2	0.84	2	0.20	3	1.00	1	0.64	0.36	0.00	4
7	0.7	0.2	0.1	0.7	0.2	0.10	1	N/A	N/A	N/A	N/A	N/A	N/A	N/A	N/A	0.70	0.20	0.10	3
8	0.7	0.2	0.0	N/A	N/A	N/A	N/A	N/A	N/A	N/A	N/A	N/A	N/A	N/A	N/A	0.78	0.22	0.00	1
9	0.7	0.4	0.1	N/A	N/A	N/A	N/A	N/A	N/A	N/A	N/A	N/A	N/A	N/A	N/A	0.58	0.33	0.08	8

*N/A: Not applicable

Table 3. Comparison of produced IDD values and assessment rankings of NS, PcFS, and SFS for given input values

	Input			Calculations									
				NS				PcFS			SFS		
#	MD	NMD	IDD	MD	NMD	IDD	Rank	IDD	RD	Rank	IDD	RD	Rank
1	0.6	0.4	0	0.60	0.40	0.00	4	0.00	0.00	6	0.00	0.69	6
2	0.7	0.3	0	0.70	0.30	0.00	2	0.00	0.00	3	0.00	0.65	2
3	0.6	0.3	0.1	0.60	0.30	0.10	6	0.10	0.00	5	0.10	0.73	6
4	0.6	0.2	0.2	0.60	0.20	0.20	7	0.20	0.00	4	0.20	0.75	8
5	0.7	0.5	0.2	0.70	0.50	0.20	8	N/A	N/A	N/A	0.20	0.47	7
6	0.7	0.4	0.3	0.70	0.40	0.30	9	N/A	N/A	N/A	0.30	0.51	9
7	0.7	0.2	0.1	0.70	0.20	0.10	3	0.10	0.00	1	0.10	0.68	3
8	0.7	0.2	0.0	0.70	0.20	0.00	1	0.00	0.10	2	0.00	0.69	1
9	0.7	0.4	0.1	0.70	0.40	0.10	5	N/A	N/A	N/A	0.10	0.58	4

*N/A: Not applicable

Another important point in Table 2 is the greatness of produced IDD values for PFS, FFS, and q-ROFS (Similar issue is available in Table 3 for RD values of SFS.). For example, the produced IDD value of the 4th assessment for PFS is 0.77 which is bigger than MD. For the same assessment, IDD is calculated as 0.2 (which is just one third of MD) for IFS. Similar issue is available for FFS and q-ROFS too. IDD values are getting bigger while q is increasing. In order to measure the size of the reliability issue for a non-MCDM problem that needs sensitive calculation, Acceptance Sampling Plan (ASP) formulation suggested by Işık & Kaya [20] was used and the results shown in Table 4 were obtained. As shown in Table 4, relative greatness of IDD directly affects the results of ASP problem. Acceptance probability (P_a) is found as 0 for PFS, FFS, and q-ROFS while it is found as 56% for IFS. The main cause of this difference is the theoretical background of PFS, FFS, and q-ROFS theories. Since they are developed in line with the needs of MCDM problem, they focus on ranking the alternatives. As seen in Table 2 and 3, loss of information is not so big for MCDM so the

reliability issue of the results is less for MCDM problems. On the other hand, the results of these FST extensions are highly unreliable for ASP problem. The reliability issue increases while the inconsistency level of the assessments is getting smaller and the inconsistency limit of FST Extension is getting bigger.

Table 4. Acceptance sampling plan results for IFS, PFS, FFS, q-ROFS, and NS for given plan parameters

Plan Parameters					
Population Size	Sample Size	Allowed Defective Item Count	Allowed Indeterminate Item Count	MD	NMD
500	50	15	10	0.6	0.2
Results					
FST Extension	Acceptance Probability	Rejection Probability	Average Outgoing Quality	Average Total Inspection	
IFS	0.559	0.031	0.112	248.652	
PFS	0.000	0.000	0.000	499.991	
FFS	0.000	0.000	0.000	499.999	
q-ROFS (q = 1.38)	0.003	0.002	0.001	498.484	
q-ROFS (q = 10)	0.000	0.000	0.000	500.000	
NS (Normalized)	0.559	0.031	0.112	248.652	

In the literature, there is no formulation for the fuzzy ASPs considering refusal case. The ASP formulation proposed by Işık & Kaya [12] was adapted for the case of refusal. Using the acceptance probability characteristic of this adapted formulation, PcFS and SFS was numerically compared as seen in Table 5. Findings similar to those between IFS and PFS are also observed between PcFS and SFS. For the same MD, NMD, and NeMD values, the acceptance probability is found as %0.57 by modelling with SFS while it is found as %57.81 by modeling with PcFS. The table shows that the results are directly dependent on the initial modeling configurations. For ASP, the reliability issue for SFS models is caused by producing a large theoretical RD value. As shown in Table 3, a similar reliability problem does not occur for MCDM problems. Therefore, caution should be exercised when using SFS for non-MDCM problems that require precise fuzzy modeling.

Table 5. Acceptance sampling plan results PcFS and SFS for given plan parameters

Plan Parameters						
Population Size	Sample Size	Allowed Defective Item Count	Allowed Indeterminate Item Count	MD	NMD	NeMD
500	50	20	5	0.6	0.2	0.1
Results						
FST Extension	Produced RD	Acceptance Probability				
PcFS	0.10	%57.81				
SFS	0.77	%0.57				

In most of the studies in the literature, these FST extensions are used with linguistic fuzzy modeling (LFM) approach. LFM is good at interpretability, but it has weaknesses about accuracy of the results. For this reason, using LFM for the modeling of the problems requiring sensitive calculations is a challenging issue. The LFM approach should be integrated with some sophisticated mechanisms to be able to obtain accurate results and gain a capability of making an efficient sensitivity analysis. For example, ASP needs precise fuzzy modeling in decision phase, and Işık & Kaya [17] integrates the LFM with some novel mechanisms to provide sensitive and accurate results. As another example problem type, investment analysis problems in engineering economy also requires sensitive calculations in decision process.

4. Conclusion

Most of the modern engineering techniques are designed for certain events. However, the real-life problems are generally including uncertainty. FST is one the most popular approaches used to reflect the uncertainties of real-life to engineering models. The uncertainty can be caused by various factors in real world applications. The nature of the uncertainty

changes depending on these factors. Several FST extensions have been offered for better modeling of uncertainties having different natures. Lack of expertness about the modeled scenario, human hesitancy while making assessment are some example factors affecting the nature of uncertainty. These types of factors can cause indeterminacy about the uncertainty level of the events. There are various FST extensions that consider indeterminacy in modeling. In fuzzy modeling, selection of the most suitable FST extension has key importance on the reliability of the obtained results. Since these FST extensions consider similar scenarios and some parts of the theories overlap with some other extensions, understandings the theories and the nature of scenarios is crucial to obtain reliable results.

The FST extensions considering indeterminacy are developed in line with the requirements of MCDM problem. For this reason, some of their assumptions are made by considering MCDM problems. The assumptions and the limitations of theories may cause reliability issues about the result of the fuzzy models of non-MCDM problems and continuous systems. In this study, capabilities, advantages, and disadvantages of the FST extensions that consider indeterminacy have been assessed and compared in a conceptual perspective in line with the needs of modeling of non-MCDM problems and continuous systems. The analysis showed that some extensions have clear advantages over others in terms of applicability, ease of calculation and scenario comprehensiveness. The analysis has been illustrated on numerical examples to make the findings clear. The analysis builds a preliminary step for a guiding approach for the selection of the most reliable FST extension in modeling.

As a future research direction, this study can be extended by analyzing some other FST extensions. Depending on this analysis, a guiding procedure can be proposed for choosing the most appropriate FST extension in fuzzy modeling.

References

[1] Zadeh, L. A. (1965). Fuzzy sets. Information and Control, 3(8): 338-353.

[2] Atanassov, K. T. (1983). Intuitionistic Fuzzy Sets. VII ITKR Session, Sofia.

[3] Smarandache, F. (2005). Neutrosophic set-a generalization of the intuitionistic fuzzy set. International Journal of Pure and Applied Mathematics, 3(24): 287.

[4] Yager, R. R. (2013). Pythagorean fuzzy subsets. 2013 Joint IFSA World Congress and NAFIPS Annual Meeting (IFSA/NAFIPS).

[5] Yager, R. R. (2016). Generalized orthopair fuzzy sets. IEEE Transactions on Fuzzy Systems, 25(5): 1222-1230.

[6] Senapati, T. and Yager, R. R. (2020). Fermatean fuzzy sets. Journal of Ambient Intelligence and Humanized Computing, 11: 663-674.

[7] Cuong, B. C. and Kreinovich, V. (2014). Picture fuzzy sets. Journal of Computer Science and Cybernetics, 30(4): 409-420.

[8] Kahraman, C., and Kutlu Gündoğdu, F. (2018). From 1D to 3D membership: spherical fuzzy sets. In BOS/SOR2018 Conference. Warsaw, Poland.

[9] Kaya, İ., Çolak, M. and Terzi, F. (2019). A comprehensive review of fuzzy multi criteria decision making methodologies for energy policy making. Energy Strategy Reviews, 24: 207-228.

[10] Mardani, A., Nilashi, M., Zavadskas, E. K., Awang, S. R., Zare, H. and Jamal, N. M. (2018). Decision making methods based on fuzzy aggregation operators: Three decades review from 1986 to 2017. International Journal of Information Technology & Decision Making, 17(2): 391-466.

[11] Salih, M. M., Zaidan, B. B., Zaidan, A. A. and Ahmed, M. A. (2019). Survey on fuzzy TOPSIS state-of-the-art between 2007 and 2017. Computers and Operations Research, 104: 207-227.

[12] Alkan, N. and Kahraman, C. (2021). Evaluation of government strategies against COVID-19 pandemic using q-rung orthopair fuzzy TOPSIS method. Applied Soft Computing, 110: 107653.

[13] Kahraman, C., Oztaysi, B., Otay, I. and Onar, S. C. (2020). Extensions of ordinary fuzzy sets: a comparative literature review. International Conference on Intelligent and Fuzzy Systems.

[14] Sevastjanov, P. and Dymova, L. (2021). On the neutrosophic, pythagorean and some other novel fuzzy sets theories used in decision making: invitation to discuss. Entropy, 23: 1485.

[15] Akram, M. and Dudek, W. A. (2011). Interval-valued fuzzy graphs. Computers and Mathematics with Applications, 61: 289-299.

[16] Smarandache, F. (2014). Introduction to neutrosophic statistics, Infinite Study.

[17] Işık, G. and Kaya, İ. (2022). A new integrated methodology for constructing linguistic pythagorean fuzzy statements for decision making problems. Journal of Intelligent & Fuzzy Systems, 43(4): 4883-4894.

[18] Xu, Z. (2007). Intuitionistic fuzzy aggregation operators. IEEE Transactions on fuzzy systems, 15(6): 1179-1187.

[19] Şahin, R. and Küçük, A. (2014). Generalised neutrosophic soft set and its integration to decision making problem. Applied Mathematics & Information, 8(6): 2751-2759.

[20] Işık, G. and Kaya, İ. (2021). Design and analysis of acceptance sampling plans based on intuitionistic fuzzy linguistic terms. Iranian Journal of Fuzzy Systems, 18(6): 101-118.

Appendix – List of Abbreviations

Abbreviation	*Statement*
ASP	Acceptance Sampling Plan
DM	Decision Making
FFS	Fermatean Fuzzy Set
FS	Fuzzy Set
FST	Fuzzy Set Theory
IDD	Indeterminacy Degree
IFS	Intuitionistic Fuzzy Set
IVFS	Interval Valued Fuzzy Set
LFM	Linguistic Fuzzy Modeling
MCDM	Multi-Criteria Decision-Making
MD	Membership Degree
MF	Membership Function
NeMD	Neutral Membership Degree
NMD	Non-Membership Degree
NMF	Non-Membership-Function

NS	Neutrosophic Set
P_a	Acceptance Probability
PcFS	Picture Fuzzy Set
PFS	Pythagorean Fuzzy Set
q-ROFS	q-Rung Orthopair Fuzzy Set
RD	Refusal Degree
SFS	Spherical Fuzzy Set